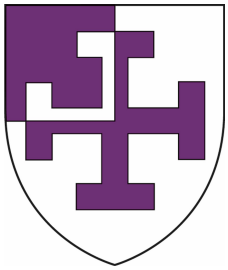


An exploration of vacuum evaporable non-fullerene acceptors for use in organic solar cells and molecular orientation in evaporated thin films

Irfan Habib

St Cross College



University of Oxford

A thesis presented for the degree of

Doctor of Philosophy

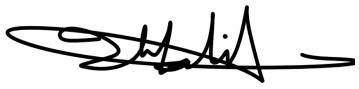
Michaelmas 2023/24

Declaration

I, Irfan Habib, declare that all the work in this thesis is original unless stated otherwise and has not been submitted in support of an application for another degree or qualification, at either this university or any other institute of learning.

Word Count: $29533/40000$

Data from this thesis was used in the following publication:
I. Habib et al. "Vacuum deposited organic solar cells with BTIC-H as A-D-A non-fullerene acceptor", *APL Materials* 11.6 (2023), DOI: 10.1063/5.0148208



01/06/2024

Signature *Date*

This thesis is dedicated to

my loving parents, my awesome brother, and of course my brilliant wife,

this is for you.

Acknowledgements

My PhD journey began at the start of 2019 and is now finally coming to a close at the beginning of 2024. The past 5 years have both been wonderful and incredibly demanding. While I am so delighted to be done, I am also sad to say goodbye to many of the amazing people I've met along the way, without many of who I would not have been able to finish my PhD.

I would like to thank the Oppenheimer Memorial Trust and the Firstrand Foundation in providing me with the necessary financial support in getting my PhD going. Without your assistance I would not have been able to embark on this amazing journey. I would also like to acknowledge the XMaS at the European Synchrotron Radiation Facility and B07 at Diamond Light Source for giving me access to the tools at the beamlines to conduct my research with. Big shout out to the staff at these beamlines, especially Dr Oier Bikondoa, Dr Dave Grinter, and Dr Pilar Ferrer for their amazing support.

I would like to thank my supervisor Prof Moritz Riede for starting me on this journey way back in 2018. He gave me the ultimate freedom to pursue whatever topics interested me, while providing a light steering touch which I greatly appreciated. Thanks for being great, and I hope our work intersects again in the future. A huge thanks to all the lovely people in the AFMD group, including all the past members who have since moved on. The vibe was always awesome, friendly, and extremely supportive. From the moment I joined I was greeted with the most jovial banter between the then 'Senior Post Docs' Dr Sameer Kesaava and Dr Alberto Privitera that made me feel right at home. Others in the office would undoubtedly categorise this banter as 'noise', but I loved it. And of course to Dr Pascal Kaienburg who was there from the very beginning and is still there as

I'm leaving (although now with a fancy fellowship!). He was a fantastic mentor, and an even better friend. I will definitely miss the lunch/coffee breaks, but I will definitely not miss all the ECHO maintenance! Thanks to Dr Jin Yao at the National Thin Film Cluster for his wealth of expertise regarding vacuum deposition systems and for always being available to help out. To the PhDs who've graduated since I joined: Hanyang, Giulio, Anna, Bernd, and of course Andreas. They truly paved the way for me. Thanks for the commiseration, the advice, and of course the coffee. To my fellow PhDs: Ming, Nicky, Zhenlong, Olivia, Kate, I wish you all the very best in completing your own monumental journeys. Thanks for the vibes, I will miss working with you all!

Dean Delongchamp (NIST), Subhrangsu Mukherjee (NCSU), Elliot Gann (NSLS-II), and James Hilfiker (J.A. Woollam) were fonts of wisdom with regards to all things related to molecular orientation! I frequently took advantage of this during the last year or so of my PhD. They were always happy to chat and were very kind. I am incredibly appreciative of their support.

Now for my friends outside of the office. Firstly, to all the Bungie Jumpers, I did it despite your terrible influence! Jokes aside, the many long hours gaming on Discord is what kept me sane during this journey. Good news! We will now finally be able to resume our Dungeons and Dragons campaign. To my friends in Oxford, I hope I will be seeing more of you now that I'm no longer a thesis-writing recluse. To my friends back home, and to those scattered throughout the world, thanks for your friendship. It helped more than you can imagine.

To my new colleagues and friends at Oxford Ionics, thanks for being so supportive during the final months of thesis edits. The flexibility you guys afforded was absolutely invaluable, and the kind words and advice were very appreciated.

And of course thanks to my family. To the Habibs, the Gogas, and the Badats,

and of course to my aunty Rasheeda who is always ready to answer any and every question Sabica and I have about adulting, thanks for all the love, prayers, and support. Special thanks to my Nani who I know has been praying night and day for me to finish this PhD. I've been blessed with amazing in-laws, especially Aunty Maryam, Sumbul, and her adorable little munchkin Enaya who joined us halfway through my PhD, you guys are the best, thank you for all the support.

Mom, Dad, Zidaan, I did it! Finally. We can finally do away with the "How's your thesis coming along" or the "When are you submitting again?" questions that gave us all so much trauma. Jokes aside, I am truly blessed to have such amazing family. The support you provided, the advice you gave, the love you showed, all of it was so so instrumental in getting me to this completion. Thank you from the bottom of my heart.

And finally to my loving wife Sabica, this truly would not have been possible without you. You put up with so much nonsense from my end in the months leading up to this, and you never complained once. Okay maybe once or twice. I'm just joking! In many ways this PhD was the beginning of our married life together, and the end of it marks the beginning of a new chapter in our lives. I am so excited to explore it with you.

Abstract

Organic solar cells (OSCs) offer an attractive pathway for next-generation photovoltaic technologies. Recent advances in molecular design have advanced the technology with the advent of non-fullerene acceptors (NFAs). NFAs have enabled rapid efficiency gains in OSCs, with state-of-the-art OSCs showcasing efficiencies of close to 20%. These advances are constrained to the solution processing field and are not compatible with vacuum deposition, a more industrially mature and commercially relevant manufacturing method which also eliminates the need for solvent use and related components in the fabrication process.

In the first part of this thesis various NFA molecules, specifically oligothiophenes and a perylene diimide, are investigated for use as a vacuum evaporable NFA. the investigation focused on studying the optical and energetic behaviour, primarily using spectroscopic ellipsometry (SE) and ambient photoelectron spectroscopy, of these materials. Based on the results, the oligiothiophene BTIC-H was identified as a strong candidate for use in vacuum evaporated NFA OSCs with a good extinction coefficient $k = 0.6$, and a HOMO and LUMO of -5.9 and -3.6 eV, respectively. Planar and bulk heterojunction devices using BTIC-H were explored. PHJ devices showcased promising performance (good $V_{OC} \approx$ 1V with low voltage losses ≈ 0.8 V), however, photocurrents in BHJ devices were poor (≈ 0.5 mA/cm^2). These results showed that there is very real promise for vacuum evaporable NFAs, however, significant optimisation of devices as well as molecular design are needed.

The second part of this thesis explored a comprehensive analysis of molecular orientation in vacuum evaporated organic thin films, a concept which is often poorly understood but plays a critical role in the photophysics of organic elec-

tronics. This was done using SE and near edge X-ray absorption fine structure (NEXAFS) spectroscopy. Three different molecules were investigated, namely alpha-sexithiophene, the merocyanine dye HB194, and the donor-acceptor (DA) type donor DTDCPB. NEXAFS was used to calculate the mean facial orientation of the molecules while SE was used to calculate the backbone orientation, with the results supplemented by grazing incidence wide-angle X-ray scattering (GIWAXS). Results were compared to literature, showing strong agreement in the case of alpha-sexithiophene and revealing significant changes in orientation upon substrate heating, which were broken down into their respective facial and backbone orientation changes. These results showed that understanding both the facial and backbone changes reveal rich information about the microstructure of organic thin films and provide a foundation for more comprehensive analysis of blended films which may reveal device relevant insights.

Contents

List of Figures xii

List of Tables xviii

List of Acronyms xix

1 Introduction 1

1.1 Motivation . . . 1
1.2 What are Organic Photovoltaics? . . . 2
1.3 Emergence of Non-Fullerene Acceptors . . . 4
1.4 Current Challenges in Organic Photovoltaics . . . 5
1.5 Problem Statement . . . 7
1.6 Research Scope . . . 9
1.7 Thesis Outline . . . 10

2 Physics of Organic Solar Cells 11

2.1 Organic Semiconductor Molecules . . . 11
2.1.1 Energy Levels . . . 11
2.1.2 Absorption and Excitation . . . 13
2.2 Organic Thin Films . . . 16
2.2.1 Energy Level Shifts in Thin Films . . . 16
2.2.2 Exciton Diffusion . . . 21
2.3 Organic Solar Cells . . . 22
2.3.1 Charge Transfer at the Donor Acceptor Interface . . . 22
2.3.2 Charge Generation and Recombination . . . 27
2.3.3 Current Density-Voltage Characteristics . . . 30

2.4 Development of NFAs in OPV 32
2.4.1 1986-2012 33
2.4.2 2013-2016 34
2.4.3 2017-2023 35
2.4.4 Towards Vacuum Evaporable NFA structures 36

3 Methods and Materials 38
3.1 Methods 38
3.1.1 Sample Fabrication 38
3.1.2 Thin Film Characterisation 41
3.1.3 Device Measurements 57
3.2 Materials 62
3.2.1 Overview of Materials 62
3.2.2 BTIC-H 62
3.2.3 TTR and TTIC4F 65
3.2.4 Perylene Diimides 65
3.2.5 α-sexithiophene 66
3.2.6 HB194 67
3.2.7 DTDCPB 68
3.2.8 SubNc 68
3.2.9 DCV5T-Me 69

4 Identifying Evaporable Small Molecule Non-Fullerene Acceptors 70
4.1 Introduction 70
4.2 Evaporability of Candidate NFAs 72
4.2.1 BTIC-H 72
4.2.2 PDIFCN2 75
4.2.3 TTR 76

4.2.4 TTIC4F 77
4.3 Optical Characterisation 78
4.3.1 BTIC-H 78
4.3.2 PDIFCN2 80
4.3.3 TTR 84
4.4 Energy Level Characterisation 85
4.4.1 BTIC-H 85
4.4.2 PDIFCN2 87
4.4.3 TTR 87
4.5 Microstructure Characterisation of BTIC-H 88
4.6 Summary and Conclusions 93

5 Using BTIC-H as an NFA in evaporated organic solar cells 95
5.1 Introduction 95
5.2 PHJ Devices 95
5.3 BHJ Devices 104
5.4 Microstructure of DCV5T:BTIC-H blend 109
5.5 Summary and Conclusions 114

6 Using NEXAFS and SE to characterise orientation in evaporated small molecule thin films 118
6.1 Introduction 118
6.2 NEXAFS Results 122
6.2.1 a6T 122
6.2.2 DTDCPB 128
6.2.3 HB194 132
6.3 Spectroscopic Ellipsometry Results 137
6.3.1 a6T 138

6.3.2 DTDCPB . . . 139
6.3.3 HB194 . . . 140
6.4 GIWAXS results . . . 142
6.5 Discussion . . . 144
6.6 Conclusion . . . 148

7 Summary, Evaluation and Recommendations 151
7.1 Concluding Remarks . . . 151
7.1.1 Identification of candidate NFA for evaporable OSCs . . . 151
7.1.2 Developing a more comprehensive view of the molecular orientation in evaporated organic thin films . . . 153
7.1.3 Final Remarks . . . 156

Appendix A Appendix 179
A.1 BTIC-H NMR . . . 179
A.2 Spectroscopic ellipsometry fitting . . . 180
A.2.1 BTIC-H . . . 180
A.2.2 PDIFCN2 . . . 180
A.2.3 TTR . . . 180
A.2.4 a6T . . . 180
A.2.5 DTDCPB . . . 180
A.2.6 HB194 . . . 181
A.3 TTR preliminary devices . . . 182
A.4 PDIFCN2 preliminary devices . . . 183
A.5 APS of PHJ donors . . . 184
A.6 EA estimation values . . . 185
A.7 Voltage Loss Fits for BTIC-H PHJ Devices . . . 186
A.8 NEXAFS Data . . . 187

List of Figures

1.1 Simplified illustration of the donor acceptor concept 4
1.2 Molecular structures of ITIC and $PC_{71}BM$ 5
1.3 NREL chart showing record PCEs of solar PV 6

2.1 Energy level diagram showing the formation of molecular orbitals 11
2.2 Schematic of energy level shifts from molecules to thin films . . . 16
2.3 In-plane and out-of-plane optical constants of DIP 18
2.4 Schematic of H-type and J-type aggregation 19
2.5 An illustration of a device stack 22
2.6 An illustration of CT state formation at a DA interface 24
2.7 Illustration of the impact of χ blend morphology 25
2.8 Summary of key processes in OSCs 29
2.9 Timeline of NFA development 32
2.10 Simple NFA structures 36

3.1 Illustration of the deposition process 38
3.2 Schematic of a spectroscopic ellipsometry measurement 41
3.3 Snapshot of the SE fitting process: Cauchy model 44
3.4 Snapshot of the SE fitting process: b-spline model 45
3.5 Snapshot of the SE fitting process: anisotropic b-spline model . . 46
3.6 Orientation of the TDM calculated from SE 48
3.7 Typical example of optical constants modelled via SE. 49
3.8 Schematic of a NEXAFS measurement 50
3.9 Example of a NEXAFS measurement 51
3.10 Illustration of orbital orientation vector tracking the molecular face-on orientation. 53

3.11 Molecular structures of studied NFAs 63
3.12 Molecular structures of donor molecules 64

4.1 Molecular structures of studied NFAs 72
4.2 Images of BTIC-H before and after evaporation. 73
4.3 TGA and DSC scans of BTIC-H and DCV5T 75
4.4 Images of PDIFCN2 before and after evaporation. 76
4.5 Images of TTR powder in a crucible before and after an evaporation. Before evaporation TTR appears to be a red powder with distinct agglomeration present. After evaporation the material appears more green. 77
4.6 Images of TTIC4F powder in a crucible before and after an evaporation. Before evaporation TTIC4F appears to be a red powder with distinct agglomeration present. After evaporation the material appears burnt and is likely degraded. 78
4.7 Optical constants of BTIC-H thin film. 81
4.8 UV-Vis data of BTIC-H in solution. 82
4.9 Steady state photoluminesence data of BTIC-h thin film. 83
4.10 Optical constants of a PDIFCN2 thin film. 83
4.11 Optical constants of TTR 85
4.12 APS and CV data of BTIC-H thin film and in solution, respectively. 86
4.13 APS data of TTR thin film 88
4.14 AFM data of BTIC-H thin film. 89
4.15 XRR data of BTIC-H thin film 90
4.16 GIWAXS data of BTIC-H thin film. 91
4.17 NEAXFS data and fitting results of BTIC-H thin film. 93

5.1 a) Chemical structures and energy levels of the molecules used in this chapter. IP levels were measured via Ambient Photoelectron Spectroscopy. EA levels were estimated using Equation 3.6 [84] that relates EA levels probed via IPES to the sum of the HOMO level and energy of absorption onset, which is defined in Chapter 3. The latter is determined from the absorption onset in the extinction coefficients in b). Extinction coefficients were calculated from data obtained via spectroscopic ellipsometry using anisotropic models where relevant, with only the device relevant in-plane data shown, and with C60 data included as a reference. Reproduced from [14] with permission. 96

5.2 a) Device stack for PHJ devices. BPhen was used as ETL (electron transport layer), and MoO3 was used as the HTL (hole transport layer), nominal thicknesses were ITO (110 nm)/MoO3 (3 nm)/ Donor (20 nm/ BTIC-H (20 nm)/ BPhen (8 nm)/ Al (100 nm). JV measurements under approximately 1 sun illumination (solid lines) and in the dark (dashed lines) of individual PHJs using donors DCV5T, SubNc, DTDCPB, and HB194. c) Log plot of dark JV measurements of the same devices as b). d) Extended JV scans of the samples in b) showing behaviour at reverse bias. . 99

5.3 a) Plot showing the simulated contributions to the maximum J_{SC} assuming 100% internal quantum efficiency and exciton diffusion length of 20 nm (SubNC) and 10 nm (DCV5T, HB194, DTDCPB), bottom bars indicate donor contributions and top bars indicate BTIC-H contributions, simulated with a transfer matrix method model adapted from [121]. b) Plot showing the effect of HOMO energy offset between donors and BTIC-H on the ratio between the J_{SC} to the simulated J_{SC} assuming 100% IQE, and the V_{OC} . Purple crosses indicate the $J_{SC\ meas}$ / $J_{SC\ max}$ ratio, diamonds indicate the V_{OC} . The donor molecules the offsets refer to are listed on the image. 102

5.4 a) External Quantum Efficiency (EQE) measurements of PHJ devices shown in Figure 5.2, plotted on a linear scale. b) Same EQE as in a), plotted on a logarithmic scale. No shoulders are discernible in the EQE, except for the HB194 PHJ at ≈ 1.7 eV. . . . 103

5.5 Voltage loss breakdown showing the $\Delta V_{J_{SC}}$,ΔV_{rad}, and ΔV_{nonrad} contributions a) split alongside each other and b) stacked below the photovoltaic gap. Individual contributions can be found in Table 5.2. Fitting details can be found in the Appendix A.7. 104

5.6 a) Device stack for BHJ devices. BPhen was used as hole blocking layer, and MoO_3 was used as the hole transport layer, nominal thicknesses were ITO (110 nm)/MoO_3 (3 nm)/ DCV5T:BTIC-H (1:1 vol, 40 nm)/ BPhen (8 nm)/ Al (100 nm).b) JV results under illumination of DCV5T/BTIC-H PHJ and DCV5T:BTIC-H BHJ devices and their C60 counterparts. 105

5.7 a) EQE results of the same devices shown in Figure 5.6, b) EQE of the same devices, plotted on a logarithmic scale. 106

5.8 OTRACE measurement of the 60nm DCV5T:BTIC-H BHJ. (a) extracted mobilities at two different ramp rates and for several delay times. Results are in good agreement and yield a low mobility of 1.3×10^{-6} cm^2/Vs. (b) Transient current traces for different delay times and a ramp rate of 200V/ms. The black lines smooth the raw data and red dots indicate the automatically extracted maxima used to calculate the mobility. For long delay times the height of the current peak decreases and a maximum cannot be determined. Measurements were taken and processed by Pascal Kaienburg from the University of Oxford. 107

5.9 Voltage loss breakdown according to detailed balance principle showing $\Delta V_{J_{SC}}$, ΔV_{rad}, and ΔV_{nonrad} contributions, shown a) split up alongside each other and b) stacked with the photovoltaic band gap for ease of reference. 109

5.10 GIWAXS and AFM images of BTIC-H and DCV5T (neat and blend) films deposited at RT 110

5.11 GIWAXS and AFM images of BTIC-H and DCV5T (neat and blend) films deposited at 80°C 113

5.12 JV measurements of BTIC-H:DCV5T BHJs deposited at 80°C . . 114

5.13 NFA Screening Flowchart 117

6.1 Geometry of different orientation angles of an elongated molecule. 121

6.2 NEXAFS results of a6T deposited at room temperature 123

6.3 Zoomed in image of the fitted NEXAFS results of a6T deposited at room temperature 124

6.4 Peakset plots for the a6T room temperature NEXAFS data 125

6.5 NEXAFS data of a6T deposited on a substrate held at 110°C . . . 126

6.6 Peakset plots for the a6T 110 °CNEXAFS data 127

6.7 NEXAFS data of DTDCPB deposited at room temperature 129
6.8 Peakset plots for the DTDCPB room temperature NEXAFS data . 130
6.9 NEXAFS data of DTDCPB deposited at 80 °C 131
6.10 Peakset plots for the DTDCPB 80°C NEXAFS data 132
6.11 NEXAFS data of HB194 deposited at room temperature 134
6.12 Peakset plots for the HB194 room temperature NEXAFS data . . 135
6.13 NEXAFS data of HB194 deposited at 80°C 136
6.14 Peakset plots for the $HB19480$°C NEXAFS data 137
6.15 Optical constants of a6T RT and 110°C films 139
6.16 Optical constants of DTDCPB RT and 80°C films 140
6.17 Optical constants of HB194 RT and 80°C films 142
6.18 GIWAXS images of HB194 and DTDCPB thin films deposited at room temperature and 80 °C 144
6.19 Illustration of the packing of α-6T 146
6.20 Illustration of the packing of DTDCPB 147
6.21 Illustration of the packing of HB194 148

A.1 NMR of two batches of BTIC-H 179
A.2 Preliminary TTR JV data 182
A.3 Preliminary PDIFCN2 JV data 183
A.4 APS data of donors used in BTIC-H PHJ devices 184
A.5 EQE fits for Voltage Analysis 186

List of Tables

4.1 NFA Key Data Summary 94

5.1 Table of key parameters of the JV data from BTIC-H PHJ devices 100

5.2 Table of voltage loss contributions for BTIC-H PHJ devices 104

5.3 Key device metrics for the DCV5T:BTIC BHJ and DCV5T:C60 BHJ devices, calculated from the $J-V$ and EQE results shown in Figure 5.6b and Figure 5.7 respectively. 105

5.4 Table of individual voltage loss contributions for BTIC-H and C_{60} PHJ and BHJ devices using DCV5T as a donor. 109

5.5 Key mean device metrics for the DCV5T:BTIC BHJ HT and DCV5T:C60 BHJ devices, calculated from the $J-V$ results shown in Figure 5.12 114

6.1 Table of key results for orientation analysis of a6T, DTDCPB, and HB194 at RT and HT 145

A.1 Table of values used to estimate the LUMO values of materials used in PHJ devices in Chapter 5 185

List of Acronyms

OSC . . . . . organic solar cells

OPV . . . . . organic photovoltaics

NFA . . . . . non-fullerene acceptor

SE . . . . . spectroscopic ellipsometry

HOMO . . . . . highest occupied molecular orbital

LUMO . . . . . lowest unoccupied molecular orbital

NEXAFS . . . . . near edge X-ray fine structure

DA . . . . . donor-acceptor

D-A . . . . . donor-acceptor

D . . . . . donor

A . . . . . acceptor

GIWAXS . . . . . grazing incidence wide-angle X-ray scattering

OLED . . . . . organic light emitting diode

PCE . . . . . power conversion efficiency

PV . . . . . photovoltaic

VTE . . . . . vacuum thermal evaporation

PVD . . . . . physical vapour deposition

IP . . . . . ionisation potential

EA . . . . . electron affinity

CT . . . . . charge transfer

R-SoXS . . . . . resonant soft X-ray scattering

CS . . . . . charge separated

PHJ . . . . . planar heterojunction

BHJ . . . . . bulk heterojunction

2D . . . . . two-dimensional

3D . . . . . three-dimensional

A-D-A . . . . . acceptor-donor-acceptor

ECHO . . . . . evaporation chamber oxford

QCM . . . . . quartz crystal microbalance

AOI . . . . . angle of incidence

EQE . . . . . external quantum efficiency

BT . . . . . bithiophene

APS . . . . . ambient photoelectron spectroscopy

AFM . . . . . atomic force microscopy

TEY . . . . . total electron yield

CV . . . . . cyclic voltammetry

DLS . . . . . Diamond Light Source

RMS . . . . . root mean squared

MSE . . . . . mean squared error

MSA . . . . . multi-sample analysis

IPES . . . . . inverse photoelectron spectroscopy

OTRACE . . . . . open-circuit corrected charge carrier extraction

LED . . . . . light-emitting diode

DSC . . . . . differential scanning calorimetry

TGA . . . . . thermogravimetric analysis

PL . . . . . photoluminescence

RT . . . . . room temperature

HT . . . . . high temperature

TD . . . . . transition dipole

TDM . . . . . transition dipole moment

a6T or α-6T . . . α-sexithiophene

1 | Introduction

1.1 Motivation

Within the semiconducting field organic electronics occupies an interesting space with a balance of novel and established practices. The organic light emitting diode (OLED) industry, for example, has seen remarkably strong growth in recent years and is currently valued between $40 - 50$ billion USD according some reports and is projected to continue growing [1, 2, 3] and now has established manufacturing practices and methods, mostly within the display market space. While work in the organic photovoltaic (OPV) space on the other hand is not as mature in the industry, there are several companies working on large scale production in addition to the active research present in academia.

Despite the necessity and importance of the role photovoltaics (PV) must play in the race for a globally carbon neutral energy supply, the energy cost of the manufacturing and production of conventional silicon photovoltaics is not negligible, resulting in carbon footprint that, despite being far lower than fossil fuels, cannot be ignored. In addition to production, disposal of old (silicon-based) PV modules is also a concern for this technology, as many materials used in the module assemblies do not allow for climate friendly disposal or recycling. OPVs offer an attractive alternative to the more mature silicon photovoltaic technology in this respect due to low energy costs during manufacturing and easy disposal[4].

In addition to being more climate friendly, OPVs modules can be flexible and lightweight. This opens up many different applications previously unavailable to conventional PV such as reduced transport and installation costs (which are the cause of a significant part of costs of modern PV installations [5]), 3D confor-

mations on non-standard architecture, usage in weight-limited applications such as vehicles or wearable technologies, to name a few. Organic semiconductors are also highly tuneable, and allow for a range of colours and transparencies to be employed. This allows for much more creative and aesthetically pleasing design choices for PV installations or wearables, which can often be an eyesore for communities or individuals. There are currently several start-ups working on developing thin film OPVs, such as Heliatek, NEXT Energy Technologies, ARMOR, and CSEM Brasil.

1.2 What are Organic Photovoltaics?

Organic materials are composed of molecules which primarily comprise carbon and hydrogen. Typically, they also tend to include elements such as nitrogen, oxygen, and sulfur. Some of these materials exhibit optoelectronic properties typically associated with semiconductors, such as their degree of conductivity as well as their (visible) light absorption and emission spectra. These properties make them useful for the fabrication of devices such as light emitting diodes (LEDs), field-effect transistors (FETs) and of course photovoltaic or solar cells (PVs or SCs). Typically we distinguish between these devices made from standard inorganic semiconductors (such as silicon or gallium arsenide - GaAs) and those made from organic semiconductors by adding the term 'organic' to the latter, such as OLEDs, OFETs, and OPVs or OSCs.

Traditional inorganic semiconductors like silicon, germanium, and gallium arsenide have low band gaps; 1.1 eV (Si), 0.67 eV (Ge), or 1.4 eV (GaAs). These low band gaps mean that at room temperature thermal excitation of charges from the valence band to the conduction band results in the appearance of free charges. Typical intrinsic, i.e without dopants, conductivities at room temperature range

from 10^{-8} to 10^{-2} Ω^{-1} cm^{-1}. In addition to this, the dielectric constant in these semiconductors is often around $\epsilon_r \approx 11$, which means that the Coulombic attraction between electrons and holes is low enough that light absorption creates free electrons and holes due to dielectric screening [6].

In organic semiconductors absorption and emission takes place mostly in the range of 2 - 3 eV (roughly 600 - 400 nm), which means that at room temperature thermal generation of free charges is extremely inefficient. Additionally, the dielectric constant is typically much lower than in inorganic semiconductors, usually less than $\epsilon_r \leq 3.5$. This means that the binding energy between an excited electron-hole pair (called an exciton) is significant, and is in the order of $0.5 - 1$ eV. This makes it difficult to separate the charges so that they can flow in the external circuit, and thus charge generation in these devices in inefficient. This challenge is typically overcome by using two different materials, an electron rich 'donor' and an electron poor 'acceptor', with an energy level offset between the molecules respective highest molecular orbital (HOMO) level and lowest unoccupied molecular orbital (LUMO) levels to drive charge separation at the interface between these layers and thus enable efficient charge separation [7]. This simplified concept is illustrated in Figure 1.1, and will be discussed in more detail in Chapter 2. Despite a large catalogue of donor molecules used successfully in the field, the catalogue of successful acceptor molecules has been historically small, comprising mainly fullerene and fullerene derivatives. This has largely been attributed to the excellent electron mobility and 3D nature of the fullerene molecule. Despite its position as the key acceptor molecule in the field, devices using fullerene or fullerene derivatives showcase relatively weak absorption and high energy losses [8]. As a consequence of this, the efficiencies of OPV single-junction devices using fullerene acceptors, fabricated via evaporation or solution processing, have

been capped below the 11% mark [8, 9, 10].

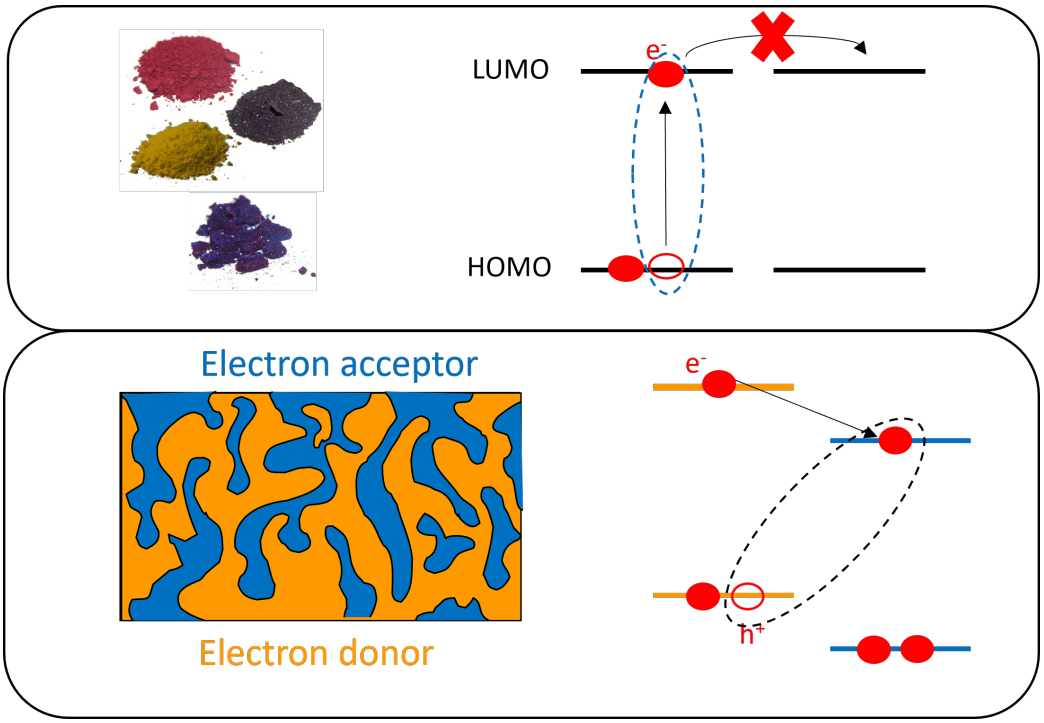


Figure 1.1: Simplified illustration showing that charge separation is inefficient in single organic materials due to the high binding energy of excitons (i.e. electron-hole pairs) generated in these materials. However, when two materials with an energy offset between their respective HOMO and LUMO levels are combined this energy offset can drive charge separation, thus allowing for efficient charge generation in OPV devices.

1.3 Emergence of Non-Fullerene Acceptors

Until 2015 the best PCE for a single-junction OPV was limited to around 10.4% [10] and was enabled by a fullerene derivative and a polymer. However, in recent years the synthesis of a class of molecules known as non-fullerene acceptors (NFAs) utilising a novel acceptor-donor-acceptor type structure have enabled a rapid rise in lab reported PCEs. The first NFA organic solar cell of this kind showed a PCE of around 7% in 2015, made possible by the ITIC acceptor molecule

[11]. The current record PCE of an NFA organic solar cells is certified at around 19.2% [12]. Figure 1.2 shows the molecular structures of the fullerene derivative and ITIC acceptor for comparison.

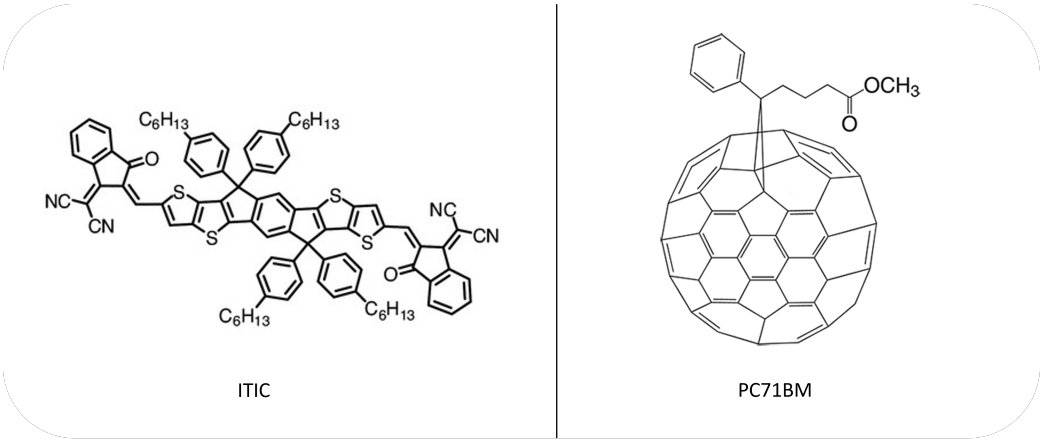


Figure 1.2: Molecular structures of ITIC (left) and $PC_{71}BM$ (right).

1.4 Current Challenges in Organic Photovoltaics

Despite the attraction of OPV for use in the energy industry, the technology has a few challenges to overcome before widespread adoption can be seen. In particular, OPVs exhibit lower efficiencies than those seen by silicon PV and even other novel PV technologies such as perovskite PV, though this gap has narrowed in recent years with current state of the art OPV employing NFAs showcasing around 19% efficiencies [12]. Despite these rapid achievements, OPVs still lag a long way behind traditional silicon (around 26%) and the technology still has a long way to go before it becomes ready for widespread field use. This efficiency gap is illustrated in Figure 1.3 which shows the record efficiencies of major technologies over time.

The synthetic complexity of the molecules, in particular for polymer materials, also requires appropriate supply chains to be established in order for production

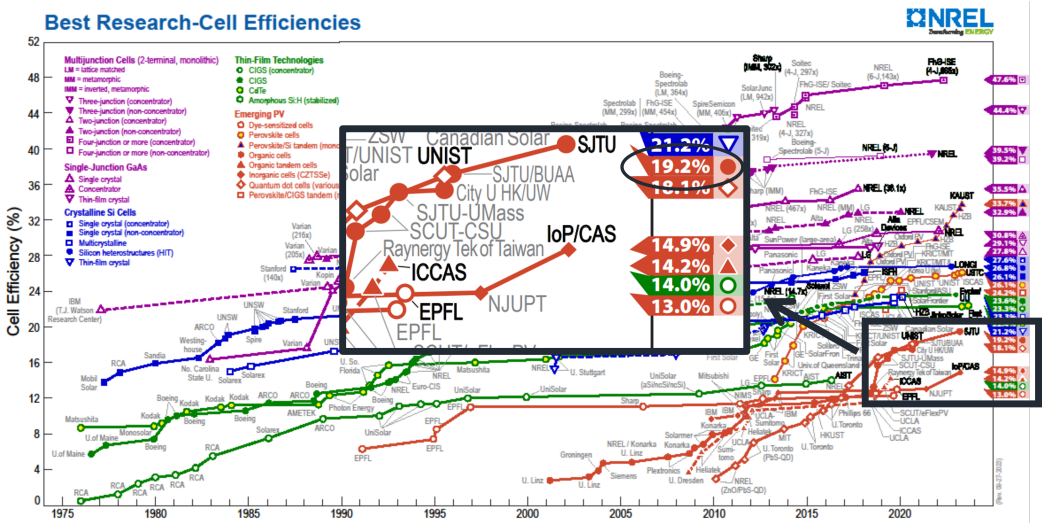


Figure 1.3: NREL chart showing record power conversion efficiencies (PCEs) for various Solar PV technologies. Zoomed in image of most recent single junction efficiency records, with the record PCE for OPV (19.2%) circled in black. This plot is courtesy of the National Renewable Energy Laboratory, Golden, CO.

to be scaled up to ensure cost effective materials. Production of full stack devices is also a chief concern, with current NFAs being only applicable to solution processing manufacturing methods.

OPV samples are made with either solution processing or vacuum deposition, also called vacuum thermal evaporation (VTE) or physical vapour deposition (PVD). Solution processing makes use of wet solvents to disperse the material after which they can be processed into a thin film by various methods such as spin coating, blade coating, etc on substrates. Vacuum deposition involves heating up the material powder in a vacuum to sublime it, resulting in the deposition of the material on a substrate. Solution processing is by far the more popular method to fabricate devices as it offers a low cost and easy to set up production method for research groups. In addition a wider variety of molecular structures can be processed with this technique, including fullerene derivatives, other small molecules, and polymers. However, vacuum deposition is widely used in industry (for example the

production of OLEDs) but is far more niche in research groups since the equipment is expensive to set up and maintain. The materials compatible with vacuum deposition is also limited to small molecules which are relatively simple, often those with molecular weights less than 1000 g/mol. One advantage of this, however, is that these materials are often much easier to purify than their larger and more complex counterparts, especially when compared to polymers.

Despite its advantages, solution processing suffers from several issues during scale up, though several companies are attempting this currently such as ASCA, Sunew, and Epishine on the OPV module front and Brilliant Matters and Ray Energy on the molecular synthesis side of the supply chain. NFAs used in state-of-the-art OPV devices make use of novel design strategies such as more complex side chains and larger molecular backbones with various chemical moieties in order to improve their absorption and charge mobility to allow for more efficient OPV devices. However, these materials are designed primarily for solution processing rather than vacuum deposition, and the molecular structures employed are far too large and complex to be used in vacuum deposition as the molecules would break down before subliming.

1.5 Problem Statement

The use of non-fullerene acceptors in vacuum deposited OPV is something which requires far more attention in the research community. At the time of writing this thesis, there are only a handful of studies that discuss the use of NFAs in vacuum deposited OPV. If these were more common then the technology would be far closer to commercialisation since vacuum deposition is already an industry standard for OLEDs, and the production of OPV via vacuum deposition would not be much different since both technologies use very similar materials.

Given the prevalence of fullerene in OPV prior to the emergence of NFAs discussion about the microstructure, in particular the orientation of the molecules, of the absorbing layer in OPV has centred largely around that of the donor material, often polymers in the case of solution processed OPV, since the spherical nature of the fullerene molecule results in no preferential orientation in thin film. The orientation of polymer units in thin films is also incredibly complex to analyse and as a result the results from such measurements, while still useful when combined with appropriate modelling and analysis, are of limited relevance to device-related studies. In contrast, the microstructure of all small molecule thin films are simpler and therefore measurements of the orientation are more immediately applicable to device-related studies. Given this relevance, in all small molecule thin films with NFAs understanding the relative orientation of both donor and acceptor molecules can yield rich information about the microstructure and provide useful context for device behaviour.

However, the idea of molecular orientation is by itself vague and there can refer to multiple different geometries. For example, depending on the measurement, different length scales of orientation can be probed, such as local orientation in a few molecules in high-resolution experiments or mean orientation in experiments that have larger footprints. Experiments will often yield different results when they are more sensitive to the surface of a thin film or to the bulk of a thin film. In optical measurements the wavelengths probed will also yield information about different structures in the molecules. These differences are often glossed over in the literature.

This thesis attempts to provide a necessary first attempt at using relatively simple and small NFAs in vacuum deposited OPV to assess whether working devices can be made using these materials. Furthermore, an optical study using spectroscopic ellipsometry and near edge X-ray spectroscopy (NEXAFS) is carried out to pro-

vide a more nuanced view on the orientation of molecules in thin film for several different material systems.

1.6 Research Scope

In this thesis several different NFA materials are investigated for use in vacuum deposited OPV. These materials are sourced from collaborating synthesis groups, including the groups of Professor Weiwei Li from the Beijing University of Chemical Technology and Professor Iain McCulloch from the University of Oxford.

The key material properties of evaporated thin films of each material were evaluated. This data was used to inform subsequent tests, in particular the choice of appropriate donors to make preliminary devices. These devices were then investigated and further study was dependant on the performance of these devices. Given material constraints, an extensive and exhaustive study of each material was not possible and therefore an appropriate screening criteria was developed to better inform the choice of experiments, rather than a detailed optimisation study.

This work is particular relevant to the OPV field as the importance of, and need for new types of, NFAs has by now been established by the research community at large. The theme of research has now slowly been shifting towards making NFA devices that more robust and likely to survive under real working conditions rather than lab based environments, and in this context NFAs compatible with vacuum deposition is even more topical since vacuum deposition offers industrially relevant production as well as robust morphologies when compared to solution processed devices [13]. Should vacuum evaporable NFAs become more commonplace a new area within the field will open up, possibly leading to new physics and more industrially relevant research.

In addition, the orientation of several material systems are evaluated using spectroscopic ellipsometry and NEXAFS and the ability to tune these orientations using substrate annealing is also studied.

1.7 Thesis Outline

After reading this chapter it is expected that the reader will have the necessary context to understand the motivation behind the work in this thesis. In chapter two the basic governing principles of OPV are presented. Chapter three will introduce the materials and methods used in this thesis, including a breakdown of different measurement techniques and their respective analyses.

Chapter four will discuss the material characterisation of selected small molecule NFA thin films, and describe the rationale behind selecting BTIC-H from the list for a more in depth investigation. Chapter five will detail the results from a device study using BTIC-H as an acceptor in several OPV devices. Much of these two chapters have been published already in reference [14].

Chapter six will discuss the results from the second half of this thesis, i.e. the orientation investigation of several evaporated donor thin films deposited at different substrate temperatures. The analysis of NEXAFS data combined with data from spectroscopic ellipsometry of evaporated thin films will be presented. Much of the work in this chapter is part of an ongoing paper.

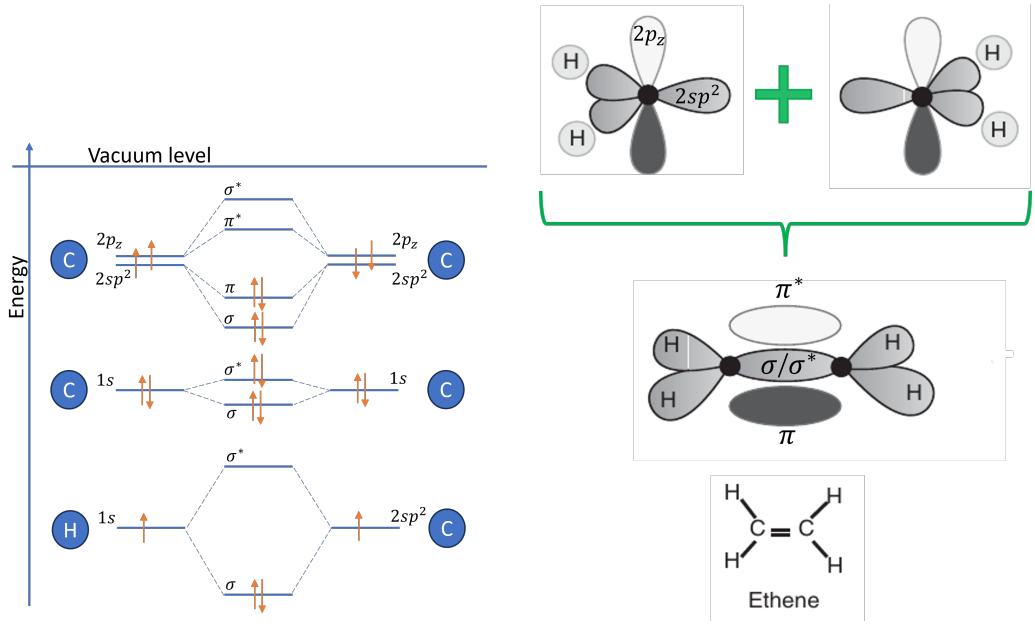
Chapter seven will summarise the key results of this thesis and evaluate the work. The chapter will also make recommendations on future work following up on the results from previous chapters.

2 | Physics of Organic Solar Cells

2.1 Organic Semiconductor Molecules

2.1.1 Energy Levels

Prior to a discussion about organic photovoltaic devices, it is essential to discuss the fundamentals of organic semiconducting materials themselves given the stark differences in the underlying physics between these and their inorganic counterparts.



(a) (b)

Figure 2.1: a) Simple energy level diagram showing the formation of molecular orbitals (center) from atomic orbitals (left and right) with the atomic origin indicated on the sides of the atomic orbitals. Orange arrows indicate the electronic configuration. Adapted from [6]. b) Illustration of the formation of the molecular orbitals of ethene by showing the molecular orbitals of CH_2 (top), the molecular orbitals of an ethene molecule (middle), and the atomic structure of the ethene molecule (bottom).

The energetics of organic molecules plays a crucial role in organic photovoltaic systems. In particular, the alternating single and double carbon-carbon ($C-C$, $C=C$) bonding mechanism plays a critical role in these systems. Briefly, the s and p orbitals of carbon hybridise when in a molecular form, and form molecular orbitals. Of particular interest is the formation of $\pi - \pi^*$ orbitals, which are typically formed from the combination of the $2p_z$ orbitals from adjacent carbon atoms. To illustrate this, consider the case of an ethene molecule. Ethene comprises two carbon atoms, each with two hydrogen atoms bonded to them. Consider first the atomic orbitals present on each carbon atom before they bond together. The electronic configuration is illustrated in Figure 2.1a as follows: each carbon fragment would comprise filled 1s orbitals, and three partially filled $2sp^2$ orbitals, two of which will be shared with $1s$ orbitals from each hydrogen atom, and one partially filled $2p_z$ orbital. As the fragments combine, the carbon $1s$, $2sp^2$, and $2p_z$ orbitals will join and form molecular orbitals. This is illustrated in Figure 2.1b.

The energies of the molecular orbitals can be approximated by a linear combination of atomic orbitals. The details of this calculation are omitted here, with only the solution summarised. The reader is guided to ref [6] for further details. The resulting calculation produces two solutions which give rise to a bonding and an anti-bonding orbital. In the case of ethene, this results in the weak and completely filled σ (bonding) and σ^* (anti-bonding) molecular orbitals from the combinations of the atomic $1s$ orbitals. There is also the much stronger interaction between the two $2sp^2$ atomic orbitals which produce σ and σ^* molecular orbitals of a much larger energy gap, and finally the two $2p_z$ atomic orbitals produce the π and π^* molecular orbitals which have a smaller energy gap than the σ and σ^* orbitals. The π orbital is referred to as the highest occupied molecular orbital (HOMO) and the π^* orbital is referred to as the lowest unoccupied molecular orbital (LUMO). This energy difference is analogous to the the energy gap between the valence and con-

duction bands in inorganic semiconductors and defines the optoelectronic properties of an organic semiconductor in a similar fashion [6]. Koopman's theorem states that the HOMO (LUMO) is equal in magnitude to the ionisation potential IP (electron affinity EA).

Semiconducting organic molecules often consist of series of these types of carbon-carbon interactions, specifically alternating single ($C - C$) and multiple bonds ($C = C$, $C \equiv C$), which merge together to form molecular orbitals which are localised over large regions of the molecule itself. This allows for charges to delocalise across a molecule, thus facilitating charge transport. This is referred to as $\pi - \pi^*$ conjugation.

2.1.2 Absorption and Excitation

The optoelectronic transitions in organic molecules is a complex topic and reader is directed to [6] for a more in depth discussion on this. Key parts and concepts are summarised below.

Absorption and emission light in organic molecules is characterised by the electronic transitions available. This is typically the $\pi - \pi^*$ transition for many organic small molecules (as well as other organic compounds such as polymers), and may also include transitions from other orbitals made available by other chemical moieties or end groups on a molecule, for example nitrogen or oxygen end groups. To a zeroth order approximation, this depends on the spatial overlap between the initial and final state wavefunctions. This is greatly influenced by the chemical structure of the molecule, including which chemical moieties are present, where they are situated along the molecule, and what the overall shape of the molecule is, to name a few, all of which can affect which wavelengths will be absorbed [6, 15]. The individual orientation of molecules plays a crucial role in governing the

absorption of photons, as this affects the orientation of the transition dipole moment with respect to incoming light, leading to more or less intense absorption at similar wavelengths. Absorption peaks are typically broadened rather than sharp lines for organic molecules, and as such the absorption of organic molecules can be modelled as a series of harmonic oscillators [6]. This is largely due to the impact of vibrational, translational, and rotational manifolds in organic molecules [16]. Indeed, the strength of an electronic transition, i.e. the oscillator strength, depends on the transitional dipole moment associated with that transition.

Upon absorption, an electron is typically excited from the HOMO to the LUMO of a molecule, i.e. the molecule is in an excited state. This process creates an exciton, i.e. a bound electron - hole pair, which will be discussed in Section 2.2.2. Depending on the absorption, additional states might also be excited, for example the electron might be excited to the LUMO + 1 or the LUMO + 2 levels, or from the HOMO - 1 level to the LUMO. The lowest energetic excited state is referred to as the S_1 state, with additional states referred to as S_n states. The ground state is S_0. When thinking about molecular orbitals the HOMO and LUMO levels are certainly useful concepts, but can become complicated when discussing excitation dynamics given the multiple configurations of molecular orbitals available. The energy state picture is much more convenient to use for this reason [6].

In addition to singlet states, triplet states consisting of unpaired electrons are also typically possible and referred to as T_n states. These direct transitions from the ground state to triplet states are spin-forbidden and highly unlikely. However, while transitions from singlet states to triplet states are also spin-forbidden, spin-orbit coupling increases the likelihood of this occurring. This process is called inter-system crossing is denoted by the transition rate k_{ISC}. Molecular species with heavy atoms such as ZnPc have stronger spin-orbit coupling, and therefore typically have a higher k_{ISC} than molecular species without heavy atoms [6].

Vibrational levels in organic molecules also play a role in the absorption of light. Excitations into higher vibrational levels of the S_1 state for example are typically possible, and these often thermalise to the zero vibrational state within approximately a picosecond. This is called internal conversion and is denoted by the transition rate k_{IC}. This would affect the spectral shape of the absorption, and would typically manifest in additional peaks. This is dependant on the molecule, with the chemical structure playing a crucial role here. For example, when considering the excitation of the S_1 state, a stiff molecule with rigid bonds might have the $0-0$ absorption peak dominant, but a flexible molecule may have the $0-2$ peak dominant [17, 6]. Another consequence of this rapid thermalisation to the zeroth vibrational level is that fluorescence (the $S_1 \rightarrow S_0$ transition or k_{fl}) is typically red-shifted compared to absorption.

2.2 Organic Thin Films

2.2.1 Energy Level Shifts in Thin Films

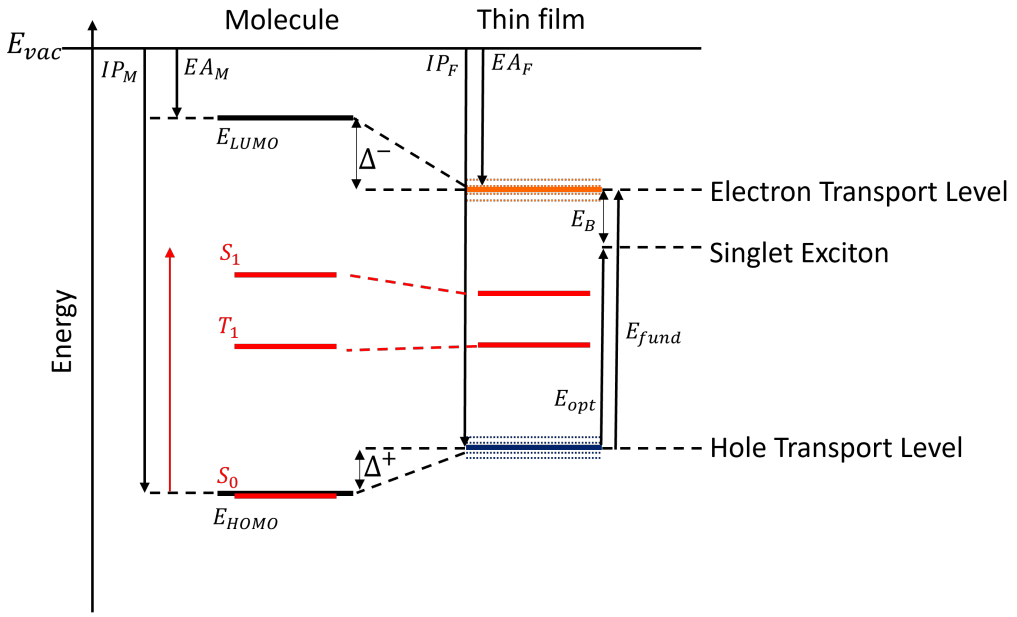


Figure 2.2: A schematic of the energy level shifts which occur when moving from an isolated molecule to a molecular thin film. According to Koopman's theorem the IP describes the energy of the HOMO level (E_{HOMO}) and the EA describes the energy of the LUMO level (E_{LUMO}). The subscript M refers to the case of an isolated molecule and the subscript F refers to the case of a thin film. The difference between the IP and EA is given by the fundamental gap E_{fund} and changes by Δ^- (Δ^+) for the EA (IP). In the case of a thin film the LUMO (HOMO) is the energy level at which electron (hole) transport occurs, and exhibits some broadening due to disorder in the thin film. The first allowed optical transition is given by S_1 and the difference between the ground state S_0 and S_1 is the optical gap E_{opt}. These states are have a different energy scale which is indicated in red, with S_0 arbitrarily set to the E_{HOMO}, and is superimposed on the molecular energy level scale to visualise all the energy levels in a single image. The difference between E_{opt} and E_{fund} is the binding energy of an exciton E_B. Adapted from [18] and [16].

In this thesis the term 'thin film' refers to a film of material < 100 nm (although in should be noted that in the literature this can refer to film thicknesses in the micron regime as well) which is formed when isolated organic molecules condense on a substrate during a deposition process. When the molecules arrive at the surface the molecules experience a weak Van der Waal's interaction with neighbouring molecules (as well as the surface of the substrate) and this causes polarisation effects (U_P) which shifts the energy levels in the thin film when compared to the isolated molecule. This polarisation effect is caused by electrostatic inductions of neighbouring molecules which increase the IP and decrease the EA. Furthermore, charge distributions in the molecular environment also shift the energy levels through electrostatic contributions (U_{el}), affecting the IP and EA equally. These energy level shifts are therefore given by:

$$\Delta^{+} = IP - E_{HOMO} = -U_P + U_{el} \tag{2.1}$$

$$\Delta^{-} = EA - E_{LUMO} = U_P + U_{el} \tag{2.2}$$

Consequently, these energy shifts can result in different absorption and emission spectra of the thin films [6]. Figure 2.2 shows a schematic of how the energy levels shift when going from isolated molecule to thin film.

In an organic thin film these energy levels typically exhibit a fair degree of broadening due to the disordered nature of organic thin films, i.e. the varying intermolecular distances and molecular orientations. This can be described by a Gaussian distribution, referred to as the density of states (DoS), with the width of the distribution characterised by a disorder parameter [6].

As discussed earlier, the orientation of molecules plays a crucial role in the ab-

sorption of incident light. This holds true for thin films as well, and the term preferential orientation is used to discuss the mean orientation of molecules in thin film. The distribution of this orientation also plays a crucial role in the absorption and energetic landscape. An excellent demonstration of this principle is shown in Figure 2.3 taken from ref [19] where the impact of different orientations of the molecule diindeno[1,2,3-cd:1',2',3'-lm]perylene (DIP) can be seen in the optical constants.

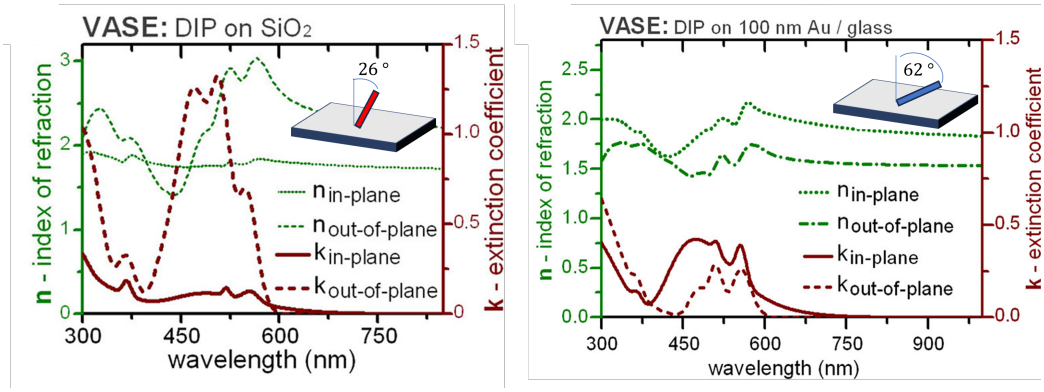


Figure 2.3: In-plane and out-of-plane optical constants of DIP deposited on SiO2 (left) and Au (right). Orientation of the backbone of the molecule for each sample is shown in the top right of the respective plot. Reproduced from reference [19], with the images in the top right of the plots redrawn for clarity.

Due to the disordered nature of organic thin films, all these contributions typically exhibit broadening and actual absorption data often seems to comprise several broadened peaks, of which these vibrational levels would be a part of. Typical examples of this broadening mechanism are H and J type aggregation. H-type aggregation describes groups of molecules stacking in a co-planar manner. This leads to the dipole moments (μ) of the respective molecules adding to form an overall transition dipole moment of either 0 (anti-parallel) or 2μ (parallel). Due to dipole-dipole interactions this splits the energy level into a lower lying energy level which absorption cannot occur into, and an optically allowed higher level

transition which absorption can lead to. This manifests as a blue-shifted peak in the absorption spectra. J-type aggregation describes molecules arranging in a side-by-side manner, with the parallel and anti-parallel arrangements causing a similar splitting except with the lower energy level being accessible through absorption and the higher energy level being inaccessible through absorption. This J-type aggregation consequently manifests as a red shifted peak in the absorption spectra. Additionally, molecules can exhibit an arbitrary angle offset between them which would cause a similar energy level splitting as in H and J-type interactions but each level would be given an oscillator strength given by the vectorial sum of the transition dipole moments of the molecules, resulting in doublet peaks of differing intensities. This is illustrated in Figure 2.4 for the simple case of two individual molecules.

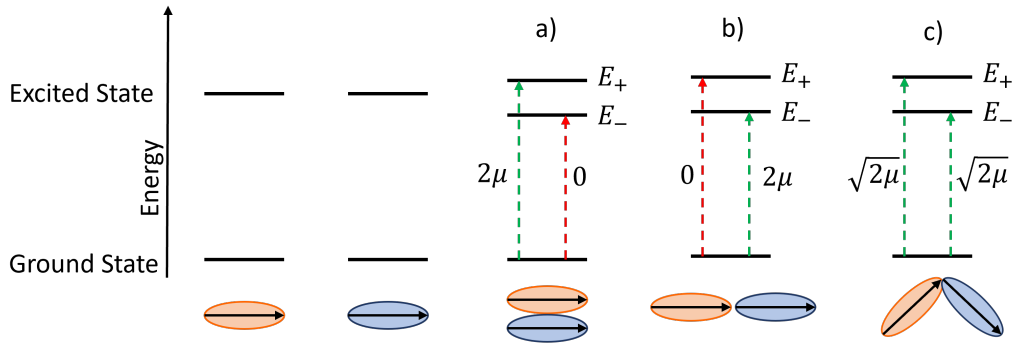


Figure 2.4: Schematic of different arangements of identical molecules leading to energy level splitting caused by different interactions, with transition dipole moments being signified by arrows, green lines indicating optically allowed transitions (caused by parallel molecular arrangements) and red lines indicating optically forbidden transitions (caused by anti-parallel molecular arrangements), with total transition dipole moments for each transition indicated alongside: a) H-type interaction caused by stacked co-planar molecules (parallel arrangement shown), b) J-type interaction caused by a co-linear arrangement of molecules (parallel arrangement shown), and c) an arbitrary angle offset between molecules. Adapted from [6].

It is also important to note that surface environments and bulk environments may

yield different energetics which should be taken into account. It is important to understand which of these environments a measurement is most sensitive to when performing these types of measurements to avoid misleading conclusions. For example, according to ref [20] thin films of the molecule alpha-sexithiophene show that during growth the molecule grows in homogenous monolayers, then switch to an island-like growth mode after $4-6$ monolayers are deposited whereby two distinct phases, an LT-phase and a β-phase grow in equal proportion, and then after 8 nm the LT-phase begins to dominate. The two different phases have different molecular orientations and will consequently affect the absorption of the film. This serves as an excellent demonstration showing that depending on which thickness regime you probe in a film you may obtain very different results.

Processing conditions also play a crucial role in determining the environment of the thin film, and thus the energetic landscape. Stark differences in energy levels have been observed for example between solution, solution processed films, and evaporated films for various systems [13].

From the above discussion it is clear that the energetic landscape of thin films can differ from that of an isolated molecule. Thus, the HOMO and LUMO of the isolated molecules, while certainly useful as starting point for a discussion about energetics, is not sufficient to consider alone when determining the energetic landscape of a thin film. It is essential to determine the energy levels of the thin films themselves in the environment that is most relevant to the device in question, and to be aware of the thickness regime for which the measurements are actually sensitive to, i.e. surface vs bulk.

2.2.2 Exciton Diffusion

As discussed earlier, upon absorption of a photon and subsequent excitation of an organic molecule a bound electron - hole pair, i.e. an exciton is created. The exciton cannot usually be separated into its component charges at room temperature due to the relatively high binding energy between the pair, usually in the order of 100s of meV, due to the low dielectric constant of organic molecules ($\epsilon_r \approx 3 - 5$) [16, 6, 18]. This results in the exciton being localised on a single molecule. The exciton can move between molecules, with the underlying principles governing this movement dependant on the molecular environment, but usually occurs between $5 - 40$ nm [21, 22, 23, 24]. Often, organic thin films comprise a mix of disordered and ordered regions with exciton diffusion commonly taking place either radiatively by the emission and reabsorption of photons from excited molecules - called trivial transfer, or non-radiatively through Förster type energy transfer. This non-radiative transfer is mediated by the Coulomb interaction between molecules, allowing for an excited molecule to de-excite and subsequently cause a ground state molecule to excite via a Coulomb coupling interaction [6]. These types of excitons are called Frenkel excitons.

In highly crystalline materials such as inorganic semiconductors with high dielectric constants ($\epsilon_r \geq 12$) excitons are much more weakly bound, are mobile within a lattice, and can span a large distance compared to the inter-atomic spacing ($r \approx 5 - 10$ nm). These are called Wannier excitons and can freely dissociate into free charges provided their binding energy is less than the thermal energy available to the system at room temperature [6].

2.3 Organic Solar Cells

We have so far discussed the case of single organic molecules and organic molecules in thin film. In an organic solar cell (OSC) while much of the physics discussed thus far holds true the environment is changed slightly due to the addition of electrodes and transport layers on either end of the active layer, i.e. what has been referred to as the thin film. Figure 2.5 shows an illustration of a full device stack, including transport layers, which serve the main purpose of enhancing charge transport to the electrodes as well as serving as a buffer layer to reduce templating effects or material damage from the metal electrode deposition.

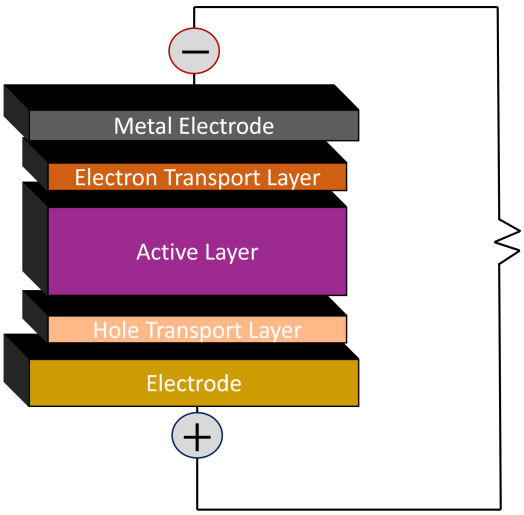


Figure 2.5: An illustration of a device stack consisting of an active layer sandwiched between an electron and a hole transport layer with electrodes on either end, in an electrical circuit with a load.

2.3.1 Charge Transfer at the Donor Acceptor Interface

As highlighted in the previous section, excitons created in organic thin films are called Frenkel excitons and experience a high binding energy which makes spontaneous dissociation highly unlikely since $E_B >> k_BT$ [6]. In fact, dissociated

states do exist in single component organic films but the energy of the dissociated state typically lies 0.5 eV above the S_1 state [6]. As a way to overcome this limitation Tang introduced the idea of a heterojunction where an interface is created with two different materials with offset energy levels such that they create a energy gradient, i.e. one material is an electron donating molecule (the donor) and one is an electron accepting molecule (the acceptor) [7]. This allows Frenkel excitons to delocalise across a donor-acceptor (D-A) interface, which has a lower binding energy and thus has a higher dissociation probability. This can occur through electron transfer where the Frenkel exciton is initially localised on the donor and an electron in the LUMO of the donor transfers to the LUMO of the acceptor. The CT state can also form through hole transfer, where the Frenkel exciton is initially located on the acceptor and the hole in the HOMO of an acceptor molecule transfers to the HOMO of the donor. This delocalised state is referred to as the charge transfer (CT) state. These CT states can also be reached directly from the ground state through photon absorption [25, 26, 27]. CT states formed via exciton diffusion to a D-A interface are considered ultra-fast transitions (k_{CT}) and occur in the order of $20 - 300$ fs [28] Recent work has suggested that in well performing non-fullerene acceptor systems where there is a small offset in energy levels between donor and acceptor the CT state formation actually occurs through Förster resonance energy transfer [6] from the donor molecule to the NFA, after which the hole on the NFA transfers back to the donor [29].

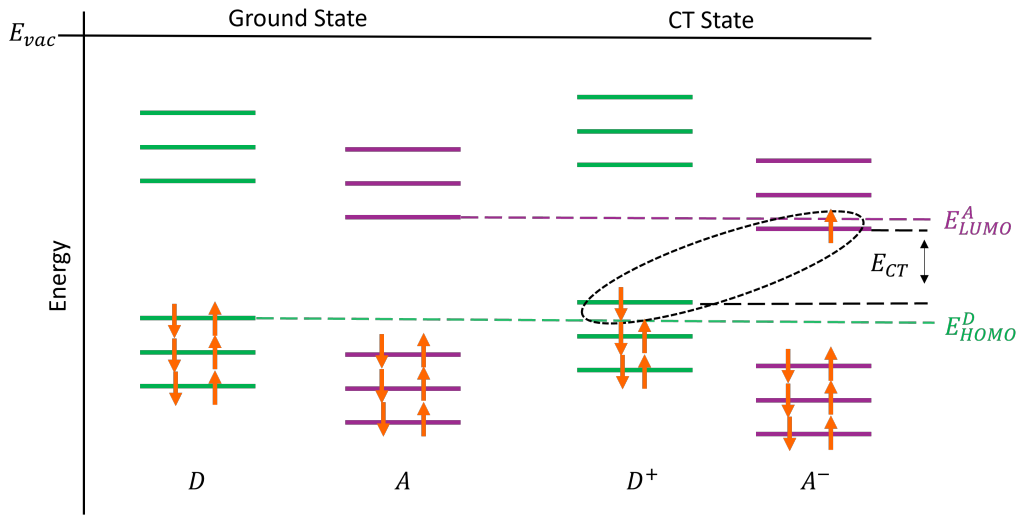


Figure 2.6: An illustration of CT state formation at a DA interface. Shown on the left is the ground state, where the HOMO and lower energy levels of both donor and acceptor are filled and the LUMO energy levels are empty. Shown on the right is the situation at charge transfer, where an electron from the donor molecule is located in the LUMO of the acceptor molecule. The DA complex undergoes some reorganisation such that the energy of the CT state (E_{CT}) is less that the difference between the the energy of the acceptor LUMO and the donor HOMO ($E_{CT} < E^A_{LUMO} - E^D_{LUMO}$). Adapted from [16].

Once the CT state is formed the energy levels of the D-A complex shifts slightly as the molecules rearrange themselves to accommodate the new charge distribution. This is referred to as the reorganisation energy and further increases the likelihood of dissociation. The energy of the CT state is less than the E_{S_1} of both donor and acceptor molecule. Figure 2.6 illustrates this concept. The CT state can recombine radiatively through photon emission to the ground state with transition rate $k_{CT,rad}$, or non-radiatively with transition rate $k_{CT,nr}$.

The concept of a D-A heterojunction first manifested in vertically stacked layers, which were known as planar heterojunctions (PHJs) [7]. If the donor and acceptor materials were chosen such that a favourable energy offset exists the dissociation at the interface is efficient, provided that the excitons can reach the interface

[30]. For many organic materials the absorption depth is typically ≈ 100 nm but exciton diffusion lengths, as stated earlier, are typically $5 - 40$ nm [21, 22, 23, 24]. This places a limit on how thick D-A heterojunctions can practically be, and consequently results in poor photocurrents due to the reduced absorption from thinner layers or excitons failing to reach a D-A interface to dissociate. This issue was circumvented by the introduction of an intermixed heterojunction rather than a vertically stacked heterojunction. These heterojunctions are called bulk heterojunctions (BHJs). By making a intermixed D-A heterojunction the interface is distributed throughout the layer, which increases the probability of excitons reaching a dissociation site , i.e. an interface.

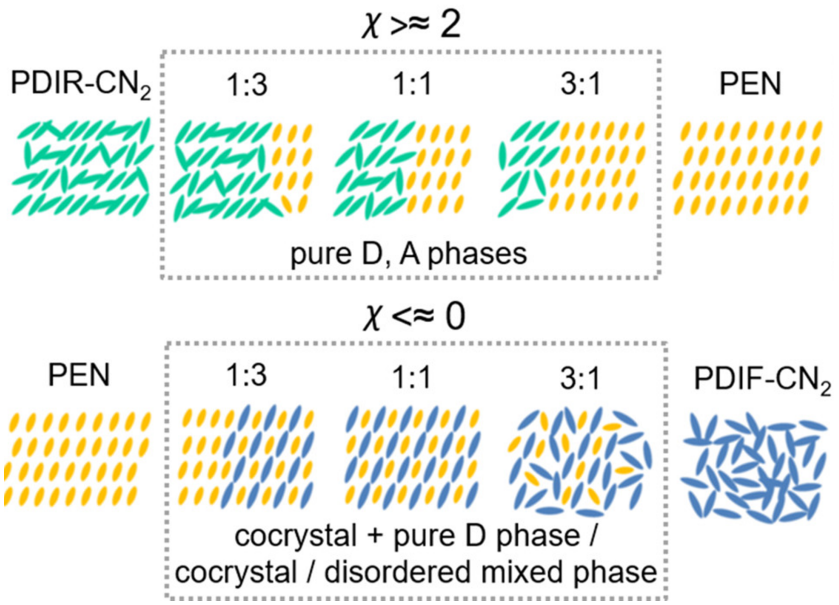


Figure 2.7: An illustration of the impact of different values of the interaction parameter χ on mixing of small molecule blends. Shown above are blends of the molecule pentacene (PEN) and a perylene diimide derivative PDIR-CN2. Shown below are blends of a different perylene diimide derivative PDIF-CN2 and pentacene. Blends are shown at different mixing concentrations. Image taken from [31].

The morphology of the D-A layer, also called the absorbing layer or the active

layer, has a significant impact on the overall performance of a device [32, 33, 34]. The general consensus is that large amounts of both acceptor and donor molecules are required to produce good devices as more interfaces would result in more dissociation. Aggregation of donor and acceptor molecular species would create percolation pathways in a blend to ensure good charge transport. However, some studies show that dilute blends ($< 10\%$ donor loading) with certain donor molecules and fullerene as an acceptor, perform better than more equivalently loaded blends [35, 36, 25]. These findings highlight the dual-nature of D-A interfaces; on the one hand they allow for excitons to dissociate into free charges, but on the other they provide a site for free charges to meet and recombine. There is a balancing act that must happen and the relative impact of each of this processes differs greatly between different D-A systems.

It is clear that the mixing of the D-A blend plays a crucial role in determining the nature of the interface. This miscibility is characterised by the Flory-Huggins interaction parameter χ. This parameter can be calculated by a nearest-neighbour interaction model where the main driving force of aggregation is the difference between donor-donor (W_{DD}), acceptor-acceptor (W_{AA}), and donor-acceptor (W_{DA}) interactions. The calculation is given by [31, 37]:

$$\chi = \frac{Z}{k_B T} \left(W_{AA} + W_{BB} - 2W_{AB} \right) \tag{2.3}$$

where Z is the coordinate number corresponding to the number of lattice sites for the molecules, k_B is the Boltzmann constant, and T is the temperature of the system. For different values of χ different morphologies are created [34, 38, 39, 31]. An example of this is shown in Figure 2.7 from ref [31] for blends of the molecules pentacene with perylene diimide derivatives PDIF-CN2 and PDIR-CN2. While quantifying the interaction parameter in solutions is relatively well

understood through Flory-Huggins solution theory, applying this to organic photovoltaic blends is made even more complex by the impact of the deposition process on the final morphology of the DA blend, as a result analyses using the interaction parameter is usually qualitative rather than quantitative although there have been some advances made in quantifying the interaction parameter in recent years using resonant soft X-ray scattering (R-SoXS) [34].

2.3.2 Charge Generation and Recombination

So far we have discussed how absorption of photons in organic thin films leads to the creation of Frenkel excitons which diffuse to the D-A interface and form CT excitons, known as the CT state. Alternatively upon photon absorption an electron is excited directly into the CT state. Now we will discuss how the CT exciton dissociates into free charges, i.e. how the CT state leads to the charge separated (CS) state. This is known as charge generation. Once free charges are created they can be collected at the electrodes. Figure 2.8 shows the various states and processes leading to charge generation in OSCs.

The internal quantum efficiency, i.e. the ratio of excitons generated to charges collected at the electrodes, of many well performing OSC systems is near unity [40, 41]. This means that almost all generated excitons dissociate into free charges in these systems. Historically, the primary factor influencing this process was thought to be the energy offset at the D-A interface, typically referred to as the 'driving force', and that large driving forces were needed to ensure efficient dissociation. The driving force is calculated as the energy difference between the LUMO of the donor and the LUMO of the acceptor for electron transfer-mediated systems and the HOMO of the acceptor and the HOMO of the donor for hole transfer-mediated systems. Alternatively, the energy difference between the S_1 state and the CT state are also used to determine the driving force, depending on

what picture is used to describe this process. Assuming efficiency charge collection, this results in a trade-off between having high photocurrents and conserving chemical potential of the system (V_{OC}). This is often described as the $EQE{-}V_{OC}$ trade-off in the literature [42, 43], where EQE stands for external quantum efficiency and refers to the ratio between incident photons and collected charges. This paradigm has been challenged by recent studies on NFA systems with high photocurrents and low driving forces [44, 45, 46].

Once CT states form they can dissociate into CS states with rates k_{diss} on the order of 100 fs to ns [47, 48, 49]. The exact model for the CT to CS process is still under debate, but it is generally accepted that the process is enabled by the gradual reduction in the Coulomb force between the electron-hole pair which comprises the exciton as the distance between the electron-hole pair increases. References [6, 47, 50, 51, 52, 53] contain various models that have been proposed, and in particular references [50] and [6] provide a review of the most prevalent models. Once a CS state is formed the charge needs to travel to an electrode to be collected. The only loss mechanism here is the recombination between an electron and a hole. Recombination events are classified as geminate if the event occurs between an electron and hole which originally comprised the same exciton, and non-geminate if they originate from distinct excitons. CS states can recombine non-geminately back into CT states with the rate k_{form} or to the ground state with the rate k_{CS}. CT states formed through k_{form} can be of singlet or triplet character. Consequently, CT states can also decay non-radiatively to a triplet state through back charge transfer (k_{BCT}). k_{form} and k_{CS} should be relatively low in a PHJ because electrons are located on the acceptor and holes on the donor, i.e. they are spatially separated from each other. In a BHJ, however, k_{form} and k_{CS} are likely to be higher because the DA interface is distributed throughout the film and the chances of non-geminate recombination are greatly increased [16].

Recombination events discussed earlier all occur geminately.

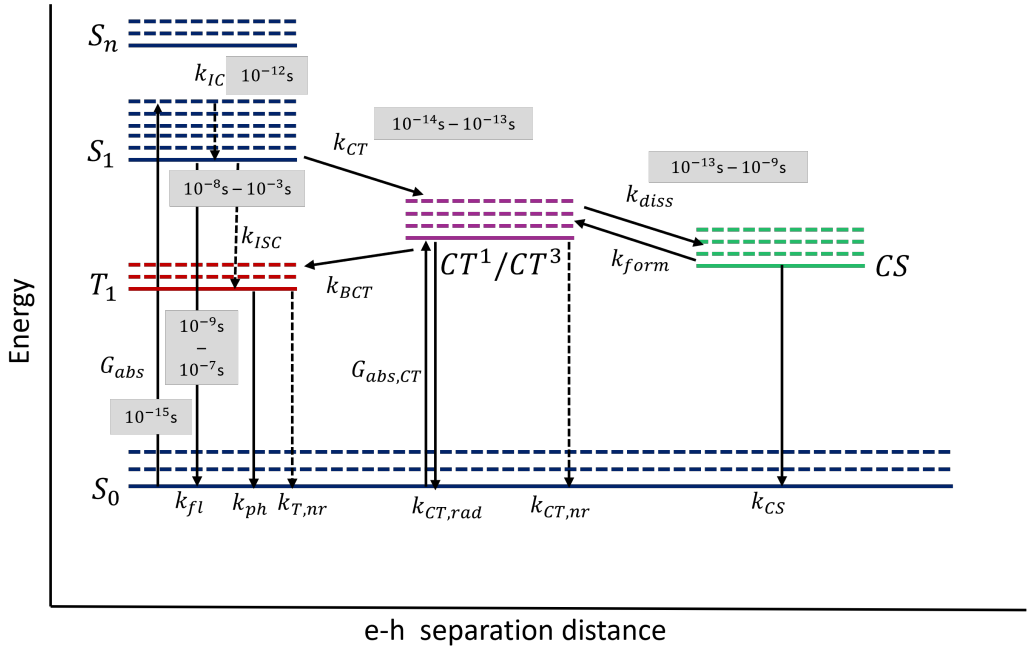


Figure 2.8: A Jablonski diagram of the key processed in OSCs. Timescales of the processes are indicated in boxes over the relevant processes and are taken from [16, 47, 28]. Solid arrows indicate radiative transitions. Dashed arrows indicate non-radiative transitions. Singlet states can be excited through photon absorption with rate G_{abs}. Higher energy singlet states S_n may also be excited, and will thermalise to the first excited state via internal conversion with rate k_{IC}. Singlet states can recombine to the ground state S_0 radiatively with rate k_fl. They can also decay to triplet states (T_n) via inter-system crossing with rate k_{ISC}, from which they can recombine non-radiatively to S_0 with rate $k_{T,nr}$ or radiatively with rate k_{ph}. Singlet states can form CT states at a DA interface with rate k_{CT}. CT states can also be excited directly with rate G_{CT}. CT states can recombine radiatively with rate $k_{CT,rad}$ or non-radiatively with rate k_{CT_nr}. They can also form CS states with rate k_{diss}. These CS states can reform CT states with rate k_{form}, which may be triplet in character. If so, they can decay to triplet states T_n via back charge transfer with rate k_{BCT}. CS states which do not recombine can be extracted at the electrodes (not shown in the diagram). Adapted from [41].

2.3.3 Current Density-Voltage Characteristics

The voltage dependence of the photocurrent ($J-V$ characteristics) in solar cells is a complex topic, and reference [16] provides a detailed discussion about it. A brief overview is presented in this section.

The $J-V$ characteristics of (inorganic) p-n junctions under illumination was derived by Shockley [54]:

$$J(V,T) = J_0 \left(exp(\frac{qV}{nk_BT}) - 1 \right) - J_{ph}(V) \tag{2.4}$$

where J_0 is the dark saturation current, q is the elementary charge, k_B is the Boltzmann constant, T is the temperature of the diode, n is the ideality factor, which typically ranges between 1 and 2 depending on the dominant recombination pathways, and J_{ph} is the photocurrent density. In conventional inorganic semiconductors it is often assumed that J_{ph} is independent of an applied external field and thus that the photocurrent density is equivalent to the short-circuit current density J_{SC} such that $J_{ph} = J_{SC}$. However, in organic semiconductors this assumption does not always hold, as a strong voltage dependence of the photocurrent can often be observed [16]. The primary reason for this is likely low charge-carrier mobilities which lead to charge populations which partially screen the applied external electric field. There have been many attempts to appropriately model these effects to more accurately derive the $J-V$ characteristics within organic semiconductors[16], but it is out of scope for this discussion.

Using Equation 2.4 an expression for the open circuit voltage V_{OC} , i.e. the voltage under illumination where there is no current extraction such that $J = 0$, can be derived:

$$V_{OC} = \frac{k_B T}{q} ln\left(\frac{J_{ph}}{J_0} + 1\right) \approx \frac{n k_B T}{q} ln \frac{J_{ph}}{J_0} \tag{2.5}$$

The term inside the natural logarithm, $\frac{J_{ph}}{J_0} + 1$, can be approximated to $\frac{J_{ph}}{J_0}$ because the photocurrent produced while under illumination is working solar cells is far greater than the dark saturation current [16].

The electrical power produced by a solar cell under illumination, P, is given by:

$$P = I \cdot V = J \cdot A \cdot V \tag{2.6}$$

where I is the total current which increases with the active area A of the device. The fill factor (FF) is a key metric when analysing the performance of a solar cell, and is often qualitatively seen as the squareness of the $J - V$ curve and is given by:

$$FF = \frac{J_{MPP} V_{MPP}}{J_{SC} V_{OC}} \tag{2.7}$$

where J_{MPP} and V_{OC} are the current density and voltage at the point in the $J - V$ curve where the power is at the maximum. Finally the power conversion efficiency (PCE) describes how efficiently illuminating light is converted into electrical power and is given by:

$$PCE = \frac{J_{SC} V_{OC} FF}{P_{in}} \tag{2.8}$$

here P_{in} is the total power of the incident light, typically 100 mW/cm^2 for the AM1.5G solar spectrum.

The parameters discussed above are key metrics used when assessing the performance of solar cells.

2.4 Development of NFAs in OPV

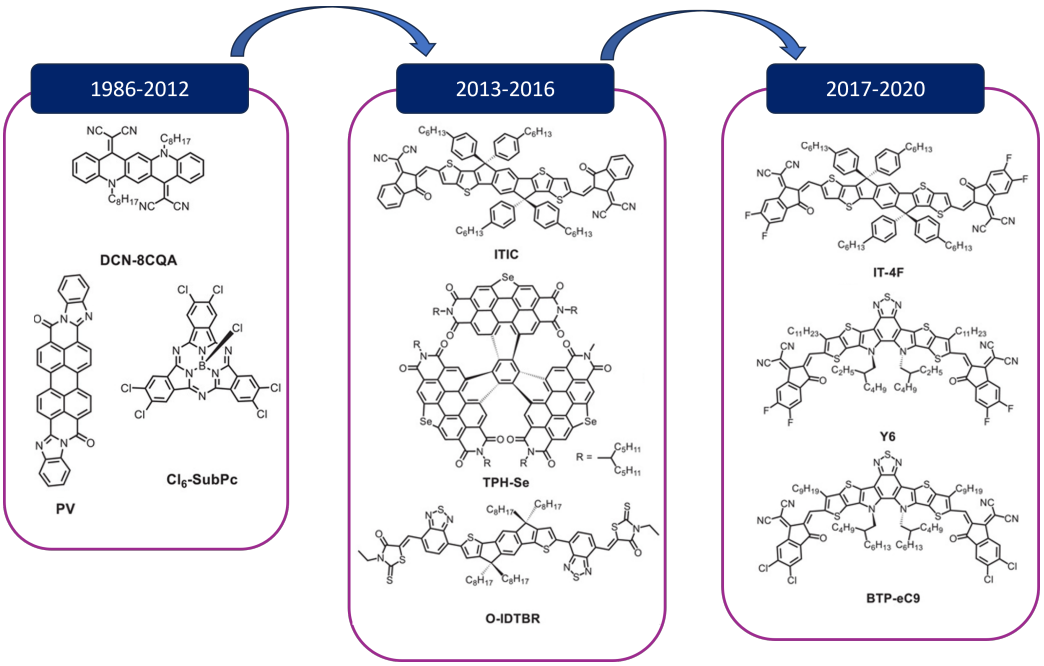


Figure 2.9: A timeline showcasing notable NFA molecules designed during the periods 1986-2012 (small, planar 2D like acceptors), 2013-2016 (larger structures with 3D like structures featuring backbone twists and/or extended side-chains, and 2017-2023 (large and complex A-D-A type structures). Adapted from [8].

The first published heterojunction OSC was made using CuPc and a non-fullerene molecule called PV. This device was vacuum deposited as a PHJ and yielded a PCE of $\approx 1\%$ [7]. Since then the field has certainly come a long way with current efficiencies of NFA OSC devices knocking on the door of the 20% milestone [12]. However, NFAs were not always the acceptor that came to mind when conceptualising organic heterojunctions. Soon after solution processed BHJs were introduced to the research community [55] in 1995 fullerene and its derivatives dominated the acceptor space, and arguably continued to do so until the advent of the A-D-A NFAs in 2015. During this period the design of NFAs could be seen as going through three phases of development [8]. The first phase began in 1986

with the introduction of the heterojunction by Tang using the NFA PV and ended with fullerene being the acceptor of choice for OSCs. The second phase began as performance of fullerene OSCs stall and interest in alternative acceptors pick up. Several novel NFA structures were created during this phase, notably the A-D-A type acceptor ITIC [11]. By the end of this period in 2016 NFA OSCs [56, 57, 58] developed to the point where they could compete with the best fullerene OSCs [10]. Finally from 2017 till 2023 there has been a rapid rise in PCEs for NFA OSCs, leaving fullerene OSCs far behind, with the highest performing OSC to date achieving a PCE of 19.2%. Figure 2.9 shows key molecular structures developed during these phases. The below sections will expand on these development periods.

2.4.1 1986-2012

In the early stages of OPV research various conjugated molecular acceptors were explored. General guidelines for molecular design were a deep EA, high mobilities, and large extinction coefficients [8]. The first acceptor material used in a published OSC was a perylene diimide derivative called PV, which was combined with copper phthalocyanine (CuPc) as a donor in a vacuum deposited PHJ device yielding a PCE of $\approx 1\%$ [7]. Shortly after this further advancements including new molecular designs, such as novel perylene diimides and subphthalocyanines, and new fabrication methods, such as producing BHJs via vacuum co-deposition [59] and solution processing [55], were made which further progressed the field.

In particular, the invention of solution processed BHJ in 1995 [55] played a key role in opening up new ways of fabricating devices through solution-processing, thereby expanding the field greatly. During this time fullerene and fullerene derivatives became the acceptors of choice for organic solar cells due to their ease of processing and compatibility with a wide range of donors [8]. However,

fullerenes typically exhibit poor light absorption in the visible regime, which was a key limiting factor in the progression of OSCs and prompted further exploration for new acceptor structures with only limited success. The best performing NFA OSC devices from this phase of development exhibited PCEs with $\approx 3\%$ for both vacuum processed PHJ devices using chlorinated subphthalocyanines as both acceptor and donor [60] and solution processed devices using perylene-pyrene bismide and a small molecule donor [61].

This period of NFA development (1986 - 2012) greatly expanded the global research community's knowledge of structure-property information for improved NFA design frameworks. In particular, strong electron withdrawing moieties such as chlorine, cyano, and fluorine were identified to be excellent at creating deep LUMOs and fused ring backbones were found to enhance $\pi - \pi$ stacking and electron mobilities. Key challenges identified in these NFAs were strong aggregation and poor overall morphology in blends, despite showing stronger absorption than fullerene [8, 62]. Consequently, fullerene retained its position as the acceptor of choice at the end of this development period, largely due to its combination of favourable energetics (deep lying energy levels), high mobility, and a 3D spherical structure that led to favourable morphology in blends, which is beneficial for charge generations and extraction.

2.4.2 2013-2016

The next phase of development focused on addressing the poor morphology of NFAs in blends. This was primarily achieved by moving from planar, 2D-like molecular structures to more 3D structures. Two key structural levers in particular were identified and explored, namely the use of twists in the backbone and the use of bulky, extended side-chains which featured strong out-of-plane structural components. Key successes during this development period include the novel ac-

ceptors ITIC, TPH-Se, IDIC, and O-IDTBR which showcased PCEs of $7 - 11\%$ [57, 11, 56, 58], competing with the best fullerene devices [10, 8]. These successes were largely attributed to the aforementioned structural features which suppressed excessive crystallinity in devices, as well as excellent light absorption with extinction coefficients $\kappa > 1$ [8, 63]. Furthermore, the use of an acceptor-donor-acceptor structure in molecules like ITIC, IDIC and O-IDTBR demonstrated excellent potential and prompted further research in this direction in the next phase of NFA development [8]. It should be noted that the advancements in NFA designs made during this period were largely limited to solution processed applications, primarily with polymer donors. Many of the improved designs were structures that were too large for use in vacuum deposition, and molecular synthesis research (in OPV) was heavily biased towards solution processing applications.

2.4.3 2017-2023

The most recent period of NFA development has seen rapid gains in performances of OSCs, with latest records reaching 19% [12, 64]. This has largely been due to extensive experimentation with the core, end, and side chain units of A-D-A type acceptors, for example the extension to A-D-A-D-A structures, as well as the use of additives to fine tune the morphology in the blends. These modifications have resulted in a host of NFAs with excellent visible-to-near-infrared light absorption, efficient molecular packing, good charge-transport, and the right degree of miscibility with multiple donor materials [8]. Notable molecules developed during this period include IT-4F [65], Y6 [66], and BTP-eC9 [46]. NFA OSCs at this point have far surpassed even the best fullerene OSC devices. However, these advancements have been largely constrained to solution processing fabrication routes again, for much the same reasons as noted earlier.

2.4.4 Towards Vacuum Evaporable NFA structures

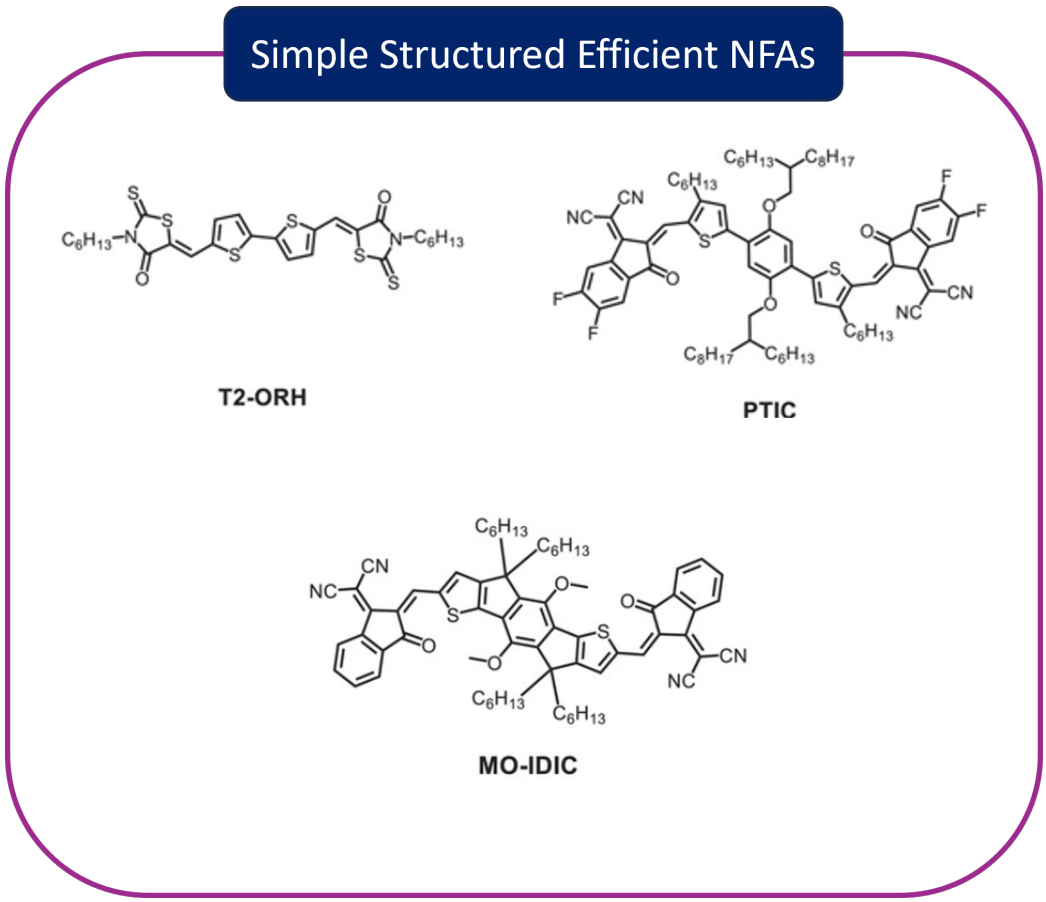


Figure 2.10: Several simple NFA structures which have been used in well performing NFA OSC devices, namely T2-ORH, PTIC, and MO-IDIC. Adapted from [8].

Modern NFA molecules to date have been largely designed for solution processing and contain extended side chains, large molecular backbones, and an overall molecular weight $>$ 1000 g/mol. These properties often make them unsuitable for vacuum deposition as bonds in these comparably large molecules break before they sublime. As a consequence of the current design paradigm, VTE OPV technology has not yet unlocked the advantages of NFAs. This represents a missed opportunity for the OPV field [67]. There are few examples of VTE NFAs in recent

years [68]. Notable examples include the phthalocyanine-based triple planar heterojunction $\alpha-$6T/SubPc/SubNc device which was able to achieve a PCE of 8.4% without C_{60} [69], and more recently devices made with the A-D-A molecule CBD which achieved a PCE of $\approx 0.86\%$ but low voltage losses of ≈ 0.7 V [70]. Despite these promising results, there is little activity in the design of VTE compatible NFAs and in particular A-D-A structures which have brought great progress on the donor side of VTE suitable molecules and for the acceptor side of solution processing.

A possible design route for vacuum evaporable NFAs could be to follow the design paradigm of low molecular weight NFA structures. These are molecules which have largely emerged since 2018 with far smaller core structures. The rationale for this design route is to simplify the synthetic process of NFAs, which has grown far more synthetically complex alongside the structural complexity, often driving up production costs. Notable molecules within this category include MO-IDIC [71], T2-ORH [72], and PTIC [73], which showcased respectable PCEs in the $9-14\%$ range. These structures are shown in Figure 2.10. These molecules are designed for solution processing but are substantially smaller than the other NFAs discussed in the previous sections and many of them, or their derivatives, may yet be compatible with the vacuum deposition process. In Chapter 4 some molecules from this category are explored, namely BTIC-H [74] and T2-ORH derivatives TTR and TTIC4F.

3 | Methods and Materials

3.1 Methods

3.1.1 Sample Fabrication

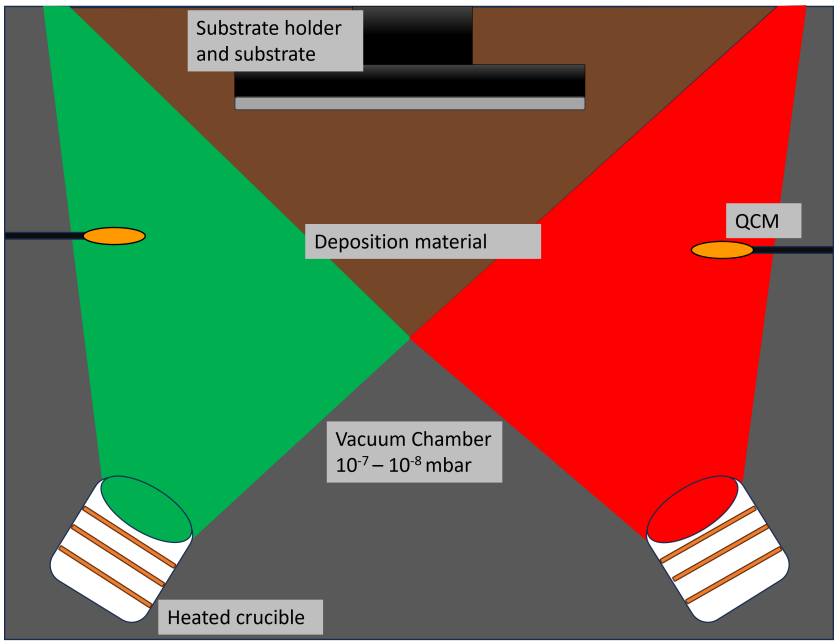


Figure 3.1: Illustration of the vacuum deposition process. The material is loaded into a crucible which is in a vacuum chamber that is pumped down to $10^{-7} - 10^{-8}$ mbar. The crucible is heated to the sublimation temperature of the loaded material and the material is evaporated outwards in a cone from the aperture of the crucible. A substrate is mounted on a substrate holder in the path of the deposition, and the film is deposited in this way. A quartz crystal microbalance (QCM) lies in the path of the deposition with which the thickness of the deposited film on the substrate is measured. In the case of a single film one material is sublimed, a blended film can have multiple materials sublimed simultaneously (indicated by the two crucibles), and in a multilayered film different materials are sublimed one at a time.

Thin films samples used in this thesis were fabricated in one of three different vacuum deposition systems, namely the B40 evaporation tool, the Evaporation Chamber Oxford (ECHO), or the National Thin Film Cluster facility. The B40 is

the smallest of the tools and comprises only four organic sources and was used for the first deposition trial of NFA materials investigated in this thesis. The deposition area of the tool is 56×56 mm. ECHO is a far more complex chamber with six organic sources as well as metal deposition source and is connected directly to a glovebox to ensure that samples fabricated can be transferred stored without seeing atmosphere. Samples can also be deposited on heated substrates up to 150°C. ECHO has a similar deposition area as the B40, and was used to make further samples, including pristine films, blended films, and devices. Finally the National Thin Film Cluster facility is a multi-purpose, multi-chamber deposition tool. It was used to fabricate pristine and blended films in more systematic studies, for example the samples used in Chapter 6, which is enabled by its larger deposition area of 150×150 mm.

Regardless of the tool used, the principles of vacuum deposition are the same. An illustration of a deposition in progress is shown in Figure 3.1. First, material powders are loaded into ceramic crucibles, which are placed in organic sources, i.e. crucible holders consisting of heaters for the crucibles. These are shielded with retractable metal plates. Once the material is loaded the chamber is pumped down with the use of both a roughing pump (Pfeiffer GmbH, ACP15) and a turbomolecular pump (Pfeiffer GmbH. HiPace 700) to $\approx 10^{-5}$ mbar and vented back to atmospheric pressure with N_2 gas. Prior to loading, substrates are cleaned by sonication in a Hellmanex soap solution ($< 2.5\%$ concentration), then in a deionised water bath, then in an acetone bath, and finally an isopropanol bath for 10 min each. Finally the substrates are cleaned with O_2 plasma for 10 min to remove any surface contaminants. Substrates are then loaded in from the N_2 filled glovebox, to preserve their clean state, into a substrate holder which is placed at some distance away from the organic sources. Once the substrates are loaded the chamber is sealed and pumped down to $10^{-6} - 10^{-7}$ mbar. The crucibles are gradually

heated until the material inside sublimes at a steady rate, after which a shield for the deposition area, often referred to as the sample shutter, is opened to allow the material to deposit onto the substrate. There are also quartz crystal microbalances (QCMs) in between the organic source and the substrate, which are used to monitor the film thickness during the deposition. The QCM can detect material mass deposited on it, which is converted in the QCM controller to a thickness using a user input thin film density, which is then used to estimate the thickness on the substrate using a calibrated tooling factor. This allows for real-time monitoring of the thin film thickness and deposition rate. QCMs are only visible to specific organic sources to allow for the independent monitoring multiple sources during a deposition without cross-talk, which allows for the controlled deposition of blended films. Based on manufactures specifications the noise on the deposition rate is $\pm 5\%$. Deposition rates used in this thesis are between 0.1 Å-0.3 Å.

OSC devices fabricated in this thesis follow the same above process, depositions involved multiple layers. Substrates were glass coated with 140 nm of pre-patterned indium-tin oxide (ITO) which were cleaned as described above. The first layer deposited is 3 nm of MoO_3 ($0.05 - 0.1$ Å/s), followed by whatever active material is used in the device. This could be a single layer, a co-deposited blend as used in BHJ devices, or a sequentially deposited bilayer as used in PHJ devices. Each material in the active layer would be deposited at a rate of $0.1 - 0.2$ Å/s. This is followed by 8 nm of BPhen ($0.1 - 0.2$ Å/s), and finally 100 nm of Al ($1 - 2$ Å/s). Once the deposition is complete and the sources cooled down the vacuum chamber is opened to the glovebox and the samples are transferred in, where the substrates are encapsulated. The encapsulation process involves applying a glue to the edges of a glass cover slip with an indent to provide a pocket of empty space for the device area. The cover slip is then carefully lowered over the substrate. Pressure is applied and the glue is exposed to UV light for around 5 min

to cure the glue. The device area is masked to prevent any damage from the UV light.

3.1.2 Thin Film Characterisation

Spectroscopic Ellipsometry

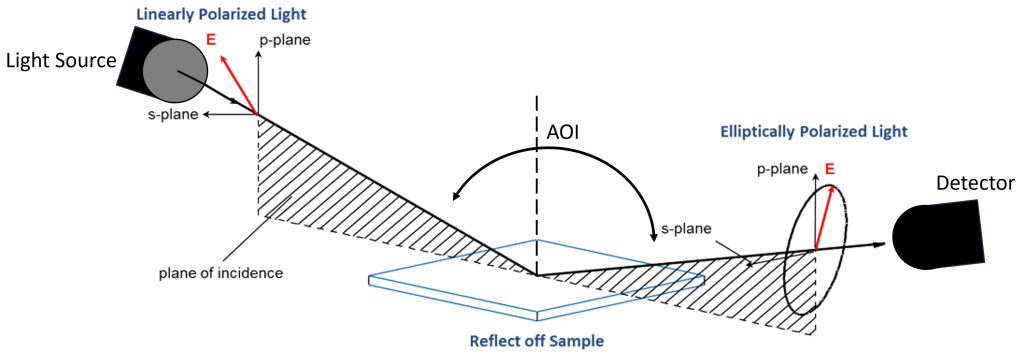


Figure 3.2: A schematic of a spectroscopic ellipsometry measurement showing linearly polarised light reflecting of a sample surface to create elliptically polarised light which is then recorded by a detector. The angle of incidence (AOI) of the measurement is variable multiple scans are typically taken at different AOIs during a measurement at an acquisition time of 10 s each. Adapted from the J.A Woollam website [75].

Ellipsometry measurements in this thesis were performed using a Woolam RC2 Spectroscopic Ellipsometer. Linearly polarised light is shone onto sample surfaces at various angles of incidence (AOI), typically 55°, 60°, 65°, 70°, 75° and 80° (with respect to the sample normal), with an acquisition time of 10s each. The reflected light is elliptically polarised by the thin film sample and is then collected by the detector at the same angle of incidence, and the Ψ and Δ values are recorded as shown in Equation 3.1:

$$\rho = \frac{r_p}{r_s} = \tan(\Psi)e^{i\Delta} \tag{3.1}$$

where ρ is the polarisation of the light, r_p is the p-component of the polarisation, and r_s is the s-component of the polarisation. A schematic of the measurement is shown in Figure 3.2. The polarisation of the light is related to the refractive index n and the extinction coefficient k through the following relation [75]:

$$(n + ik)^2 = \epsilon_a \sin^2 \phi \times \left(1 + \tan^2 \psi \left(\frac{1-\rho}{1+\rho}\right)^2\right) \tag{3.2}$$

where n and k are referred to as the optical constants, ϵ_a is the ambient dielectric function, and ϕ is the angle of incidence.

The spectral range of the measurements is 210 nm to 1600 nm. Transmission measurements were also performed by putting the arms of the ellipsometer into a transmission geometry and collecting the transmitted light after background measurements are taken.

Analysis of the data to determine optical constants is done using CompleteEase, software written by Woollam to control the instrument and analyse the data. Ellipsometry provides an ensemble view of a sample, i.e. the models calculated from the data represent the mean optical environment within the beam footprint. The beam itself is approximates an ellipse with a roughly 0.5 (0.2) mm semi-major (semi-minor) axis, but this changes size slightly as the AOI changes. For smaller samples a focusing probe can be used to narrow down the beam to around 200 μm, although this comes with a reduction in overall intensity of the beam, however, this has not been observed to change the data quality significantly, i.e. data taken with the probes yield similar if not identical results compared to data taken without them.

Samples were deposited on a mix of substrates comprising quartz, glass, Si with a native oxide, and Si with a 150 nm thermal oxide. These substrates were measured

while bare, i.e with no sample film deposited on them, and standard models generated for them before analysing subsequent sample data. When a batch change of new substrates occurred, the new bare substrate was measured and new models generated.

Typically for a given material more than one substrate is used for the measurement, or in the case of transparent substrates the transmission data should at least be taken as well. This practice was followed in this thesis. Typically analysis begins with the data taken in a reflection geometry, i.e. the Ψ and Δ data. First, an optical model, i.e. the optical constants n and k, of the substrate is loaded in (typically a previously fitted Cauchy model for transparent substrates like quartz or glass, and library models for Si substrates), which the sample model will be built on top of. Next, the transparent regime (region where the extinction co-efficient $k = 0$) is determined by looking at the raw data and seeing at what wavelength region absorption features begin to appear. Since most of the materials in this study are semi-absorbing small molecules, i.e. have transparent and absorbing regimes, this is typically > 800 nm. A Cauchy model defined as:

$$n(\lambda) = A + \frac{B}{\lambda^2} + \frac{C}{\lambda^4} \tag{3.3}$$

where A, B, and C are constants. Equation 3.3 is fitted to the data and the thickness of the film is determined, as well as whether there is significant enough roughness to warrant its inclusion in the model. This is determined by seeing if the mean standard error (MSE) of the fit changes significantly or not when roughness is added as a fitting parameter. The MSE is given by the square of the mean residual error, summed over all wavelengths and angles of incidence used in the fit to provide a single number for the goodness of fit to ensure matching between model simulated curves and experimentally measured data. The fitting

of a Cauchy model is shown in Figure 3.3 for the case of molecular thin films of the molecule PDIFCN2 (discussed further in Chapter 4).

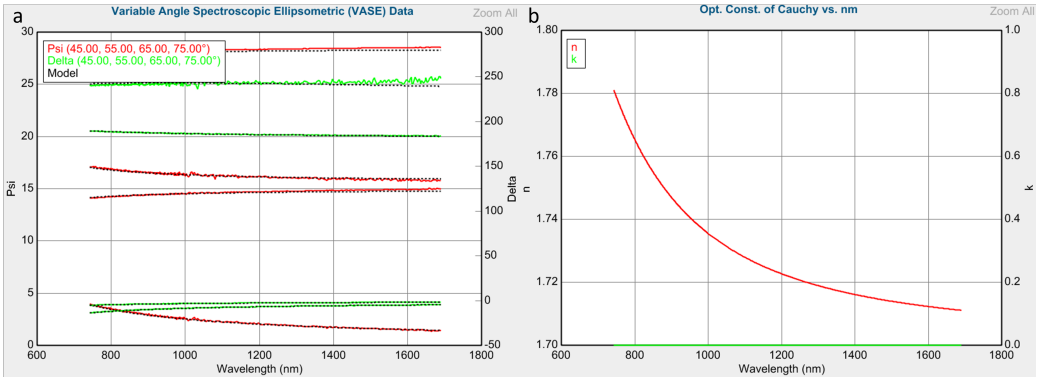


Figure 3.3: A snapshot of the fitting process from the software CompleteEase of a representative thin film sample, in this case a 20 nm (nominal) film of the acceptor molecule PDIFCN2 deposited on a quartz substrate. a) The fit of a Cauchy model to the experimental Ψ and Δ data in the transparent regime, i.e. > 900 nm. The MSE of the fit is 2.6, indicating a good fit to the data, and the Cauchy parameters for the model fit are $A = 1.70$, $B = 0.02$, $C = 0.01$. The surface roughness parameter was not observed to affect the quality of the fit. b) The optical constants n and k associated with the model fit shown in a). Further details of the fit can be found in Appendix A.2.2

The Cauchy layer is converted to a b-spline model which is Kramers-Kronig consistent and the fit is expanded to include the absorbing regime. At this point the fit is typically optimised by adding higher resolution fits for narrow spectral regions where the model has failed to capture sample data accurately. Figure 3.4 shows a representative fit of a b-spline model for the same dataset used in Figure 3.3.

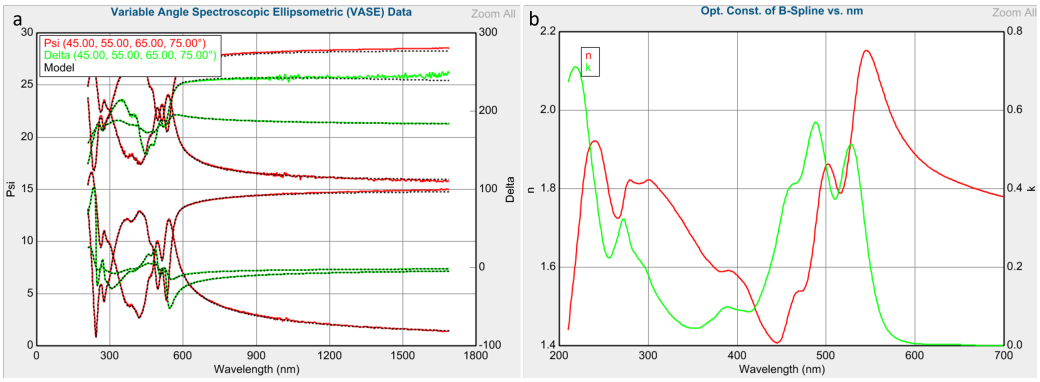


Figure 3.4: A snapshot of the fitting process from the software CompleteEase of a representative 20 nm (nominal) thin film sample, in this case of the acceptor molecule PDIFCN2 deposited on a quartz substrate. a) The fit of a b-spline model to the data. b) The optical constants n and k associated with the model fit shown in a). The MSE of the fit is 2.6, indicating a good fit to the data. For further details of the fit please refer to Appendix A.2.2.

The next step is converting the absorbing layer to an uniaxial anisotropic layer to see if it fits the data better. This creates a b-spline to represent the out of plane components and a separate b-spline to represent the in plane components. At this point additional sample data, if available, are loaded into the analysis using a multi-sample analysis (MSA) approach. This additional data can be reflectivity data of the sample deposited on other substrates or transmission data. The data is loaded in and the model then fits all the data simultaneously. Checks to see if the the individual data is consistent with each other are made by separately fitting the individual data files to see if the models converge on significantly different results. If they do not, then they are used together in an MSA fit. Figure 3.5 shows a representative fit of an anisotropic b-spline model to the same dataset showcased thus far, albeit with additional sample data from different substrates included. The MSE of the fit is less than 2, indicating an excellent fit to the data. At this point the model parameters have been optimised and the resulting optical constants can be easily exported from CompleteEase and used for any further analysis.

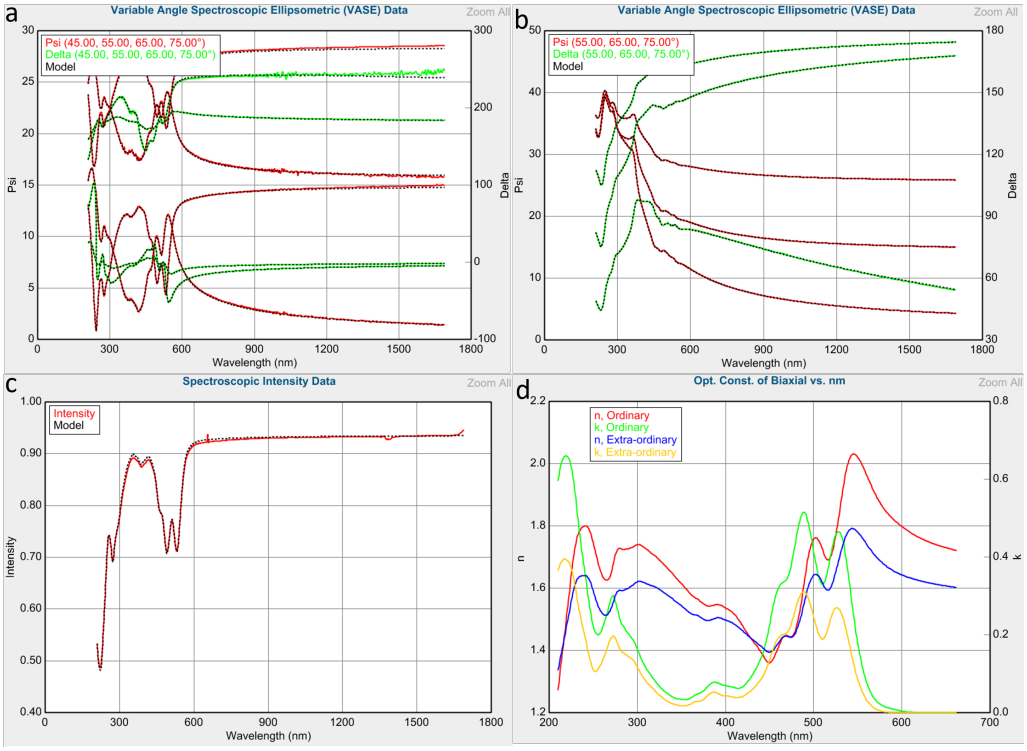


Figure 3.5: A snapshot of the fitting process from the software CompleteEase of representative 20 nm (nominal) thin film samples, in this case of the acceptor molecule PDIFCN2 deposited on quartz and Si (with a native oxide) substrates, showing a multi-sample analysis (MSA) fit of an anisotropic b-spline model to the a) reflectivity data of the film deposited on a quartz substrate, b) reflectivity data of the film deposited on a Si substrate, c) transmission data of the film deposited on a quartz substrate, and d) the anisotropic optical constants associated with the MSA fit (ordinary refers to in-plane components and extra-ordinary refers to out-of-plane constants). The MSE of the fit is less than 2, indicating an excellent fit to the data. For further details of the fit please refer to Appendix A.2.2.

This approach greatly increases the accuracy and the uniqueness of the model fits. Specifically, using Si with thermal oxides and transmission data on transparent substrates is particularly beneficial as it increases sensitivity of anisotropic fits, allowing far more of the data to be tested against the model. Si with thermal oxide creates oscillations in the data that arise from the thick oxide layer in the transparent regime of the data as opposed to relatively featureless curves typical

in transparent substrates, which allows model fits to be tested against data in a wider spectral range. MSE values for MSA models are usually larger for this reason, but the optical models are far more reliable. Transmission data allows the in plane components of the optical model to be independently verified as the out of plane components will not affect the transmission data. Due to the various checks implemented conversion to a general oscillator is not necessary, unless specific oscillator parameters are explicitly needed, which was not the case in this thesis.

Once a reliable model has been developed the ratio of the maximum extinction coefficient in the in-plane direction ($k_{in-plane}$) and the maximum extinction coefficient in the out-of-plane direction ($k_{out-of-plane}$) can be used to estimate the mean tilt angle of the optical transition dipole moment (TDM) with respect to the substrate normal using the following equation [76, 77]:

$$S_\mu = \frac{1}{2}\langle 3\cos\theta^2 - 1\rangle = \frac{k_{out-of-plane} - k_{in-plane}}{k_{out-of-plane} + 2k_{in-plane}} \tag{3.4}$$

where θ is the angle between the molecular TDM and the substrate normal, $\langle ...\rangle$ refers to an ensemble average which is what the ellipsometry measurement probes anyway, and S_μ is the orientation order parameter describing the mean orientation of the TDM with respect to the substrate normal. Given the statistical nature of the idea of a 'mean' orientation in a sample, it is perhaps more correct, and less misleading, to use the order parameter when referring to orientation of a distribution of molecules. $S_\mu = -0.5$ denotes a perfectly parallel to the substrate orientation, $S_\mu = 1$ denotes perpendicular to the substrate, and $S_\mu = 0$ denotes either no preferential orientation, corresponding to an isotropic distribution, or perfectly aligned TDMs oriented at $54.7°$. This is illustrated in Figure 3.6

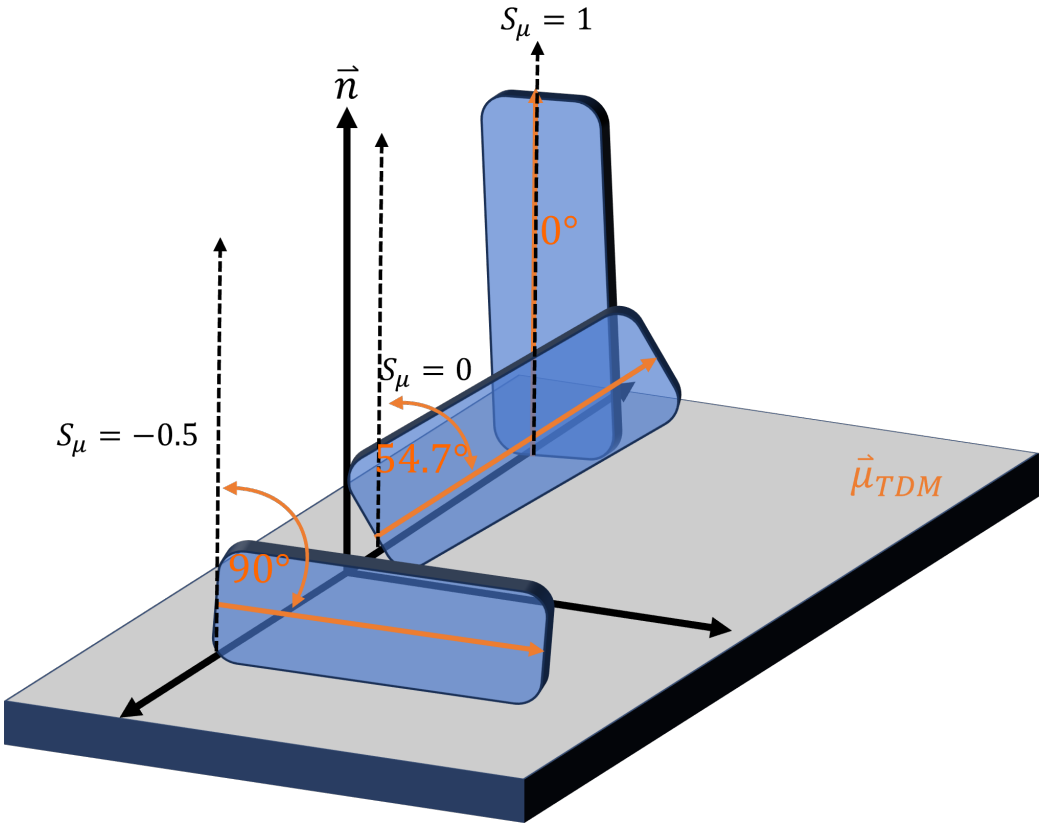


Figure 3.6: Co-ordinate system describing the geometry of different orientation angles (0°, 54.7°, 90°) with respect to the surface normal $\vec{n}$ of a molecule (shown as a blue rectangle), showing the orientation of the optical transition dipole moment $\vec{\mu}_{TDM}$ along the molecular backbone at three different values of the molecular order parameter S_μ.

The absorption onset of the materials is a parameter of interest and is calculated by approximating the long wavelength tail of the extinction coefficient as a straight line and taking the intersection of the this line with the origin. This is an approximation as there is some degree of subjectivity in choosing the appropriate bounds for the linear approximation, and in general one should assume a ≈ 5 nm uncertainty in this approximation.

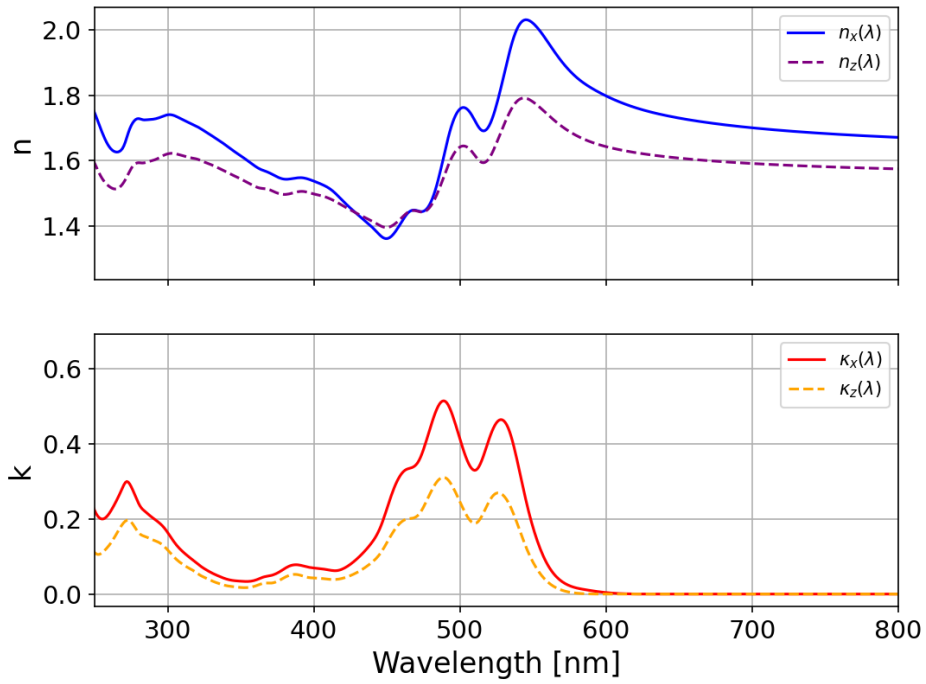


Figure 3.7: Anisotropic optical constants of 20 nm (nominal) films of PDIFCN2, calculated via an optical model based on spectroscopic ellipsometry measurements. Measurements were performed on quartz substrates and silicon wafers with a native oxide, with both data sets used in an multi-sample analysis approach. MSE of the fit is ≈ 1.9. Fitting details can be found in Appendix A.2.2.

Near Edge X-ray Absorption Fine Structure (NEXAFS)

NEXAFS measurements were conducted in a total electron yield (TEY) geometry at beamline B07 at the Diamond Light Source over two separate beamtimes (SI29412-1 and SI30197-1). Figure 3.8 shows a schematic of a typical NEXAFS TEY measurement. In a NEXAFS spectroscopy measurement a sample is illuminated with soft x-rays in vacuum, i.e. photons in the $200 - 1000$ eV range. Figure 3.8 shows a schematic of a NEXAFS measurement. This illumination excites electrons from core atomic orbitals, in particular the K shell of carbon

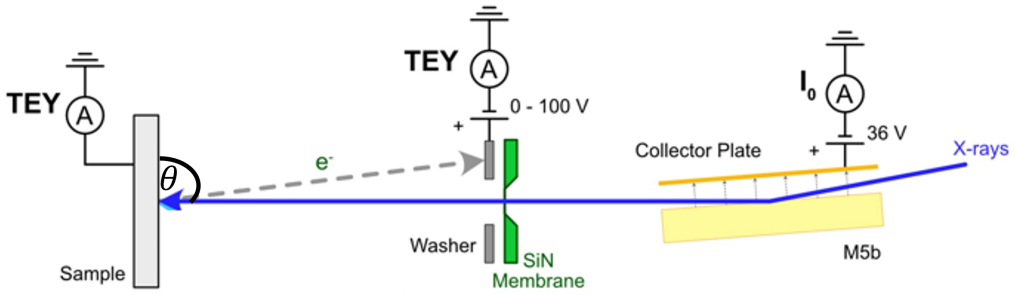


Figure 3.8: Schematic of a total electron yield NEXAFS measurement. A beam of soft X-rays in the $200-1000$ eV range are illuminated on a sample at a variable angle of incidence. Electrons are emitted from the surface of sample and detected by an electrode held a high voltage. Image taken from the DLS B07 website [78].

atoms, and into higher energy molecular orbitals, which subsequently decay and emit free charges. In a TEY geometry these charges are picked up by electrodes and spectra are recorded with distinct resonances at excited state energies. This often reveals the fine energetic structure of molecule, and depending on the energy range scanned the different transitions arising from the various chemical moieties which make up a molecule can be investigated. In this study we focus primarily on the carbon edge, i.e. the $280-330$ eV range to probe different carbon bonds, often the most significant bond in π-conjugated organic molecules. Furthermore, the sample can held at various angles with respect to the incident X-rays to yield angle-resolved information about these transitions, which can often reveal the preferential orientation of the different chemical moieties in the film. It should be noted that the spectra are dependant on electrons being ionised and reaching an electrode to be recorded. Furthermore, around the energy of the NEXAFS carbon edge (≈ 300 eV) the inelastic mean free path of an electron is in the order of units of nanometers. The measurement should thus be considered surface sensitive and the analysis should only be considered reliable for information about the surface of the thin film, with the exact length scale of the surface sensitivity being dependant on the chemical composition of each sample, but is usually < 10 nm.

Analysis and processing of the NEXAFS data is done using the comprehensive NEXAFS fitting software QANT [79]. Figure 3.9 shows a NEXAFS spectrum of a BTIC-H thin film, taken at normal incidence. The data is first divided by the spectrum of the initial beam before entering the sample chamber, which is measured using a separate detector. This data is then subsequently normalised at the pre-edge (< 284 eV) and the post-edge regions (> 330 eV).

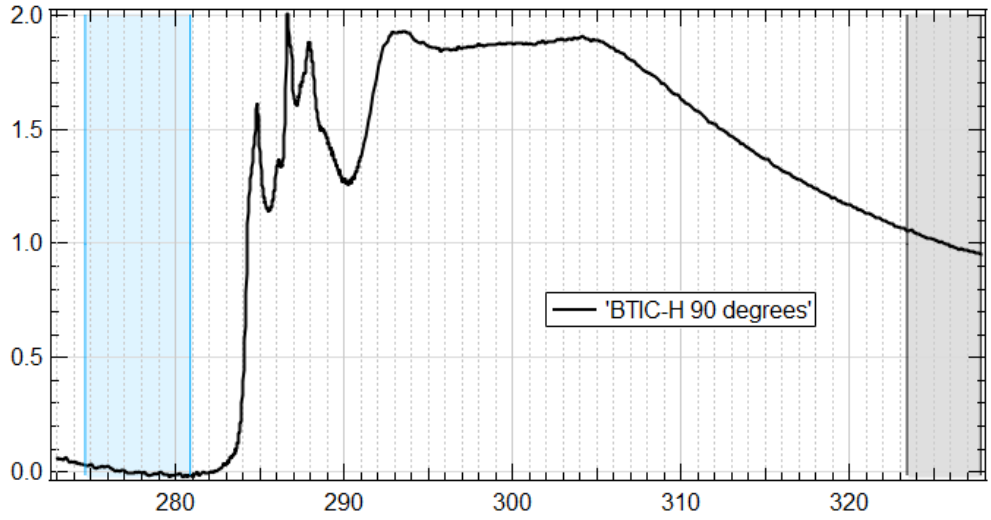


Figure 3.9: A typical processed NEXAFS spectrum showing the pre-edge region area highlighted in blue and the post-edge region highlighted in grey. The data is first divided by the initial beam spectrum and then normalised to the pre-edge region such that the average intensity of the pre-edge region is 0 and the average intensity of the post-edge region is 1. The data shown here is of 70 nm of BTIC-H deposited on an ITO layer on a glass substrate, measured at normal incidence.

Different peaks in the data can be fitted with a series of Gaussian oscillators, each describing an electronic transition from the $1s$ orbital, i,e, the K shell, of a carbon atom. Depending on the energy of transitions, these describe the $1s \rightarrow \pi^*$ or the $1s \rightarrow \sigma^*$ transitions in a molecule. The π^* orbitals in π-conjugated molecules can often be considered a vector orbital and lies perpendicular to the plane of the carbon ring [80], and the fits of these transitions for data taken at several angles can reveal the orientation of the molecule's π^* orbital with respect to the substrate

normal using the following expression [81, 80]:

$$A_{peak}(E) = C(E) \cdot \left(1 + \frac{1}{2}[3\cos\theta^2 - 1][3\cos\alpha(E)^2 - 1]\right) \tag{3.5}$$

where A_{peak} is the resonant peak area, θ is the angle of incidence between the electric field vector of the incidence light and substrate normal, C(E) is a constant equivalent to the peak area for an isotropic distribution, and $\alpha(E)$ is the net orbital tilt measured from the substrate normal, and E is the photon energy. Following the approach used in interpreting the calculated mean orientation angle in the the Spectroscopic Ellipsometry section above, the orbital tilt will similarly be converted into an order parameter S_π.

For elongated, i.e. rod-like, molecules, the order parameter S_π can be used as a proxy for the short molecular axis orientation, i.e. $S_\pi = 1(\alpha = 0°)$ face on orientation and $S_\pi = -0.5(\alpha = 90°)$ edge on orientation, and $S_\pi = 0$ denotes either no preferential orientation, corresponding to an isotropic distribution, or perfectly aligned orbital vectors oriented at $54.7°$. This is illustrated in Figure 3.10.

A comprehensive analysis of NEXAFS spectra usually requires some degree of computational analysis to properly assign resonances to peaks in the observed spectra. In this thesis, however, we have chosen materials such that there is sufficient data in the literature about the functional groups of the molecules that we are investigating to inform our analysis without the need of additional input from computational modelling. For example, C 1s $\rightarrow \pi^*$ $C = C$ resonances (this may be referred to as just $C = C$ or even π^* resonances where this is unambiguous) often appear as a series of Gaussian oscillators in the pre-edge region of a typical NEXAFS spectra. However the first two or three peaks are often the most distinct

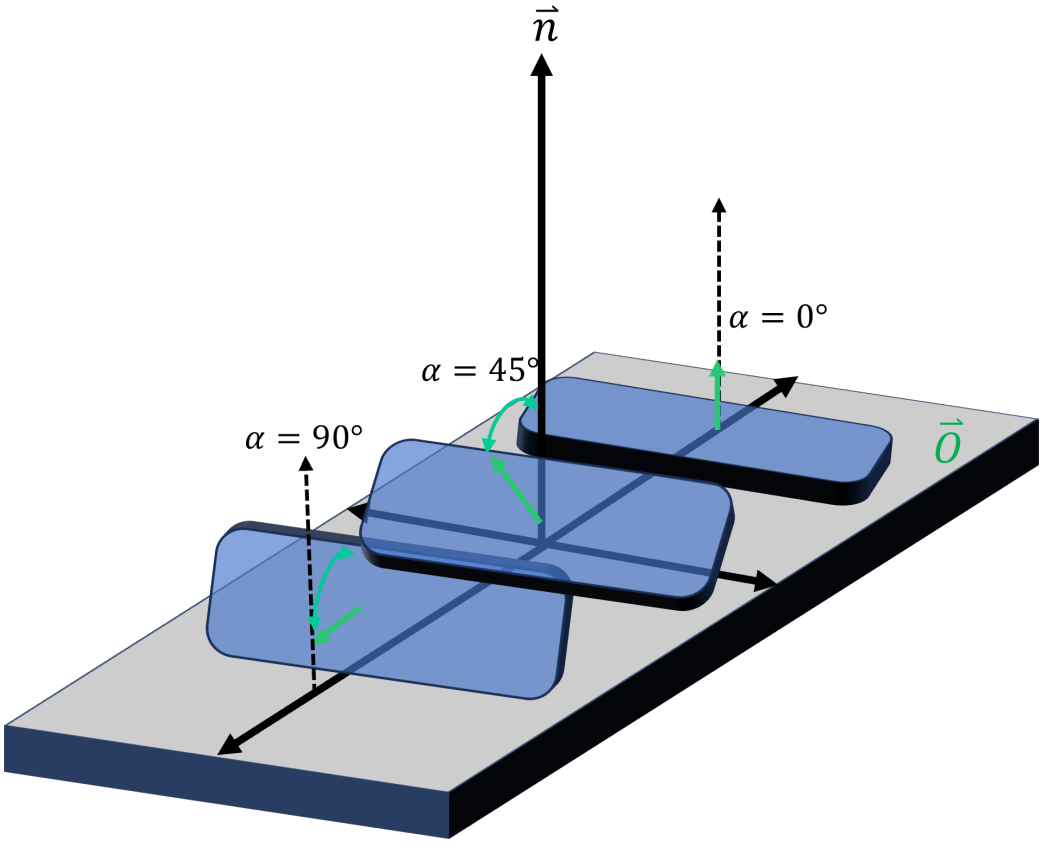


Figure 3.10: An illustration showing how the orbital orientation vector $\vec{O}$, here specifically referring to the π^* orbital, tracks the face-on orientation of an elongated molecular shape.

and unambiguous. Subsequent peaks may be difficult to accurately determine due to contributions from other chemical moieties giving rise to π^* transitions such as $C = O$ or $C - N$ groups, or even other orbital transitions from the more common bonds, for example the σ^* resonances from $C = C$, $C - C$, $C - H$. Within the context of determining orientation angles, this can be overcome somewhat by looking at groups of similar angles calculated from Equations 3.5, which uses the integrated, and cumulative, area under the peaks to determine the orbital tilt. If for example a $C - N$ bond is locked within a rigid conjugated backbone, it is unlikely that the orbital tilt of the π^* orbital will be much different from the surrounding

$C = C$ π^* orbitals.

It should be noted here that the σ^* orbital can similarly be considered a planar orbital and lies in the plane of the backbone of a π-conjugated molecule and fits of these transitions, using a similar expression to Equation 3.5 from ref [80], can reveal the orientation of the σ^* orbital plane with respect to the substrate plane (which is identical to the orientation of the orbital normal to the substrate normal), and would reveal similar information as that from using the π^* transitions, albeit with less certainty as these transitions are inherently noisier given their proximity to the NEXAFS edge and the associated fitting uncertainty comes from this. Consequently, the σ^* transitions will not be used to make conclusions about the samples investigated in this thesis.

Ambient Photoelectron Spectroscopy

Ambient photoelectron spectroscopy (APS) spectra were measured using an Ambient-pressure Photoemission Spectroscopy system (KP Technology, APS02), courtesy of Professor Iain McCulloch from the University of Oxford. IP levels were measured via a UV light (4 eV to 7 eV) illuminating the samples to generate photoemission of electrons. The photoemitted electrons interact with air molecules and generate radicals. These radicals are then collected by a positively biased tip. The HOMO levels were determined by fitting a straight line from the cube root photoemission intensity to the baseline with a Python script written by Joseph Spruce, which has been determined in the literature to be good approximation for the case of semiconductor materials [82]. The analysis follows the process used in [83]. Data shown in this thesis was measured with the assistance of Ming Zhu and Joseph Spruce.

Estimating the Electron Affinity from Optical Data

Direct and accurate measurement of the electron affinity (EA) is not trivial and requires complex set ups such as Inverse Photoelectron Spectroscopy (IPES) or Low-Energy IPES, which are niche tools. Common approaches to estimation of the EA often refer confusingly to the LUMO, and have serious shortcomings. These include:

- only using the optical gap to determine the LUMO (EA), therefore neglecting the binding energy of the exciton,
- using redox potential measurements from cyclic voltammetry (CV) to determine the LUMO, therefore neglecting the environmental impact of thin film formation.

There are corrections that can be applied to these values to make them more physically relevant, and this represents another way to estimate the energy levels in these materials. Instead, in this thesis the EA is estimated using an empirical expression calculated by ref [84] which relates the EA measured by IPES to the optical gap of a series of molecular organic semiconductor compounds. We can then compare this value to that measured in the literature to gain confidence in the value of the LUMO. The established empirical expression is as follows:

$$EA_{estimate} = 1.14 \pm 0.16 \cdot EA_{optical}(eV) + 1.19 \pm 0.52eV \tag{3.6}$$

where $EA_{opt} = HOMO + E_{opt}$ and E_{opt} is the optical gap given by the absorption onset, which itself is calculated by fitting a straight line to the long-wavelength tail of the absorption. Equation 3.6 yields high uncertainty, particularly from the offset term, which highlights the difficulty in accurately determining the electron affinity.

Atomic Force Microscopy

Atomic force microscopy (AFM) was performed in tapping mode over 256 lines using the Asylum Research MFP-3D AFM (Oxford Instruments), with HQ-150-Au model cantilever tips. Analysis of the AFM was performed with the free software Gwyddion [85]. Roughness values were evaluated as root mean squared height of the image area. Scans were done in three separate places on each sample and error was assigned as standard deviation between RMS roughness of scan areas. AFM measurements and image processing in this thesis were performed by Olivia Gough.

Grazing Incidence Wide-Angle X-Ray Scattering

Grazing Incidence Wide Angle X-ray Scattering (GIWAXS) data in this thesis were taken at XMaS: The UK Materials Science Facility (BM28) at the European Synchrotron Radiation Facility (ESRF, experimental session 28-01-1306). A MAR detector was used to acquire data at $8 - 10$ keV.

The principle of the GIWAXS measurement is as follows. A high energy X-ray beam of known energy is prepared using various optics. This is then used to illuminate a sample placed in its path at various angles of incidence. The set up is calibrated such that the beam is cut in half but the surface of the sample, and that the sample lies as parallel to the beam as possible. The high energy photons scatter off the sample material, and if they interfere constructively they are picked up by a 2D detector placed a calibrated distance away from the sample. The signal-to-noise ratio will be maximised when the incoming light penetrates the sample material but reflects off the substrate, thus limiting the scattering from the substrate and thereby reducing noise. This often only occurs at close to parallel angles of incidence, thus the term grazing incidence, and leaving a narrow range

of angle of incidence for which this can occur. For this reason various scans are taken within a narrow range and then reviewed after the measurement, with the highest signal-to-noise scan identified as the image of choice. The resulting data produces a scattering pattern which can then be analysed to better understand the microstructure of the material, in particular the crystallinity of the material. The atomic and molecular planes of the material diffract incident light, and the angle of diffraction relates to the spacing between the planes. The direction of the diffraction relates to the orientation of the planes. The magnitude of the scattering vector q is given by:

$$q = \frac{4\pi}{\lambda} \sin\theta \tag{3.7}$$

where λ is the wavelength of the incident light, and θ is the scattering angle. In the 2D images generated by the detector scattering along the q_z indicates crystalline order in the direction perpendicular to the substrate, and therefore from stacking planes parallel to the substrate, and vice versa for the q_{xy} direction.

3.1.3 Device Measurements

Current-Voltage measurements

Current density-voltage ($J-V$) characteristics were measured under illumination from a Newport Oriel Sol3A solar simulator with a Xe arc lamp. JV measurements are essential to understand the electrical behaviour of solar cells, and key device parameters such as the fill factor (FF), the V_{OC} , the J_{SC} , and the power conversion efficiency (PCE) can be determined from the JV curves.

The principle of $J-V$ measurements is to perform a voltage sweep on a device and to measure the current response from the device. This is done while the devices are either illuminated with a lamp source which simulates the AM1.5G solar spectrum, or in the dark. The dark measurements are achieved by covering

the devices in aluminium foil.

External Quantum Efficiency

Sensitive external quantum efficiency measurements were performed on a custom-built set up, built by Anna Jungbluth. The set up consists of a monochromator, preamplifier, and lock-in amplifier, as well as spectral filter to increase the sensitivity of the measurement. The principle of the measurement is that a beam of light of known wavelength and photon flux is illuminated onto a device and the current generated is measured. The light is scanned through a wavelength range to generate a data set of the charges extracted as a function of wavelength of light incident onto the device, i.e. external quantum efficiency.

Calculation of Voltage Losses

Analysing the voltage losses in photovoltaic devices is a good way to assess the energy loss mechanisms in a device. In general, a voltage loss analysis looks at the difference between the V_{OC} and a reference energy E_{ref} and ascribes this difference to specific contributors. In this thesis the detailed balance method is used to decompose the voltage losses in devices [86, 87], which uses thermodynamic principles and is applicable to both inorganic and organic devices. Following the guidance from refs [87] and [88] we will use the inflection point of the external quantum efficiency spectra, which is commonly reported in the literature, as a common reference point E_{ref}. This makes it a good comparator to use when comparing results with the literature. Errors arising from uncertainty in the inflection point are in the order of 10 meV [87].

According the detailed balance picture voltage losses are split as follows:

$$\begin{aligned}\Delta V &= E_{ref}/q - V_{OC} \\ &= (E_{ref}/q - V_{OC}^{SQ}) + (V_{OC}^{SQ} - V_{OC}^{J_{SC}}) + (V_{OC}^{J_{SC}} - V_{OC}^{rad}) + (V_{OC}^{rad} - V_{OC}) \\ &= \Delta V_{OC}^{SQ} + \Delta V_{OC}^{J_{SC}} + \Delta V_{OC}^{rad} + \Delta V_{OC}^{nr}\end{aligned} \tag{3.8}$$

where ΔV_{OC}^{SQ} describes the losses compared the Shockley-Queisser limit, $\Delta V_{OC}^{J_{SC}}$ refers to the losses due to an imperfect J_{SC} , ΔV_{OC}^{rad} describes the radiative losses and finally ΔV_{OC}^{nr} refers to the non-radiative losses. We unpack these terms below.

ΔV_{OC}^{SQ} is defined as the difference between the maximum possible V_{OC} in the Shockley-Queisser limit [89], with using E_ref as the photovoltaic bandgap. Even in ideal solar cells this term would have a non-zero value, given the unavoidable radiative recombination that is present in solar cells as a result of detailed balance, such that the recombination rate is equivalent to the recombination rate. This loss is roughly proportional to E_{ref} and is usually between $250 - 300$ meV for organic solar cells [87].

$\Delta V_{OC}^{J_{SC}}$ arises from differences in the measured J_{SC} compared to the J_{SC} in the Shockley-Queisser limit, and is given by:

$$\Delta V_{OC}^{J_{SC}} = \frac{k_B T}{q} \ln \frac{J_{SC}^{SQ}}{J_{SC}} \tag{3.9}$$

As a consequence of the logarithm the voltage losses resulting from this term are comparably low, for example for a 20% and 50% decrease in measured J_{SC} the resulting $\Delta V_{OC}^{J_{SC}}$ would be 5.6 and 17.5 meV respectively, with the former being similar to what state-of-the-art OSCs currently exhibit [45]. Losses in the photocurrent can arise from incomplete absorption or corresponding losses in the

charge collection in a device. The former results in gradual absorption onsets (as opposed to step-functions in the absorption like assumed in the Shockley-Quiesser limit) and an external quantum efficiency below unity.

ΔV_{OC}^{rad} arises from additional radiative losses that are not taken into account by ΔV_{OC}^{SQ}. In organic solar cells these are manifest as a result of the difference between the energy of the charge transfer state and that of the singlet state, which leads to gradual absorption tail in the EQE spectra. The magnitude of this loss can vary between 10s of meV and 100s of meV [90] and is dependant on the material properties of the absorbing material, i.e. donor and acceptor, as well as their resulting interaction. V_{OC}^{rad} can be calculated by first calculating the radiative saturation current density (J_0^{rad}) and the short-circuit current density J_{SC} from the EQE:

$$J_0^{rad} = q \int_0^{\infty} EQE \cdot \phi_{BB} dE \tag{3.10}$$

$$J_{SC} = q \int_0^{\infty} EQE \cdot \phi_{AM1.5G} dE \tag{3.11}$$

where π_{BB} is the black-body spectrum and $\phi_{AM1.5G}$ is the AM 1.5G solar spectrum at 100 W cm^{-2}. V_{OC}^{rad} can then be calculated via:

$$V_{OC}^{rad} = \frac{k_B T}{q} \ln \frac{J_{SC}}{J_0^{rad}} \tag{3.12}$$

It should be noted here that the boundaries of the integral are often in practice limited by the experimental range and noise floor of the measurement set up. However, a suitable workaround that has been demonstrated in the literature [88, 87] is to fit the EQE tail with Gaussians and extrapolate the data past the noise floor, which can allow an estimate for the bounds at which V_{OC}^{rad} saturates.

Lastly, ΔV_{OC}^{nr} arises from the remaining losses in devices, and the term 'non-

radiative' is a bit of a catch-all. This is usually in the order of $200 - 500$ meV for organic solar cells [8]. The exact mechanism for non-radiative losses is an active area of debate, but is usually attributed to high-energy phonons and the resulting vibration-mediated losses. Many findings have suggested that these losses are described by the energy-gap law which suggests that larger differences between the charge transfer state energy and the singlet state energies would result in higher non-radiative losses (and correspondingly higher ΔV_{OC}^{nr}). This has been shown to be the case for fullerene OSCs [91], but results from NFA OSC studies suggest that this does not hold true for these devices [92]. This claim has been further contested by findings that improper measurement of energy levels could lead to misleading conclusions about the applicability of the energy-gap law to NFAs [93].

Open Circuit Corrected Charge Carrier Extraction

Open-circuit corrected charge carrier extraction (OTRACE) was performed with a PAIOS system from Fluxim AG, Switzerland. The 60nm thick BHJ samples were illuminated with a white LED light for 100 μs until a steady-state V_{OC} was reached. Delay times were varied between a few μs and 1 ms. The linear voltage pulse (ramp rate of 200 and 400 V/ms) was chosen long enough ($\approx$ 30 μs) such that all mobile carriers were extracted, and the current peak decayed to the displacement current obtained from a dark measurement with no offset voltage applied. The analysis follows reference [94]. OTRACE measurements were performed by Pascal Kaienburg.

3.2 Materials

3.2.1 Overview of Materials

Several NFA molecules are investigated in Chapter 4. These include BTIC-H, TTR, TTIC4F, and PDIFCN2, with BTIC-H also featuring in Chapter 5. These molecules are depicted in Figure 3.11. Apart from these NFA materials, other molecules used include DCV5T-Me, SubNc, HB194, and DTDCPB as the donor materials in devices investigated in Chapter 4 and 5. Fullerene (C_{60}) was also used in some devices in Chapter 5. Molecular structures of these materials are shown in Figure 3.12. Additionally molybdenum oxide (MoO_3) is used as a hole transport layer, and BPhen as an electron transport layer in devices made in this thesis. Aluminium is used as an electrode material, and ITO (which is bought pre-deposited on glass substrates either patterned for device evaporations or un-patterned for thin film characterisation) as a transparent electrode material. C_{60} is also used as an acceptor material in some devices in Chapter 5. Materials used in Chapter 7 include α-sexithiophene (α6T), DTDCPB, and HB194. Unless otherwise indicated, stock of material was purchased from Luminescence Technology Corp, with the exception of C_{60} which was purchased from CreaPhys GmbH (now M. Braun Inertgas-Systeme GmbH).

More details on the NFA and donor materials used in Chapter 4 and 5 and the primary materials investigated in Chapter 6 are given below.

3.2.2 BTIC-H

2,2'-((2Z,2'Z)-((3,3'-dihexyl-[2,2'-bithiophene]-5,5'-diyl) bis(methaneylylidene)) bis(3-oxo-2,3-dihydro-1H-indene-2,1-diylidene))dimalononitrile, called BTIC-H, is a novel acceptor material supplied for this study. The material was synthesized

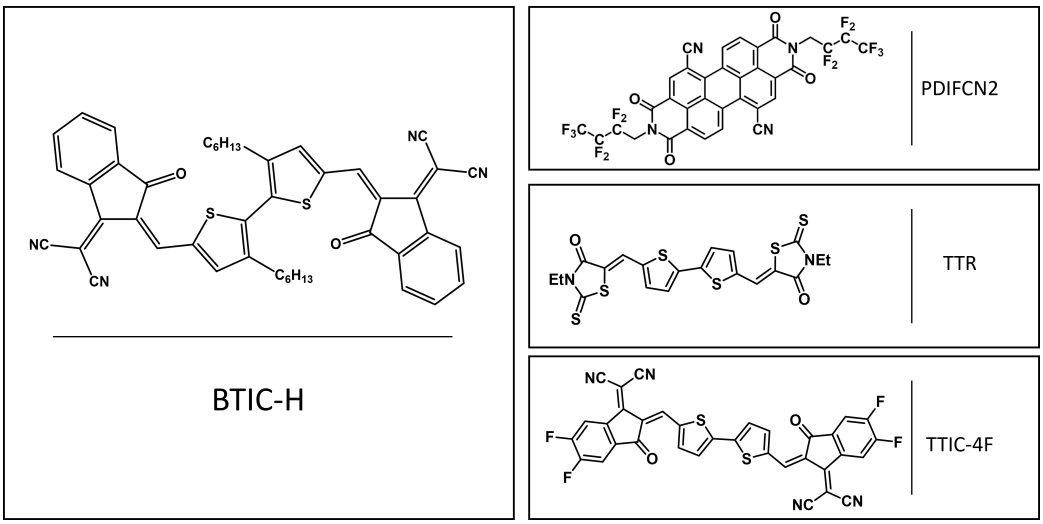


Figure 3.11: Molecular structures of the non-fullerene acceptors investigated in this thesis, namely BTIC-H, PDIFCN2, TTR, and TTIC-4F. The short names of the molecules are given below or next to the structures.

Dongdong Xia from the group of Professor Weiwei Li from the Beijing University of Chemical Technology. The material was supplied in three different batches throughout the study. Batch to batch variations do exist, most notably in the texture and colour of the material powder, but evaporated films look identical and the optical constants of the materials were measured and compared, yielding only minor differences.

BTIC-H was first synthesized by Professor Li's group and characterised in solution and in spin coated thin films. It consists of a bithiophene (BT) core with alkyl side chains substituted on the 3 and 3' positions of the BT units. The energy levels were further tuned by adding electron withdrawing 1,1-dicyanomethylene-3-indanone (DCMI) end groups. The material was also tested in a solution processed organic solar cell using the high performance polymer donor Poly[(2,6-(4,8-bis(5-(2-ethylhexyl)thiophen-2-yl)-benzo[1,2-b:4,5-b']dithiophene))-alt-(5,5-(1',3'-di-2-thienyl-5',7'-bis(2-ethylhexyl)benzo[1',2'-c:4',5'-c']dithiophene-4,8-dione)], called commonly referred to as PCE12 or PBDB-T [74]. Optimised BHJ (spin-coated)

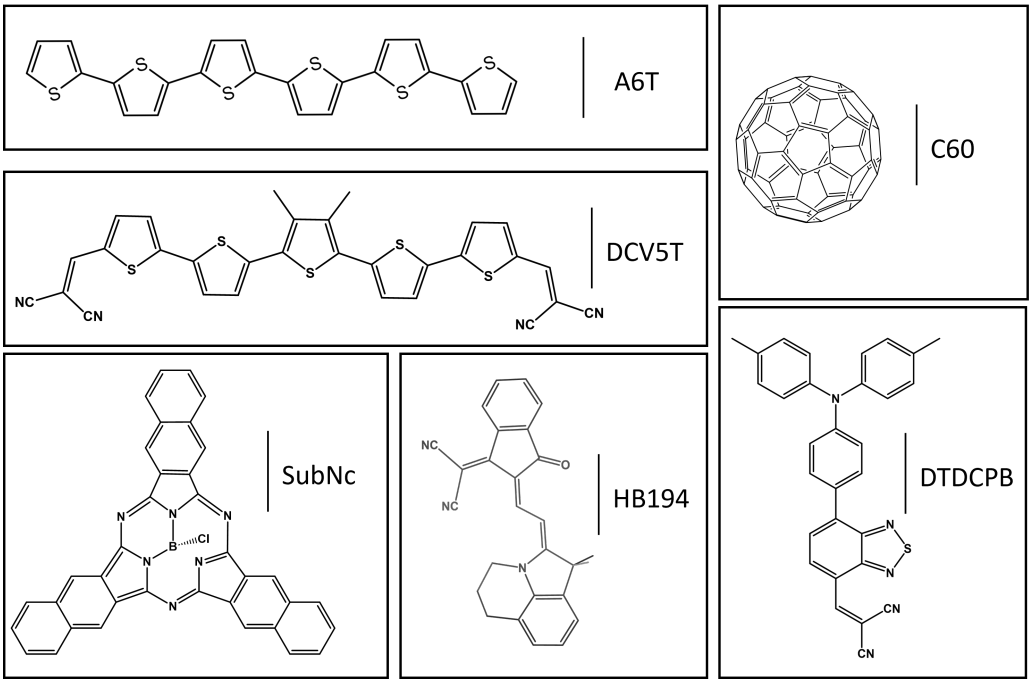


Figure 3.12: Molecular structures of the donor molecules and fullerene investigated in this thesis. The short names of the molecules are given below the structures.

devices made using BTIC-H as acceptor and PCE12 as donor yield J_{SC} of 2.68 mA/cm^2, V_{OC} of 0.69 V, FF of 0.52, and overall PCE of 0.96%. Density functional theory calculations show that the molecules are expected to show a twist along the backbone, yielding a $47°$ angle between the thiophenes. The absorption was measured via UV-Vis, yielding an absorption onset at around 650 nm and a peak at 520 nm. When measured in thin film, a significant red-shift is observed with an absorption onset closer to 870 nm and a peak at 628 nm, with the appearance of a shoulder peak at 706 nm. This red-shift is attributed to the aforementioned twist in the backbone of the molecule being present in solution but not in thin film [74].

Energetics of the molecule were investigated with cyclic voltammetry, with HOMO and LUMO values given as -6.00 and -3.85 eV, respectively. This places BTIC-H in a good position as an acceptor in the energetic landscape of small molecules, it would have a favourable energetic offset with many donor molecules.

3.2.3 TTR and TTIC4F

Stock of TTR and TTIC4F were provided by Professor Iain McCulloch from the University of Oxford and were synthesised by Hu Chen from the King Abdullah University of Science and Technology (KAUST). The molecules were derived from the small molecule acceptor T2-ORH [72]. The molecule comprises a BT core with alkyl-substituted rhodanine (RH) ends. The octyl side chains were attached to rhodanine in a direction parallel to the backbone, which was postulated to improve molecular packing and charge transport [95]. T2-ORH was used in solution processed polymer devices with favourable results. Optimised devices using PTB7-Th as polymer donor gave J_{SC} of 14.29 mA/cm^2, V_{OC} of 1.07 V, FF of 0.59, and overall PCE of 9.02 %. T-T-R keeps the same structure as T2-ORH but shortens the alkyl substitution on the RH end groups from octyl (C_8H_{17}) to ethyl (C_2H_5), shortening the overall structure and making it more suitable to the VTE process. TTIC4F retains the same structure as T2-ORH but gets rid of the side chains entirely by adding fluorinated DCMI end groups the BT core instead.

3.2.4 Perylene Diimides

Perylene diimide (PDI) dyes were some of the first functional non-fullerene acceptors used in OPV [8], and the first published PHJ OSC used a perylene based acceptor [7]. This class of material typically exhibit many favourable properties for an acceptor material; high electron mobility from intermolecular π stacking, electron affinities comparable to fullerene acceptors, strong absorption in the vis-

ible regime, deep lying HOMOs, and good thermal and oxidative stability [96]. However, PCEs in BHJs using PDIs as acceptors can suffer from poor performance, likely due to the lack of percolation pathways formed in the blend as a result of large crystalline domains of the PDIs [97]. These 1D π stacked domains have also been shown to rapidly deactivate excitons [98]. More complex PDI structures were designed to inhibit this crystallisation such as by linking non-coplanar cores, however this offered only slight improvements in performance (PCEs of $\approx 9\%$ were reached) [96].

2,9-Bis(2,2,3,3,4,4,4-heptafluorobutyl)-1,3,8,10-tetraoxo-1,2,3,8,9,10-hexahydro-anthra[2,1,9-def:6,5,10-d'e'f']diisoquinoline-5,12-Dicarbonitrile (PDIFCN2) is a perylene diimide (PDI) derivative that was first synthesised in [99]. It was investigated for use in a PHJ OSC with DPP as donor molecule [100] and showed very low EQE of $< 5\%$, low V_{OC} of ≈ 0.15 V and low J_{SC} of ≈ 0.2 mA/cm^2. The optical constants were measured and reported in [101], showing a peak absorption at ≈ 539 nm. Analysis of the in plane and out of plane components of the dielectric function reveal that the film is mostly disordered with some weak in plane preferred orientation.

Stock of PDIFCN2 was provided by Professor Yonggang Zhen at the Beijing University of Chemical Technology.

3.2.5 α-sexithiophene

α-sexithiophene (α6T) is a conjugated polythiophene molecule consisting of six thiophene rings connected in series attached with $C-C$ bonds. It is a well studied small molecule whose microstructure is well documented in the literature [102, 20, 83]. In particular, the molecule is thought to exhibit a rod-like morphology with a fairly upright orientation when deposited at room temperature, and this

orientation angle is only increased with respect to the substrate plane when the substrates is heated during deposition [102].

α6T has also been used in OSC devices, notably in reference [69] where it was combined with donor materials SubNc and boron subphthalocyanine chloride (SubPc) in triple PHJ device (as opposed to the more standard two layer PHJ device) which showcased a PCE of 8.4%. Reference [83] exploited the orientation changes in the material at different substrate temperatures to create a single-component device which showcased efficient charge generation, highlighting the significant effect the orientation of molecules can have on the energetic landscape in a thin film.

3.2.6 HB194

2-2-[2-(1,1-Dimethyl-5,6-dihydro-1H,4H-pyrrolo[3,2,1-ij]quinolin-2-ylidene)- ethylidene]-3-oxo-indan-1-ylidene-malononitrile (HB194) is a merocynanine dye consisting of a 2-(3-oxo-indan-1-ylidene)-malononitrile acceptor unit connected to an indolenine donor with an alkyl chain. The indolenine donor is bridged with a propylene unit to increase the planarity of this component of the molecule. Effectively the molecule consists of two planar components connected via a flexible chain. The optical transition dipole of the molecule has been shown to lie along the long axis of the molecule [103] and in solution has been shown to form a diimer with a $25°$ separation between molecular planes [104] and in single crystal has been shown to adopt a J-aggregate like packing with the donor units overlapping, but with the acceptor units being rotated $88°$ with respect to each other [105]. While this level of order from a single crystal as well as that from a solution would be unlikely to manifest in a standard vacuum deposited thin film, both these respective conformations are nevertheless important to understand the packing behaviour of HB194.

HB194 has also been used as a donor in vacuum deposited OSCs with both C_{60} and C_{70}, with optimised BHJ devices showcasing PCEs of $\approx 6\%$ [106].

3.2.7 DTDCPB

2-[7-(4-N,N-ditolylaminophenylen-1-yl)-2,1,3-benzothiadiazol-4-yl]methylenemalononitrile (DTDCPB) consists of an electron-donating tri-p-tolylamine moiety connected to an electron-withdrawing dicyanovinylene moiety through another electron-accepting 2,1,3-benzothiadiazole unit. Single crystal X-ray diffraction measurements show that DTDCPB is completely planar due to a dihedral angle of $24.7°$ between the phenyl rings at the end of the molecule and the benzothiadiazole unit at the centre of the molecule. The molecules were also shown to pack in an anti-parallel manner [107]. Optical constants calculated via spectroscopic ellipsometry show slight uniaxial anisotropy in the thin film, and with the transition dipole moment of the lowest energy excited state being along the molecular backbone the claim made is that the preferential orientation of the molecules is parallel to the surface [107].

DTDCPB has also been used as a donor in vacuum deposited OSCs with with both C_{60} and C_{70}, with optimised BHJ devices showcasing PCEs of $\approx 7\%$ [107].

3.2.8 SubNc

Boron subnaphthalocyanine (SubNc) is a subpthalocyanine derivative used primarily as a donor molecule in vacuum deposited OSC devices [108]. However, it has also seen use as an acceptor in the aforementioned triple planar junction cell showing excellent PCEs of 8.4% [69]. SubNc showcases excellent absorption with extinction coefficient > 1.2 beyond 700 nm. SubNc also shows very high exciton diffusion lengths of > 20 nm [109].

3.2.9 DCV5T-Me

2,2'-[3",4"-dimethyl-2,2':5',2":5",2"':5"',2""-quinquethien-5,5""-diylbis(methane-1-yl-1-ylidine)]dimalononitrile (DCV5T-Me), referred to as DCV5T in this thesis, is a dicyanovinyl (DCV) capped A-D-A quienquethiophene [110] that has been used as a donor in vacuum deposited OSCs with optimised BHJ devices with fullerene showcasing PCEs $\approx 7\%$. DCV5T exhibits broad absorption centred around 610 nm, and energy levels have been measured via cyclic voltammetry to be -5.7 and -3.8 for the HOMO and LUMO respectively [110]. Stock of DCV5T was purchased from Synthon Chemicals.

4 | Identifying Evaporable Small Molecule Non-Fullerene Acceptors

4.1 Introduction

The non-fullerene acceptors investigated in this thesis have already been introduced in Chapter 3, and for ease of reference their molecular structures are shown again in Figure 4.1. This chapter will detail the material characterisation of these molecules, in particular the thin film properties as these are most relevant to device applications. Of the materials investigated, BTIC-H was by far the most promising candidate for an evaporable non-fullerene acceptor. These materials were sourced through collaborations with other research groups (see Chapter 3 for details). The different materials investigated in this chapter have varying degrees of depth of characterisation. In particular, the characterisation of BTIC-H was far more extensive than the other molecules investigated. This was due to the fact that the results from preliminary measurements were promising. The materials were all used as received without further sublimation as the potential material losses from sublimation was deemed too high to risk.

It is perhaps useful to explicitly define here what is meant by an evaporable small molecule non-fullerene acceptor. In general, this refers to a molecule that will meet the following criteria:

- it must evaporate well in vacuum, i.e. it should sublime at a temperature below its degradation temperature,
- it should form a relatively homogenous thin film,
- it should show sufficient absorption to contribute to the photogeneration in

a device,

- its energy levels should be low-lying enough to allow for charge dissociation when combined with a donor molecule
- efficient charge generation should be observable in a device,

In particular spectroscopic ellipsometry (SE) and ambient phototelectron spectroscopy (APS) measurements were performed on all samples that were successfully evaporated. SE was used to characterise the optical constants of the materials using an optical model that provides information about the absorption and homogeniety of the thin films. APS measurements yielded the values of the highest occupied molecular orbital (HOMO) levels of the thin films, which are a necessary requirement to choosing a suitable donor material to pair the acceptor with in a device. Recent studies also suggest that the difference in energies of the HOMO levels in NFA OSCs are what drives efficient charge generation in devices [93]. Additional measurements such as atomic force microscopy (AFM), differential scanning calorimetry (DSC), thermogravimetric analysis (TGA), to name a few, were also performed to provide further information about the materials where relevant.

It should be noted that the criteria listed earlier are meant to guide the discovery process rather than provide a strict rule-set by which molecules should be disqualified, hence the minor ambiguity in some of the items. For example, what level of charge generation is efficient? What is sufficient absorption? How far below its degradation temperature should the molecules sublimation temperature be? How low-lying should the energy levels be? These are open questions that this chapter aims to unpack.

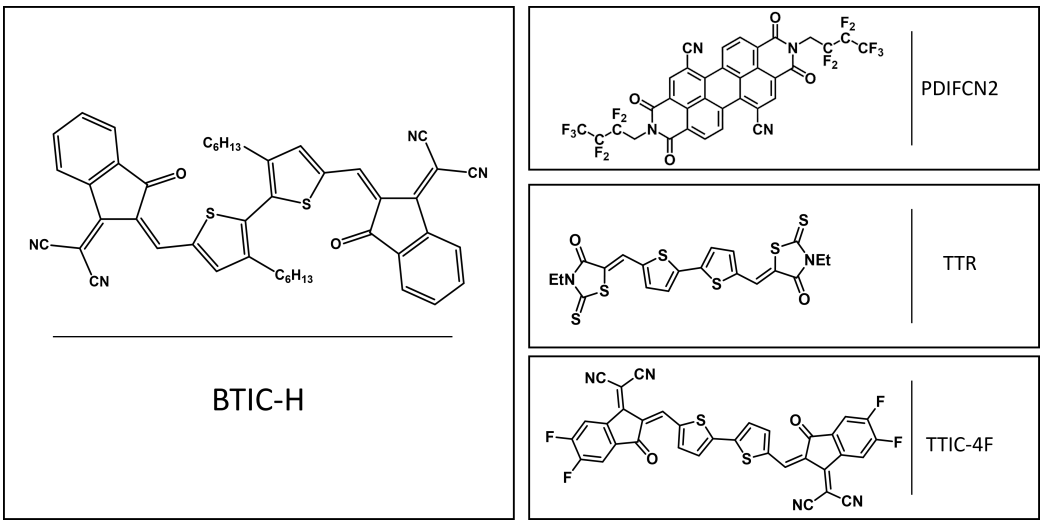


Figure 4.1: Molecular structures of the non-fullerene acceptors investigated in this thesis, namely BTIC-H, PDIFCN2, TTR, and TTIC-4F. The short names of the molecules are given below the structures.

4.2 Evaporability of Candidate NFAs

4.2.1 BTIC-H

BTIC-H presents as a dark green powder with large particulates as seen in Figure 4.2, although depending on the synthesis it can present slightly differently. Batch to batch variations were observed in the powder samples received from collaborators, varying from finer powder samples initially to more fibrous samples towards the latest batch, however the NMR spectra (shown in Appendix A.1) showed only trace amounts of solvent in the powder, which would be eliminated during the thermal evaporation process. Indeed, thin films all presented as deep blue films, and showcased identical spectral shapes in the optical constants, discussed later in this chapter, with any differences observed most likely due to variations in the evaporation rates.

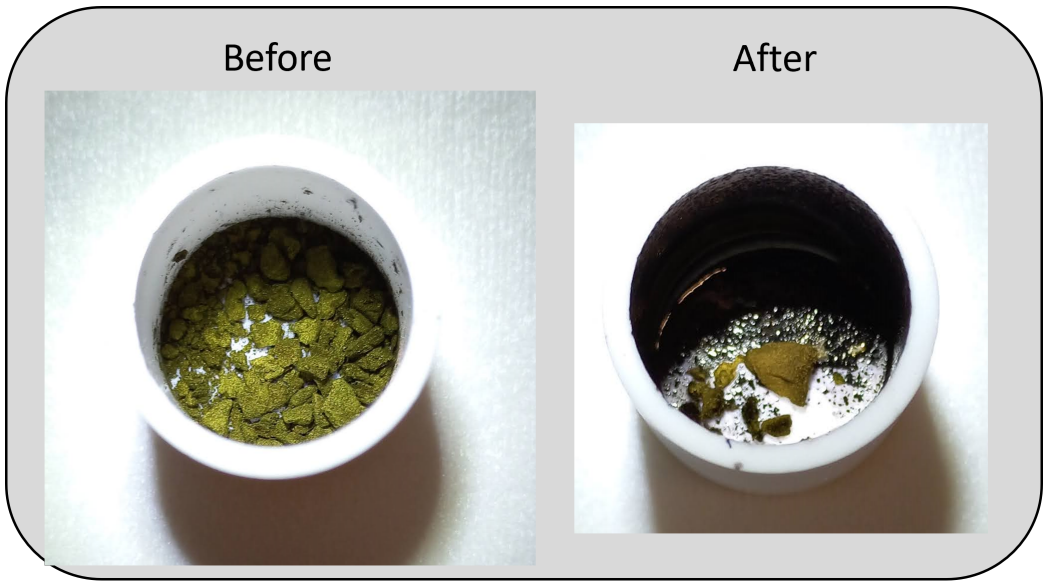
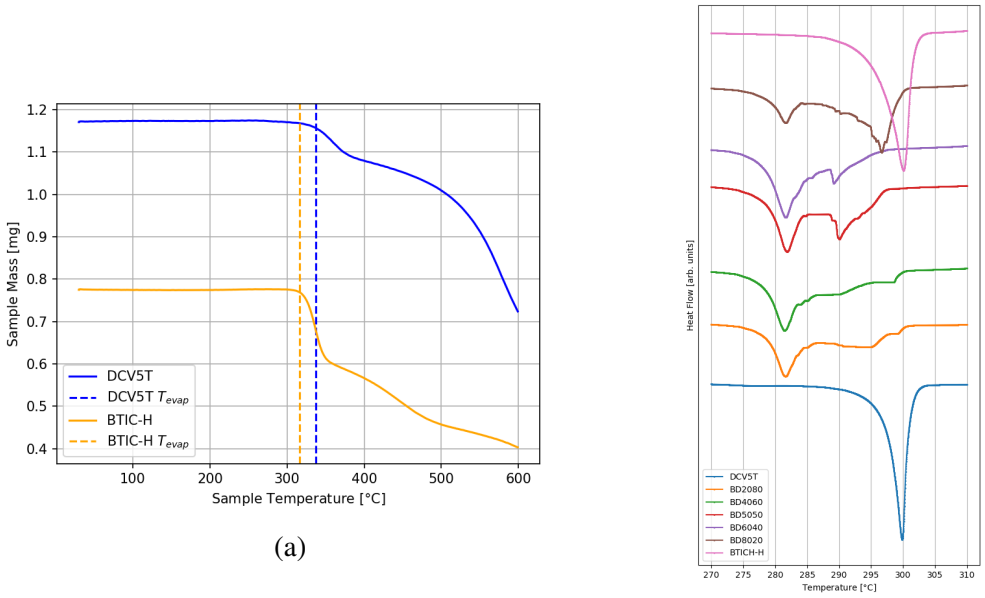


Figure 4.2: Images of BTIC-H material in crucibles before and after being evaporated. Before evaporation, BTIC-H appears to be a green powder with some agglomeration. After evaporation some larger agglomerates are still present and slightly darker, but there is also a distinct residue left in the crucible.

BTIC-H evaporates at a rate of 0.1 Å/s at approximately 210°C. The evaporation needs to be kept under 0.1 Å/s to reduce rapid fluctuations in the rate, and longer evaporations for thicker films did showcase fluctuations up to ≈ 0.4 Å/s that were controlled by reducing the temperature of the crucible during the evaporation. This behaviour suggests that the material melts in the crucible during evaporation, possibly causing evaporation rate fluctuations as critical sample masses undergo phase changes, and this hypothesis is supported by the melt-like residue left in the crucible, as seen in Figure 4.2. Similar evaporation behaviour has been found with the small molecule donor DCV5T, synthesis shown in ref [110]. Figure 4.3 shows the thermogravimetric analysis (TGA) and differential scanning calorimetry (DSC) scans of the material of both DCV5T and BTIC-H. This data was supplied by Prof Weiwei Li. Both materials exhibit very similar thermal behaviour. DSC scans show an endotherm just below 300°C for both materials, and TGA

scans show that between 300°C and 350°C the materials begin subliming. Given that in vacuum materials will undergo phase changes at lower temperatures (as per the ideal gas law $pV = nRT$ where p, V, and T are the pressure, volume, and temperature respectively, n is the amount of substance and R is the gas constant), it is likely that during evaporation the material begins subliming and melting within a very narrow temperature range thereby causing the observed rate fluctuations. DCV5T has been used in the literature to make state-of-the-art evaporated organic solar cells [111], and while the yield of the evaporation is lower than other more standard molecules (closer to 1 mg : 2 nm rather than the more standard 1 mg : 1 nm), the similar behaviour evaporation behaviour of BTIC-H suggests that the molecule is still a viable material candidate for evaporable non-fullerene acceptors.



(a)

(b)

Figure 4.3: a) TGA scans of BTIC-H (orange) and DCV5T (blue) with likely sublimation temperatures indicated (dashed lines), measured in nitrogen at atmospheric pressure. b) DSC thermograms of BTIC-H and DCV5T with endothermic peaks shown as negative. Data was provided by Prof Weiwei Li from the Beijing National Laboratory of Molecular Sciences.

4.2.2 PDIFCN2

PDIFCN2 presents as red powder and evaporates at approximately 205°C at a rate of 0.1 Å/s. The evaporation rate is steady, and leaves little to no residue in the crucible. The material can safely be re-evaporated under similar conditions, which results in less material loss during sample fabrication and is thus favourable. Figure 4.4 shows an image of the material in a crucible before and after the evaporation.

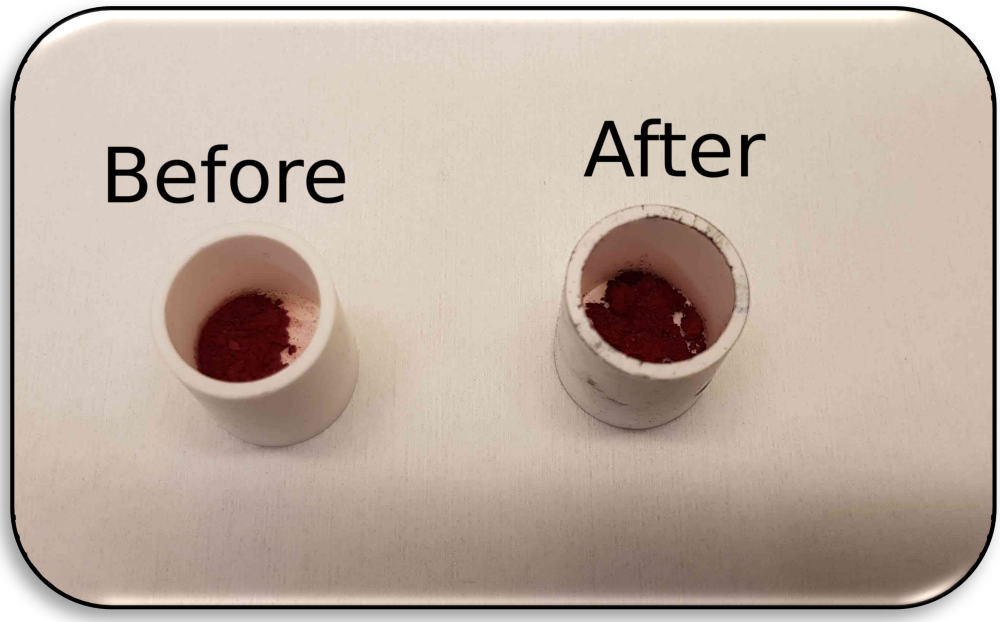


Figure 4.4: Images of PDIFCN2 material in crucibles before and after being evaporated. The material does not undergo any noticeable change during the evaporation.

4.2.3 TTR

TTR presents as a red powder with some agglomeration. The material evaporates at a stable rate of 0.1 Å/s at 210°C. After evaporation, there is a slight colour change in the material. Figure 4.5 shows how the material looks before and after an evaporation. The material can also be re-evaporated under similar conditions.

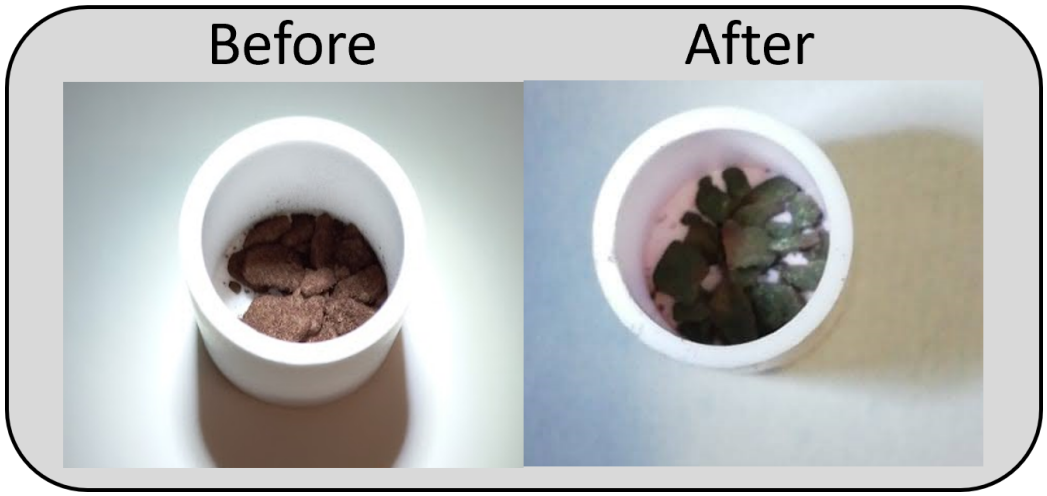


Figure 4.5: Images of TTR powder in a crucible before and after an evaporation. Before evaporation TTR appears to be a red powder with distinct agglomeration present. After evaporation the material appears more green.

4.2.4 TTIC4F

TTIC4F presents as a bright red powder with large disk like agglomerates. The material does not evaporate well, and a stable, appreciable rate was never reached. The temperature was increased to 350°C, which is higher than other organic small molecules used in this thesis which usually evaporate at temperatures < 300°C, with only a rate of 0.05 Å/s being reached. After an attempted evaporation the material looks burnt and most likely degraded. Figure 4.6 shows a picture of the material before and after evaporation. Nominally, less than 10 nm was recorded as being deposited during this evaporation despite using over 30 mg of material, suggesting that the material did not evaporate well.

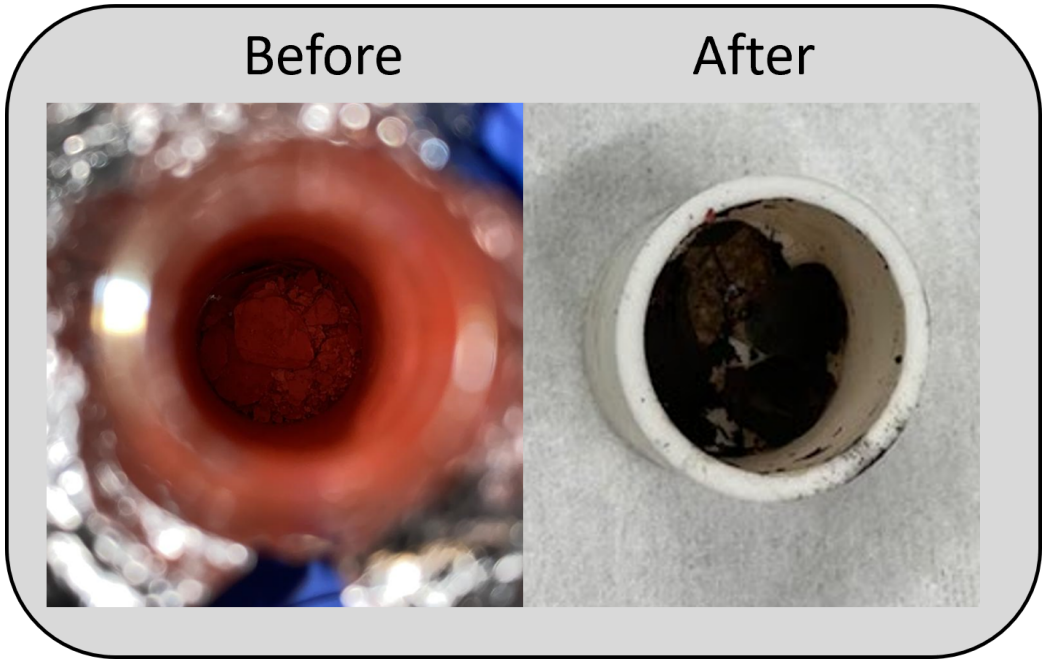


Figure 4.6: Images of TTIC4F powder in a crucible before and after an evaporation. Before evaporation TTIC4F appears to be a red powder with distinct agglomeration present. After evaporation the material appears burnt and is likely degraded.

As a result of TTIC4F not being able to evaporate well in vacuum the material was disqualified as a candidate for an evaporable NFA.

4.3 Optical Characterisation

4.3.1 BTIC-H

Figure 4.7 shows the optical constants of BTIC-H as determined by spectroscopic ellipsometry (SE), performed on 60 nm (nominal) films deposited on quartz substrates. Both reflectivity and transmission data were used for the fitting. The mean squared error (MSE) of the fit was less than 2, indicating an excellent fit to the data. The optical constants are consistent with the Kramers-Kronig relations,

and the refractive index follows normal dispersion criteria, i.e. at low (absorbing) wavelengths the refractive index increases, and at high (transparent) wavelengths the refractive index gradually decays. These features strengthen the reliability of the optical model used for the fit. The anisotropic features were further tested by modelling the out-of-plane components with a Cauchy layer, with the resulting fit showing a much higher MSE, implying that the model is indeed sensitive to the out-of-plane components. For the in-plane components absorption onset is approximately 760 nm, with a broad primary absorption peak at approximately 600 nm and a shoulder peak at 680 nm, with a peak extinction coefficient around 0.5, indicating good absorption, higher than many well-performing organic small molecules such as DTDCPB as well as C60, though not as strong as state-of-the-art solution processable NFAs such as Y6 [63] or the state-of-the-art evaporable small molecule donor DCV5T which showcase extinction coefficients above 1. Out-of-plane components show extinction coefficient peaks between 0.2 and 0.3, with similar peak positions to the in-plane components indicating that there is a mean preferential orientation in the thin film. Further details about the fitting can be found in the Appendix in section A.2.1.

The ratio between the maximum extinction coefficient in the in-plane and out-of-plane directions can be substituted into Equation 3.4 to yield an order parameter which gives an indication of the orientation of the S_1 optical transition dipole moment of the molecule (often taken to be parallel to the molecular backbone for molecules exhibiting a rod-like structure such as oligothiophenes like BTIC-H) with respect to the substrate normal. This value is calculated to be $S = -0.15$, indicating a shallow tilt angle of the molecule with respect to the substrate. However, the ratio between in-plane and out-of-plane components is not constant, and for the shoulder peak around 680 nm this ratio yields an order parameter of $S = -0.26$, which indicates a shallow tilt angle. This indicates a wavelength-

dependent orientation change, which may arise from the bending in the molecular structure as observed in [74].

The 680 nm shoulder likely represents J-type aggregate formation in the thin film [112, 8, 6], and indeed in solution there is no such shoulder peak in the absorbance spectrum shown in Figure 4.8. This shoulder also appears red-shifted in the absorbance of the spin-coated film, suggesting a similar aggregation mechanism is responsible for its formation. It is interesting to note that the extinction coefficient of the evaporated film does appear to be red-shifted compared to the absorbance of the spin-coated film. One explanation for this is that there might be more significant aggregation in the evaporated thin films.

Figure 4.9 shows the steady-state PL with a 505 nm excitation of a 20 nm thermally evaporated thin film of BTIC-H as well as the normalised in-plane extinction coefficient data from Figure 4.7 for comparison. Three distinct peaks are visible in the PL data at $\approx$ 1.46, 1.53, and 1.60 eV. Considering the spacing between the two higher energy peaks, it is possible that this originates from the radiative decay of the various states contributing to the the broad absorption between 1.7 and 2.8 eV seen in the absorption of the material.

4.3.2 PDIFCN2

Figure 4.10 shows the optical constants for PDIFCN2 using SE. The mean squared error (MSE) of the fit was less than 2, indicating an excellent fit. Measurements were performed on 20 nm (nominal) films deposited on quartz substrates and silicon wafers with a native oxide, with both data sets used in an multi-sample analysis approach. The optical constants follow Kramers-Kronig relations, the refractive index follows normal dispersion criteria, i.e. at low (absorbing) wavelengths the refractive index increases, and at high (transparent) wavelengths the refrac-

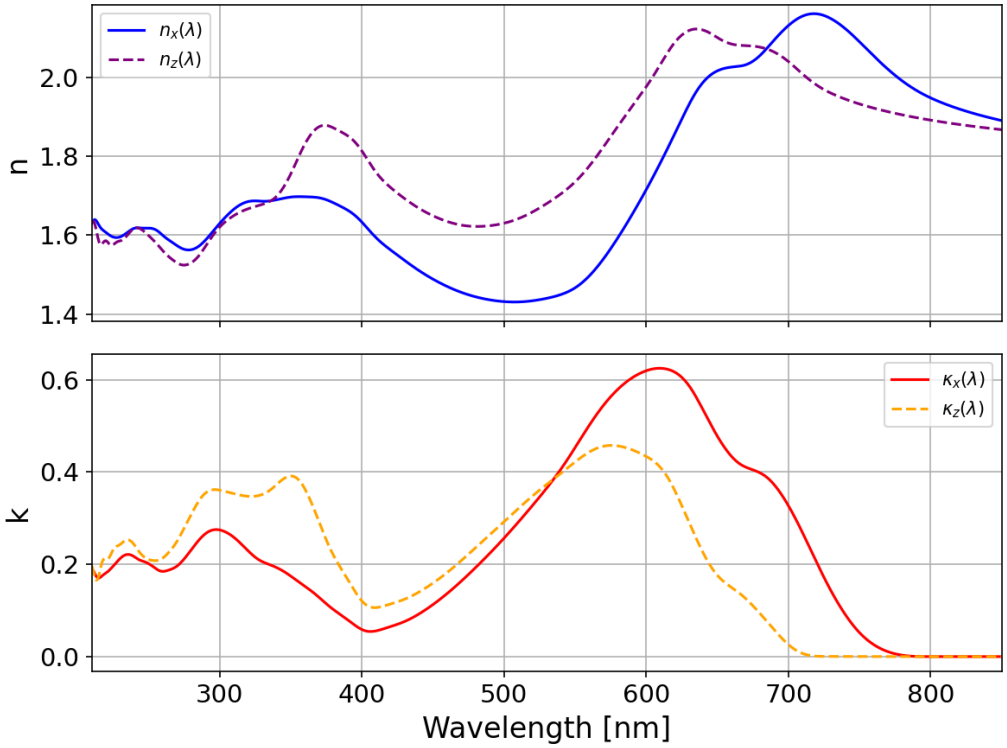


Figure 4.7: Optical constants of BTIC-H thin films modelled using spectroscopic ellipsometry data taken on quartz substrates. Refractive index (top) and extinction coefficient (bottom) values are shown as a function of wavelength. In-plane and out-of-plane components are shown, where the plane refers to that of the substrate. Fits were obtained using an anisotropic bspline model, and the resulting mean squared error of the fit was less than 2, indicating an excellent fit to the model. Further details of the fitting can be found in Appendix A.2.1.

tive index gradually decays. These features strengthen reliability of the model. The anisotropic features were further tested by modelling the out-of-plane components with a Cauchy layer, with the resulting fit showcasing a much higher MSE, implying that the model is indeed sensitive to the out-of-plane components. For the in-plane components absorption onset is approximately 560 nm, with two distinct absorption peaks at approximately 530 and 490 nm, with peak extinction coefficients between 0.4 and 0.5. Out-of-plane components show extinction coefficient peaks between 0.2 and 0.3, with similar peak positions to the in-plane

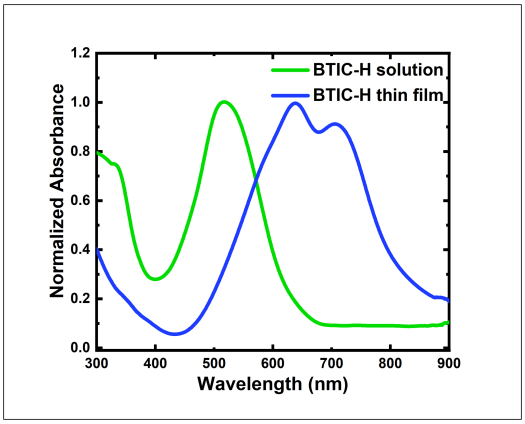


Figure 4.8: Normalised absorbance of BTIC-H in $CHCl_3$ solution (green) and of BTIC-H in a spin-coated thin film (blue). Reproduced with permission from [74].

components, indicating that there is a mean preferential orientation in the thin film. Using Equation 3.4 yields an order parameter of $S_\mu = -0.16$, indicating that the molecules are on average tilted from the substrate at a shallow angle. See Appendix A.2.2 for further details on the fitting.

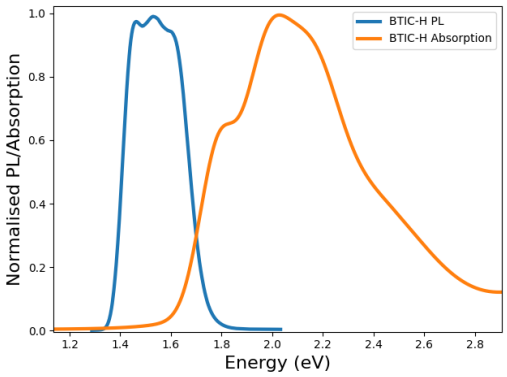


Figure 4.9: Normalised steady-state photoluminesence data shown of a 20 nm BTIC-H film excited with a 505 nm laser (blue), and normalised in plane extinction coefficient in Figure 4.7 (orange).

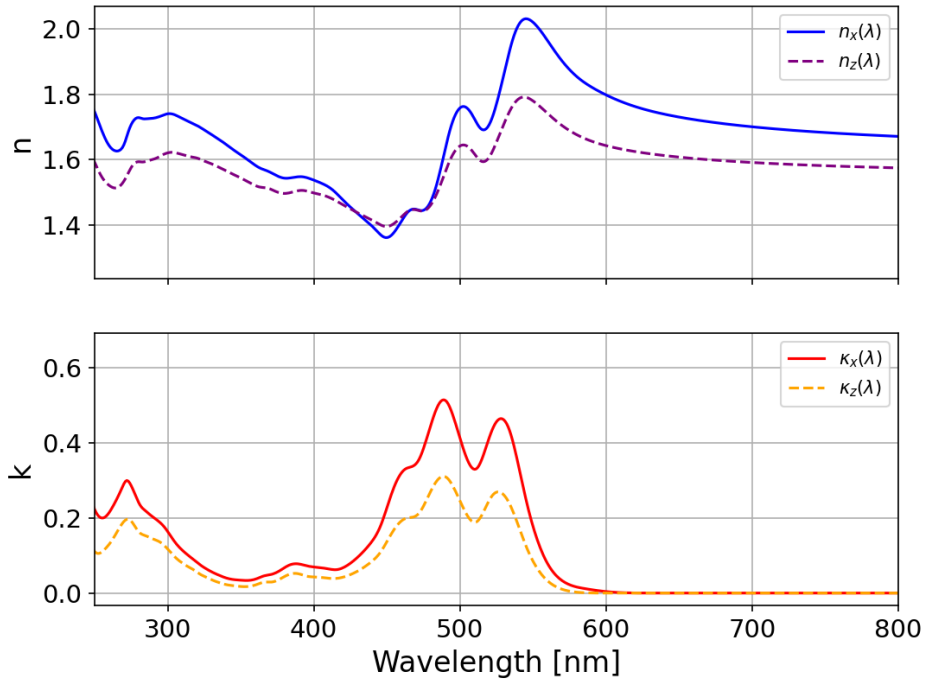


Figure 4.10: Anisotropic optical constants of 17 nm films of PDIFCN2, calculated via an optical model based on spectroscopic ellipsometry measurements. Measurements were performed on quartz substrates and silicon wafers with a native oxide, with both data sets used in an multi-sample analysis approach. MSE of the fit is ≈ 1.9. Fitting details can be found in the Appendix A.2.2.

4.3.3 TTR

Figure 4.11 shows the optical constants of TTR using SE. The mean squared error (MSE) of the fit was less than 14. This MSE is higher than observed in other ellipsometry models used in this chapter, however, samples used in the fit included 20 nm (nominal) films deposited on an unpatterned ITO layer on glass substrates and Si substrates with a native oxide. These substrates exhibit many absorption features than standard glass substrates and despite having good fits of the bare substrates, fits of samples using these substrates typically exhibit higher MSE values despite showing physically consistent models. Please see the Appendix A.2.3 for a more details on the fitting.

The optical constants follow Kramers-Kronig relations, the refractive index follows normal dispersion criteria, i.e. at low (absorbing) wavelengths the refractive index increases, and at high (transparent) wavelengths the refractive index gradually decays. These features strengthen reliability of the model. The anisotropic features were further tested by modelling the out-of-plane components with a Cauchy layer, with the resulting fit showcasing a much higher MSE, implying that the model is indeed sensitive to the out-of-plane components. For the in-plane components absorption onset is approximately 660 nm, with a narrow primary absorption peak at approximately 584 nm and a narrow doublet peak at 535 nm and 500 nm, with a peak extinction coefficients in between 0.3 and 0.4. Out-of-plane components show extinction coefficient peaks between 0.2 and 0.3, with similar peak positions to the in-plane components, indicating that there is some minor preferential orientation in the thin film. Using Equation 3.4 here yields an order parameter of $S = 0.13$, suggesting a steeper tilt between the molecule and the substrate than seen for either PDIFCN2 or BTIC-H.

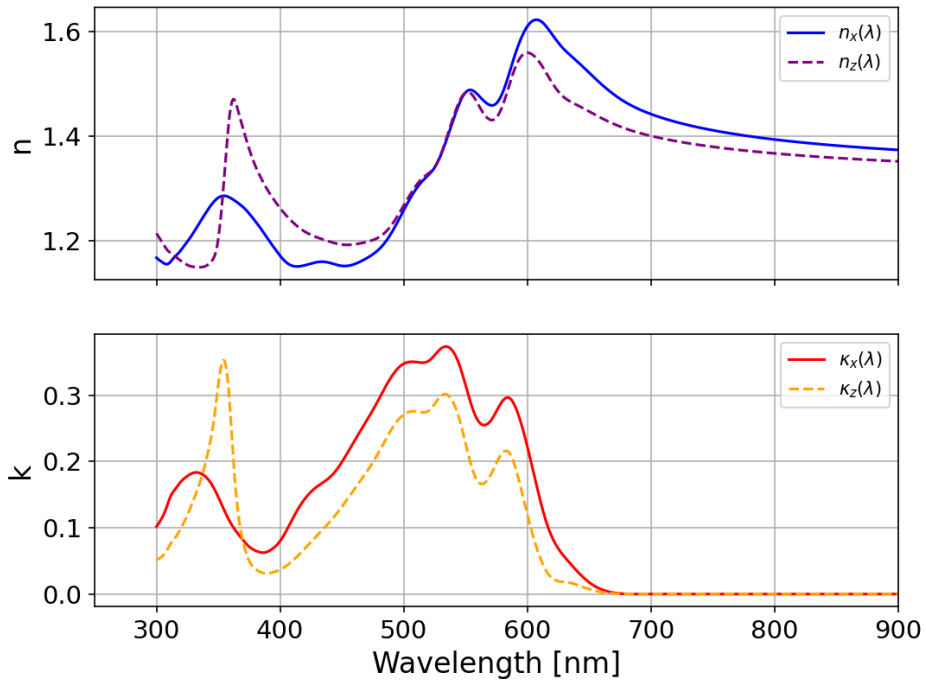


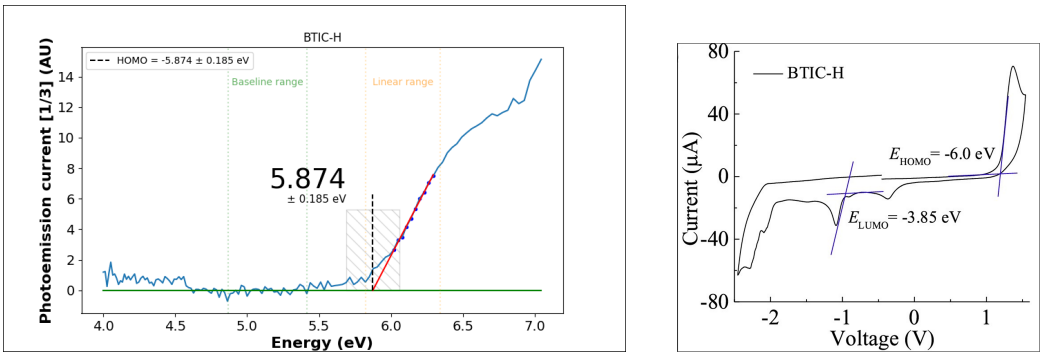
Figure 4.11: Optical constants of TTR thin films modelled using spectroscopic ellipsometry data taken on various substrates with varying thickness. Refractive index (top) and extinction coefficient (bottom) values are shown as a function of wavelength. In-plane and out-of-plane components are shown, where the plane refers to that of the substrate. Fits were obtained using an anisotropic bspline model, and the resulting mean squared error of the fit was less than 14. Fitting details can be found in the Appendix A.2.3.

4.4 Energy Level Characterisation

4.4.1 BTIC-H

Figure 4.12a shows the Ambient Photoelectron Spectroscopy (APS) data of a BTIC-H film deposited on an ITO on glass substrate. Analysis of the data using the intersection between the linear regime and the baseline regime of the data is shown in the image, and yields an IP of -5.9 ± 0.2 eV. This value is well below

that of many small molecule donors. A comparison to cyclic voltammetry data of the molecule taken from [74] is shown in Figure 4.12b, showing a deeper HOMO. It should be noted here that calculating the HOMO value from APS data is considered more reliable than doing it from CV data given that the sample is more representative of what is found in a device, i.e. an evaporated thin film rather than a solution, and there is no interaction with the solvent which may need corrections to account for and may lead to misleading conclusions as result [93].



(a) (b)

Figure 4.12: a) Ambient Photoelectron Spectroscopy measurement of a 30 nm BTIC-H film deposited on an ITO-coated glass substrate. The intersection of a linear fit to the data with the baseline are shown in the plot, yielding a HOMO value of -5.9 ± 0.2 eV. b) Cyclic voltammetry measurements showing estimates of the HOMO and LUMO of BTIC-H in solution, -6 and -3.85 eV respectively. Potential vs. Fc/Fc+, produced from ref [74].

We can estimate the EA of BTIC-H using Equation 3.6, as discussed in Chapter 3, which relates the EA measured by IPES to the optical gap of a series of molecular organic semiconductor compounds. We can then compare this value to that measured in the literature to gain confidence in the value of the LUMO. Applying the approach above to BTIC-H, using the optical data from Figure 4.7 yields an EA of -3.6 ± 0.7 eV. The large uncertainty comes mostly from the 0.5 eV uncertainty in the offset in the expression above, and highlights the challenge in

precisely determining the EA. However, this approach does give us an estimate to work with. Nevertheless with an IP of ≈ 5.9 eV and an EA of ≈ 3.6 eV, BTIC-H is well positioned, energetically at least, as a non-fullerene acceptor.

4.4.2 PDIFCN2

While the energy levels of PDIFCN2 were not directly measured in this thesis, literature results [113] of the material report an estimated LUMO of -4.5 eV and a HOMO of -6.6. These results were calculated using the reduction potential of the material dissolved in 0.1 M $TBAPF_6$ in CH_2Cl_2 solution to estimate the LUMO energy value, and the optical gap with this value to calculate the HOMO. This is not the ideal way to measure the energy levels, APS data would provide more reliable data, but the values can be used as a guide nonetheless.

4.4.3 TTR

Figure 4.13 shows the APS data of a TTR film deposited on an ITO-coated glass substrate. Analysis of the data using the intersection between the linear regime and the baseline regime of the data is shown in the image, and yields an IP of -5.8 ± 0.1 eV. Following the same approach by using the optical gap calculated from the absorption onset of the extinction coefficient of TTR shown in Figure 4.11, we estimate EA for TTR to be -3.3 ± 0.7 eV. The EA of TTR is quite high, and similar to its parent molecule T2-ORH [72] it can probably be considered a wide-gap acceptor as a result, which means its EA is actually quite close to that of many donor molecules and may result in too small an offset and thereby inhibit efficient exciton dissociation in devices where TTR is used as an acceptor.

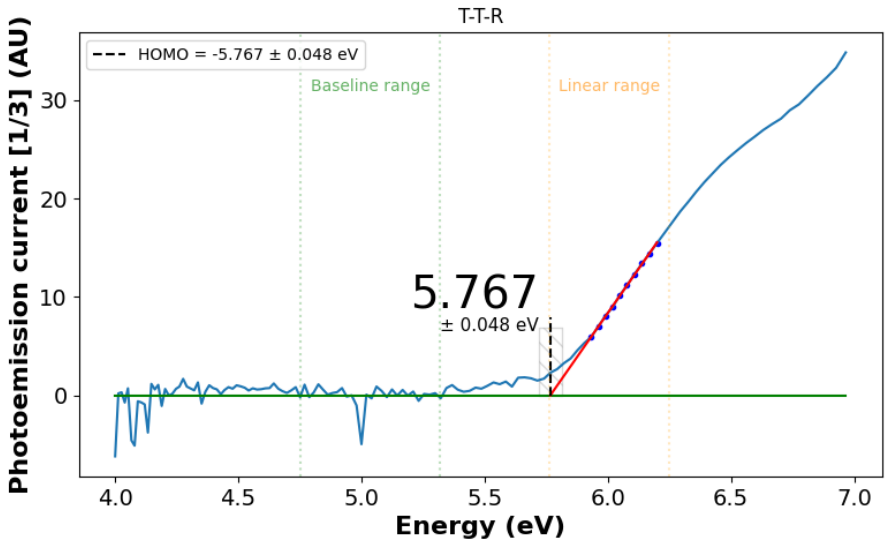


Figure 4.13: APS data of a TTR 20 nm thin film deposited on an ITO substrate. The intersection of a linear fit to the data with the baseline are shown in the plot, yielding an IP value of -5.8 ± 0.1 eV.

4.5 Microstructure Characterisation of BTIC-H

From the optical and energetic characterisation of the candidate materials BTIC-H was considered the most promising and further microstructure characterisation was carried out.

The surface morphology of BTIC-H films were studies using atomic force microscopy (AFM), and the bulk microstructure was studied with X-ray Reflectivity (XRR) and Grazing Incidence Wide Angle X-ray Scattering (GIWAXS) measurements. Near Edge X-ray Absorption Fine Structure (NEXAFS) spectroscopy was used to better understand the molecular orientation of the film, and the existing SE measurements shown earlier in this chapter were used to complement this analysis.

The film surface of a 20 nm (nominal) BTIC-H film deposited with a rate of $0.1/s$

on a glass substrate held at room temperature was studied using atomic force microscopy (AFM), shown in Figure 4.14. The film appears to be homogeneous and the mean surface roughness was calculated to be 0.6 ± 0.1 nm.

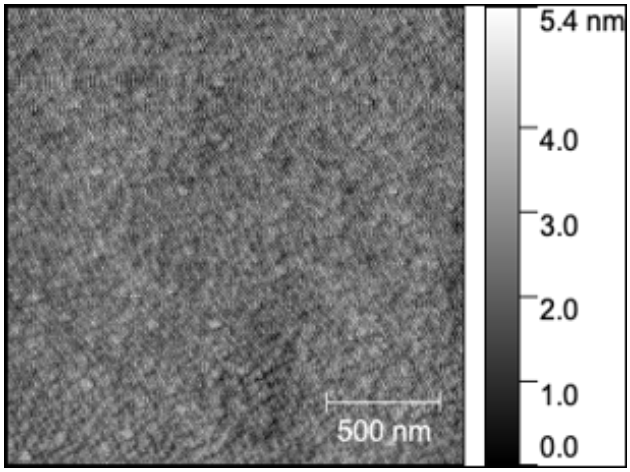


Figure 4.14: AFM image of a 20 nm (nominal) BTIC-H film deposited on a glass substrate held at room temperature. Surface roughness (RMS) of 0.6 ± 0.1 nm was calculated. There is a comb-like artefact present on the scans, due to a filtering fault on the microscope, resulting in a 50 Hz 'click'. The amplitude of the click is of a similar order of magnitude to the features of the film meaning the artefact is particularly visible. In this case, it was not possible to use Fourier notch filtering on the 2D image because the random distribution of phases across all the many horizontal scan lines in the image averages this component to around zero. The presence of these artefacts does not change the analysis. Adapted from [14].

Figure 4.15 shows the X-ray reflectivity data of a 40 nm (nominal) BTIC-H film deposited on a glass substrate. The actual thickness is calculated from the fit, and is 45.3 ± 0.1 nm. The data was taken on a Rigaku SMARTLab diffractometer and the data analysed using GenX [114]. The surface roughness (root mean squared) is given as 1.14 ± 0.05 nm, indicating a relatively smooth and homogenous film surface. This value is slighlty larger than observed from the AFM results on a 20 nm film observed in Figure 4.14, and may have been the result of the film being thicker. The thin film density is given as 1.02 ± 0.01 g/cm^3, which is lower than the typical density observed for other small molecules used in this thesis, which

are closer to ≈ 1.3 g/cm^3.

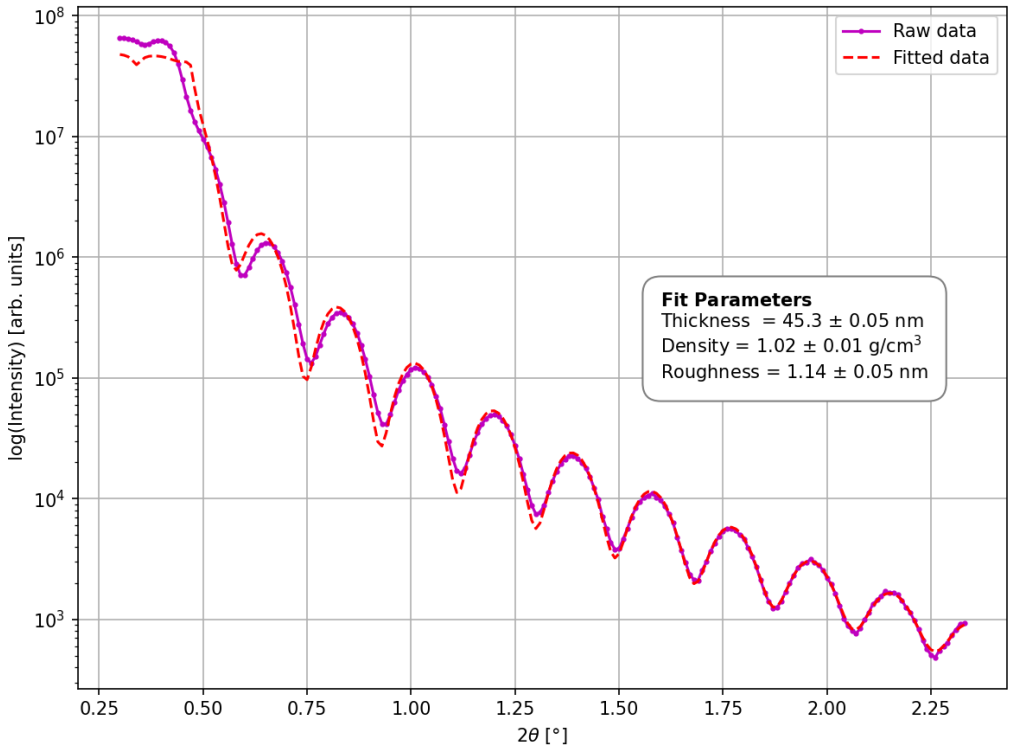


Figure 4.15: Fitted X-ray Reflectivity data (purple dots and line) of a 40 nm (nominally) BTIC-H evaporated on a glass substrate, shown alongside a fit of the data (red dashed lines). Thickness, density and roughness values calculated from the fit are shown on the plot. The data was fitted using GenX[114] and data was measured with a Rigaku SMARTLab diffractometer.

Figure 4.16 shows a Grazing Incidence Wide Angle X-ray Scattering image of a 20 nm (nominal) BTIC-H film deposited on a glass substrate. There is a strong Bragg peak present in the image at $q_z \approx 0.5^{-1}$, which corresponds to 12.6 nm in real space dimensions, in the out of plane direction, indicative of lamellar stacking of the BTIC-H molecules. This has been attributed to the dihedral angle in the bithiophene core of the molecule caused by the hexyl side chains [74]. Also visible is weak scattering at $q_x \approx 1.8^{-1}$, which is indicative of $\pi - \pi$ stacking. Both peaks indicate some ordering is present in the thin film, and that the

molecules have a preferential orientation. This observation reinforces the finding of a molecular tilt calculated from the optical models based on the SE data shown earlier in this chapter.

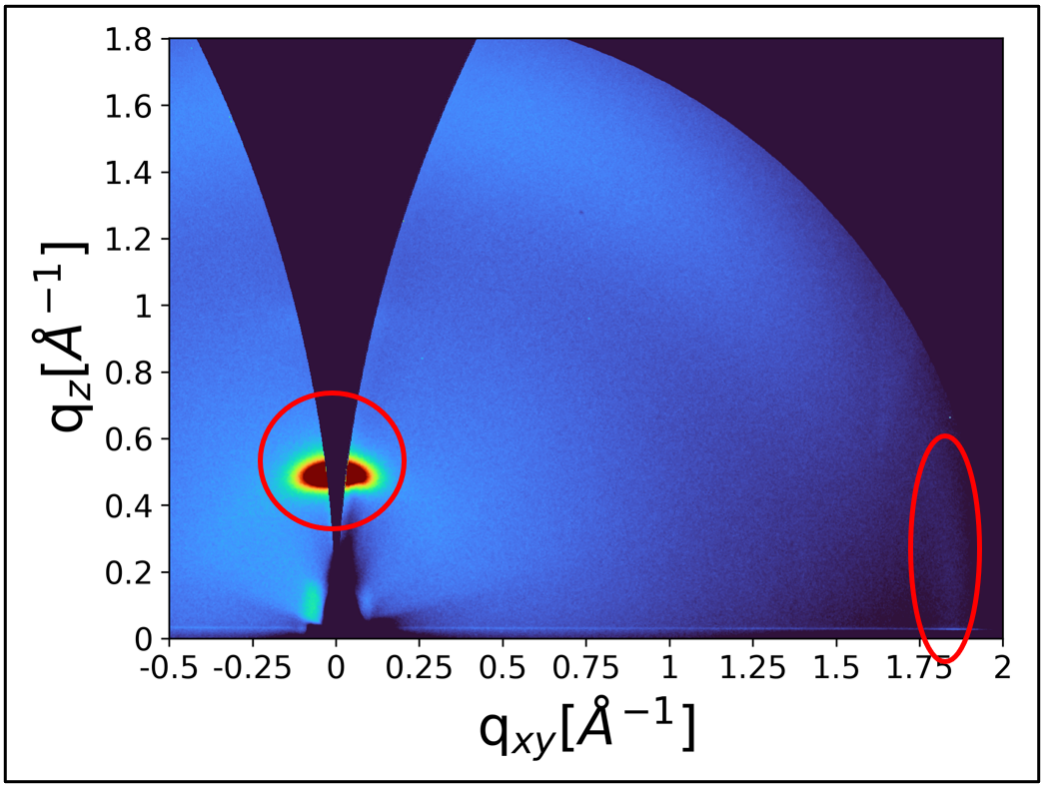


Figure 4.16: GIWAXS image of a 20 nm (nominal) BTIC-H film deposited on a glass substrate held at room temperature with a rate of $0.1/s$. Circled in red are Bragg peaks indicating strong scattering at $q_z \approx 0.5^{-1}$, and weaker scattering at $q_x \approx 1.8^{-1}$. Measurement was taken at XMaS: The UK Materials Science Facility (BM28) at the European Synchrotron Radiation Facility (ESRF; experimental session 28-01-1306). A MAR detector was used to acquire data at 10 KeV.

To better understand this orientation, NEXAFS measurements of the Carbon K edge were taken at multiple angles with respect to the incoming beam (Figure 4.17a). This data was taken at the B07 beamline at the Diamond Light Source in July 2021 (beamtime SI29412). These measurements reveal information about excitation of atomic shell electrons to excited states in the molecule. In particular,

the $1s \rightarrow \pi^*$ resonances are analysed at different angles to understand how the transition dipole moments for these transitions are preferably oriented, which can then reveal information about the face on orientation of the molecule itself. The data can be fitted with Gaussian oscillators (shown in Figure 4.17b) and the areas under the peaks can be used with Equation 3.5 to calculate the tilt angle of the molecule with respect to the substrate normal. It should be noted this value reflects the first moment of the angular distribution, and is assumed to reflect the mean of this distribution. This is discussed in more detail in the Methods section of Chapter 3. The data in Figure 4.17a and Figure 4.17b shows that most peaks show the same behaviour as a function of angle, however the narrow doublet at 286.75 eV and 286.98 eV show slightly different behaviour, with them showing less angular dependence than other pre-edge peaks. The peaks at lower energies often arise due to $C = C$ π^* resonances along the backbone of the molecule and since this dipole moment is perpendicular to the plane of aromatic rings in organic molecules it can be used as a proxy for the facial orientation of the molecule [81]. The doublet is suspected to arise from the $C \equiv N$ π^* resonance [81], which in this case gives us information about the CN end groups of the molecule. Fitting these areas under these peaks separately reveals that there is a 60.2 ± 0.07 ° mean facial orientation for the $C = C$ π^* resonance and a $55.13 \pm 0.18°$ mean facial orientation for the $C \equiv N$ π^* resonance, with respect to the substrate normal. The value for the $C \equiv N$ π^* resonance is quite close to $54.7°$, which suggests that the end groups could actually be randomly oriented. It is also possible that this difference in facial orientation is responsible for the wavelength-dependent ratio between in-plane and out-of-plane extinction coefficients observed from the SE models for BTIC-H films observed earlier in the chapter in Figure 4.7.

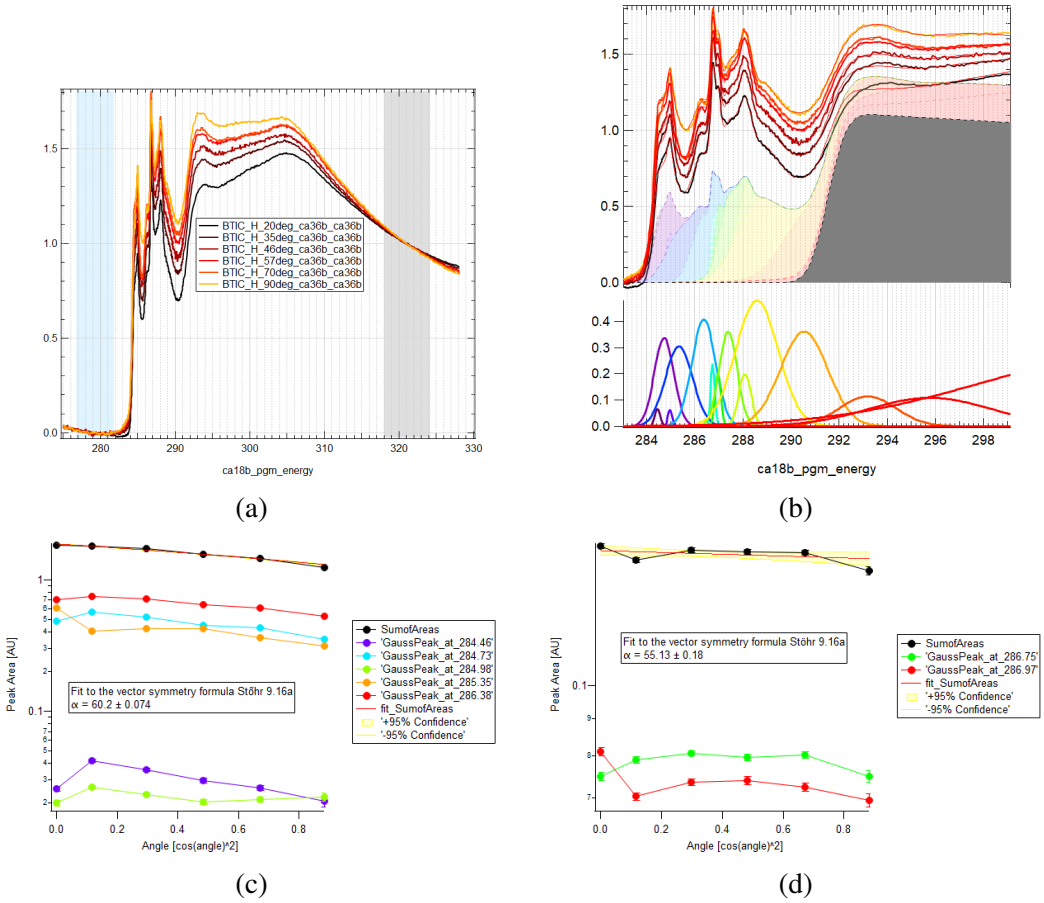


Figure 4.17: a) NEXAFS measurements of a 60 nm (nominal) thin film deposited on a ITO on glass substrate at multiple angles. b) Gaussian fits to the data in a). Fits of the areas under peaks associated with (c) $C = C$ and (d) $C \equiv N$ π^* resonances to the orbital tilt expression assuming vector symmetry.

4.6 Summary and Conclusions

Table 4.1 summarises key results from the optical and energetic characterisation found in this chapter. While PDIFCN2 is reported to have an even deeper-lying IP -6.6 eV, it also has a relatively deep EA of -4.4 eV which may introduce serious losses in an organic solar cell with conventional donors. TTR on the other hand has an appropriate IP of -5.8 eV which positions it well relative to many small

molecule donors, however its EA of -3.3 eV is quite shallow, which may lead to inefficient exciton dissociation in organic solar cell devices. Of the molecules investigated thus far BTIC-H is best positioned as an acceptor given its combination of a deep-lying IP of -5.9 eV as well as an EA of -3.6 eV that allows for a decent energetic offset with a variety of donor molecules. Additionally, its extinction coefficient of ≈ 0.6 is higher than the both PDIFCN2 and TTR, which range between 0.5 and 0.4, respectively. Chapter 5 will focus on BTIC-H as an acceptor in organic solar cell devices, however preliminary devices were nevertheless investigated for both TTR and PDIFCN2, with the data shown in the Appendix A.3 and A.4.

Material	**Peak Extinction Coefficient**	**HOMO (eV)**	**LUMO (eV)**
BTIC-H	0.63	-5.9 ± 0.2	-3.6 ± 0.7
PDIFCN2	0.5	-6.6	-4.5
TTR	0.4	-5.8 ± 0.1	-3.3 ± 0.7

Table 4.1: A summary of the peak extinction coefficient, HOMO and LUMO values calculated for candidate NFA materials studied in this chapter. Values which were deemed to be good are highlighted in green, bad in red, and unclear in orange.

5 | Using BTIC-H as an NFA in evaporated organic solar cells

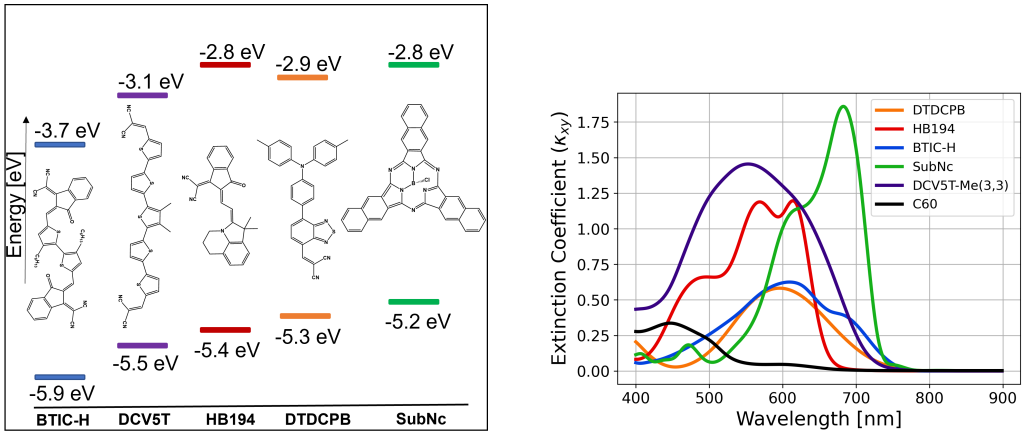
5.1 Introduction

This chapter will show the results from a device-centred study using BTIC-H in organic solar cell devices. The first section will showcase the use of BTIC-H in planar heterojunction (PHJ) devices using several organic small molecule donors which were selected to pair with BTIC-H based on their energy levels and/or their absorption spectra. Next, based on the results of the PHJ devices, a more detailed investigation follows with the use of DCV5T as a donor in bulk heterojunction (BHJ) devices, and compares the results to those using C_{60} as an acceptor. The results are discussed and analysed. The overall conclusion from this study is that evaporated BTIC-H PHJ devices using DCV5T as a donor outperform solution processed BHJ devices using PCE12 as a polymer donor, and show comparable results to C_{60} in PHJ devices. However, when moving to a BHJ architecture the extracted charges in the evaporated devices significantly decreases, contrary to what is expected for a typical BHJ device. The reasons for this are investigated. In summary, BTIC-H shows promise as an evaporable NFA, however, device and perhaps further material optimisation is required in order to reach performance levels more comparable with those seen by other solution processed NFAs.

5.2 PHJ Devices

Following the thin film characterisation of BTIC-H, various donors were selected to pair with the NFA to use in a PHJ device. These donors have shown good per-

formance with C_{60} in the literature. The structures and energy levels are shown in Figure 5.1a, with EA values being estimated using Equation 3.6 to use a common approach for good comparison, and in-plane extinction coefficients of the molecules are shown in Figure 5.1b, following the same approaches used to characterise BTIC-H thin films in the previous section. The APS data of the donors is shown in Appendix A.5 and the exact values used for the LUMO estimation are shown in Appendix A.6.



(a) (b)

Figure 5.1: a) Chemical structures and energy levels of the molecules used in this chapter. IP levels were measured via Ambient Photoelectron Spectroscopy. EA levels were estimated using Equation 3.6 [84] that relates EA levels probed via IPES to the sum of the HOMO level and energy of absorption onset, which is defined in Chapter 3. The latter is determined from the absorption onset in the extinction coefficients in b). Extinction coefficients were calculated from data obtained via spectroscopic ellipsometry using anisotropic models where relevant, with only the device relevant in-plane data shown, and with C60 data included as a reference. Reproduced from [14] with permission.

The stack used for the PHJ devices is shown in Figure 5.2a. All devices were made using 20 nm of donor and 20 nm of the BTIC-H acceptor in the active layer. Current voltage curves are shown in Figure 5.2b, with key performance metrics from the measurements summarised in Table 5.1.

The open circuit voltage (V_{OC}) for all PHJs, except SubNc, is between 0.94V and 0.96V. SubNc devices show the lowest V_{OC} in the study with values around 0.78 V, which could be explained by the large HOMO offset between BTIC-H and SubNc.

Photocurrents vary significantly between donors, with SubNc providing the highest short circuit current (J_{SC}) at 3.55 ± 0.05 mA/cm^2. This is likely due to the high extinction coefficient of the material; therefore, more excitons are generated through photon absorption in the SubNc layer which contribute to charge generation at the interface. HB194 PHJs showed the lowest J_{SC} at 0.4 ± 0.04 mA/cm^2 despite having a stronger absorption than DTDCPB, which showed a J_{SC} of 1.16 mA/cm^2. DCV5T PHJs showed a J_{SC} of 2.43 mA/cm^2. There are other factors to consider here, such as the interference pattern and the spectrum of the illuminating light, and these are taken into account via transfer matrix models discussed below.

Fill factors for all PHJs were less than 50%. HB194 PHJs shows a clear 'S' shape and FF below 25% which may indicate contact issues in the device [115, 116] which could also explain the low photocurrent despite the relatively high energetic offset between HB194 and BTIC-H. DCV5T and SubNc PHJs showed FF values of $\approx 42\%$, with DTDCPB PHJs showing a lower FF at 33%. Figure 5.2c shows the JV of each PHJ device taken under dark conditions. The inverse slope of the JV at the V_{OC} of the HB194 PHJ data is significantly greater than that of the other devices, suggesting that the series resistance in the HB194 PHJ devices was greater than exhibited in the other devices. This is a further indication of more challenging charge transport issues in the HB194 devices compared to the rest of the PHJ devices.

The dissociation of excitons into free charges is likely not 100% efficient for all

tested donors. The moderate FF, lower than what one might expect for PHJ devices [68], could indicate field-assisted charge generation. Since the electric field in a solar cell is higher at J_{SC} than at the maximum power point, a charge generation process that depends on the electric field, and thus the applied voltage, would restrict the FF. This hypothesis is reinforced by comparing the photocurrent at reverse bias with the J_{SC} as seen in Figure 5.2d, which shows that at reverse bias there are significant gains in the photocurrent for the devices, as indicated in Table 5.1. This suggests that the charge extraction and/or the exciton dissociation is poor. It should be noted that this effect is most pronounced for HB194 and SubNc devices, but also that the data for DCV5T devices does not extend as far in the reverse bias and an equivalent comparison at the same reverse bias suggests that HB194 suffers from this problem more so than the rest of the samples studied ($\approx 40\%$ compared to $70 - 80\%$).

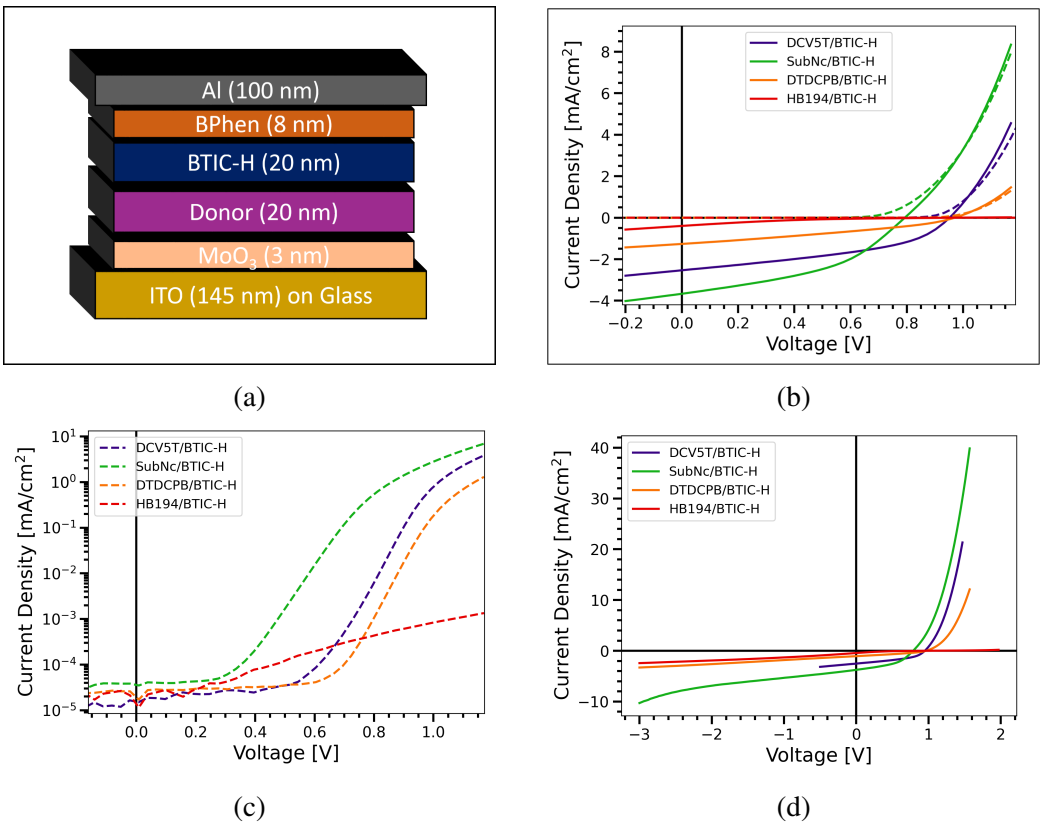


Figure 5.2: a) Device stack for PHJ devices. BPhen was used as ETL (electron transport layer), and MoO3 was used as the HTL (hole transport layer), nominal thicknesses were ITO (110 nm)/MoO3 (3 nm)/ Donor (20 nm/ BTIC-H (20 nm)/ BPhen (8 nm)/ Al (100 nm). JV measurements under approximately 1 sun illumination (solid lines) and in the dark (dashed lines) of individual PHJs using donors DCV5T, SubNc, DTDCPB, and HB194. c) Log plot of dark JV measurements of the same devices as b). d) Extended JV scans of the samples in b) showing behaviour at reverse bias.

Optical Transfer Matrix Method (TMM) simulations were also carried out to better understand the obtained J_{SC} by considering the effects of the multilayer environment that the light has to propagate through, such as the interference pattern produced in the stack, as well as the spectrum of the incoming light vs the absorption spectrum of the active layer of these devices. In a PHJ device only a certain volume surrounding the interface will contribute to charge generation in

	DCV5T	DTDCPB	HB194	SubNc
V_{OC} (V)	0.96 ± 0.01	0.96 ± 0.01	0.94 ± 0.01	0.78 ± 0.01
FF (%)	41.9 ± 0.3	33.2 ± 0.2	13.4 ± 0.1	42.5 ± 0.2
$J_{SC\ measured}$ (mA/cm^2)	2.43 ± 0.10	1.16 ± 0.05	0.4 ± 0.04	3.55 ± 0.05
Equiv. Intensity (AM1.5G)	0.95	0.96	0.94	1.01
$J_{SC\ corrected}$ (mA/cm^2)	2.55 ± 0.11	1.25 ± 0.05	0.43 ± 0.04	3.51 ± 0.05
PCE (%)	1.02 ± 0.04	0.40 ± 0.01	0.05 ± 0.01	1.20 ± 0.03
Voltage Loss	0.81 ± 0.02	0.80 ± 0.02	0.95 ± 0.02	0.92 ± 0.02
$J_{measured}$ at -3 V	N/A	3.3 ± 0.1	2.4 ± 0.1	10.36 ± 0.1
$J_{measured}$ at -0.5 V	3.2 ± 0.1	1.4 ± 0.1	0.9 ± 0.1	4.6 ± 0.1

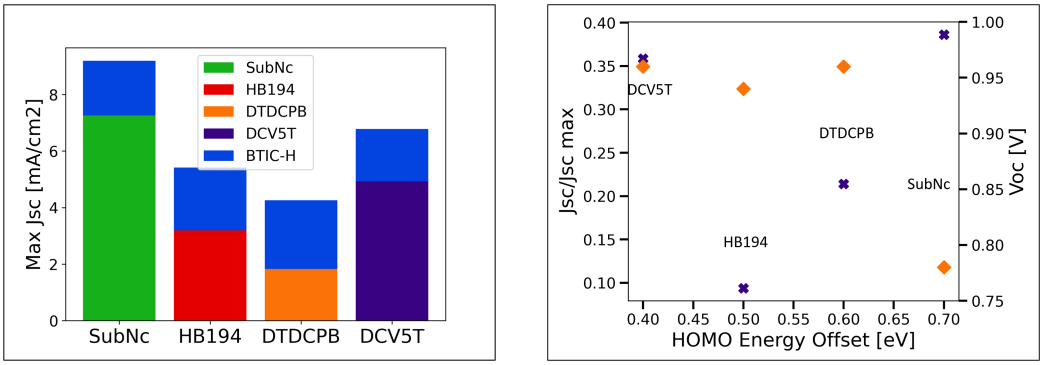
Table 5.1: Mean key metrics from JV measurements of donor/BTIC-H devices shown in Figure 5.2b. The voltage loss is calculated via $\Delta V = E_g/q - V_{OC}$, where E_g is calculated from the inflection point of the EQE. Uncertainties indicated are given by the standard deviation in the data, with sample sizes around 10-11 devices each. Equivalent AM1.5G spectra intensities are shown for the measurements, and mismatch corrected J_{SC} values are also shown for a scaled equivalent 100 mW/cm^2 AM1.5G spectra.

the device. The total size of this region is governed by the materials exciton diffusion length. Comprehensively determining the exciton diffusion length for all the materials used in this study is beyond the scope of this thesis, however, values from literature were used for SubNc (20 nm) [109], which is remarkably large and DCV5T (10 nm) [117]. When no value could be found, 10 nm was assumed.

By normalizing the J_{SC} by the simulated maximum J_{SC} , which assumes 100% internal quantum efficiency, i.e. that every photon absorbed within the device results in an extracted charge pair, we can account for different donor absorptions and thus get an estimate of the impact of the energetic offsets on charge generation efficiency (assuming collection is the same in all devices, which should be the case for PHJs unless the layers are too thick). Simulated maximum J_{SC} contributions are shown in Figure 5.3a. Figure 5.3b shows the relation of the HOMO offsets on this $J_{SC\ meas}/J_{SC\ max}$ ratio, which suggests that as the energetic offset for both the HOMO gets larger, surprisingly, charge generation becomes less efficient in

these devices. The exception to this trend is SubNc, which has also been shown in literature to generate charges efficiently in a neat film, showcasing a $J_{SC} \approx 2$ mA/cm^2 in a single (photo-active) layer device [118], which will inflate its J_{SC} relative to other devices.

Also shown in Figure 5.3b is the relationship between V_{OC} and HOMO offset, showing that the V_{OC} generally decreases with increasing offset, an expected result considering the established relation between donor HOMO and acceptor LUMO and V_{OC} [119]. All HOMO offsets are larger than or equal to 0.4 eV which is thought to facilitate efficient charge generation for solution processed NFAs [93, 29]. From a pure energy levels perspective, larger offsets (to a certain extent) should yield more efficient charge generation, which is not the case in our dataset based on BTIC-H. The exact reasons for this are unclear. Possible reasons are that the energetic landscape at the buried interface itself might be very different to the energy levels probed during APS measurements, that we already enter the Marcus-inverted regime [120], or that factors other than energetics governing the charge transfer processes occurring when transitioning from a bound to an unbound state.

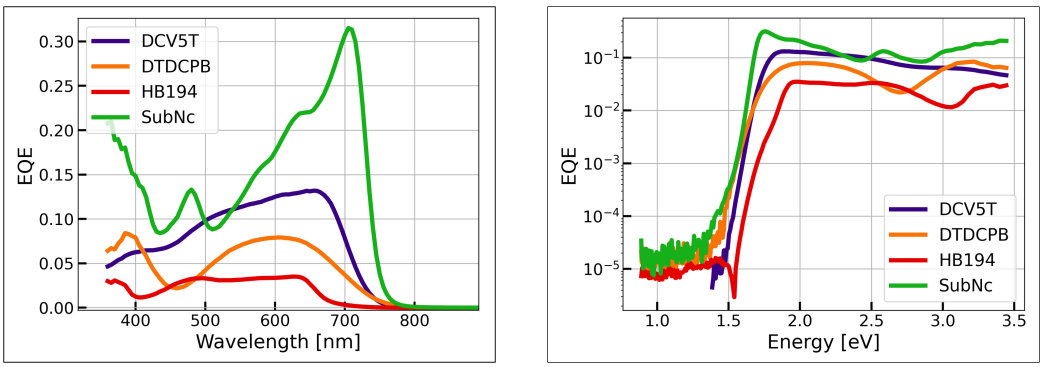


(a) (b)

Figure 5.3: a) Plot showing the simulated contributions to the maximum J_{SC} assuming 100% internal quantum efficiency and exciton diffusion length of 20 nm (SubNC) and 10 nm (DCV5T, HB194, DTDCPB), bottom bars indicate donor contributions and top bars indicate BTIC-H contributions, simulated with a transfer matrix method model adapted from [121]. b) Plot showing the effect of HOMO energy offset between donors and BTIC-H on the ratio between the J_{SC} to the simulated J_{SC} assuming 100% IQE, and the V_{OC} . Purple crosses indicate the $J_{SC\ meas}$ / $J_{SC\ max}$ ratio, diamonds indicate the V_{OC} . The donor molecules the offsets refer to are listed on the image.

The external quantum efficiency (EQE) of the PHJs was measured with a high dynamic range over up to 5 orders of magnitude and is shown in Figure 5.4a. EQEs are less than 15% with the exception of the SubNc devices which show a peak EQE of 30%, and values and trends match the measured J_{SC} reported above. Figure 5.4b shows the EQE on the logarithmic scale, and no clear shoulder is visible in most of the tails of the EQE, with the exception of HB194, implying that the CT state is either quite close to the singlet, or that its absorption and oscillator strength is very weak.

Voltage loss analysis was carried out following the detailed balance principle as discussed in Chapter 3 and the photovoltaic gap of each device was taken to be the inflection point of the EQE. Due to SubNc devices displaying a slowly decaying tail below 1.5 eV, which cannot be fully resolved with our setup, these devices

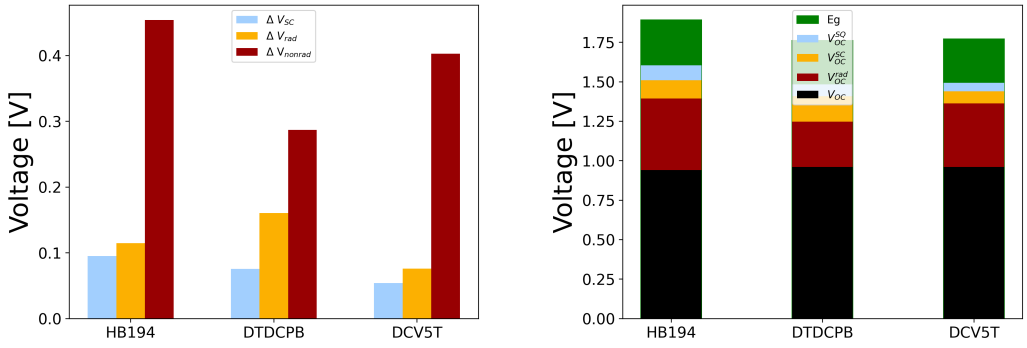


(a) (b)

Figure 5.4: a) External Quantum Efficiency (EQE) measurements of PHJ devices shown in Figure 5.2, plotted on a linear scale. b) Same EQE as in a), plotted on a logarithmic scale. No shoulders are discernible in the EQE, except for the HB194 PHJ at ≈ 1.7 eV.

were omitted from the voltage loss analysis. The results of the analysis are shown in Figure 5.5, with individual loss values shown in Table 5.2.

Breaking down the voltage loss yields the following: $\Delta V_{J_{SC}}$ follows the J_{SC} shown in Figure 5.2b, with highest losses in HB194/BTIC-H (0.09 V) and lowest losses in DCV5T/BTIC-H (0.05 V), with DTDCPB/BTIC-H showing losses of 0.08 V. ΔV_{rad} represents the losses arising from radiative recombination from sub-gap states, commonly attributed to be CT states [87]. DTDCPB/BTIC-H and HB194/BTIC-H show the highest ΔV_{rad} (0.16 V and 0.11 V respectively), while DCV5T PHJs show the lowest (0.08 V). DCV5T devices show steeper tails in the EQE than DTDCPB or HB194 devices, which explains the lower ΔV_{rad}. HB194 PHJs show a broad shoulder in the EQE, which gives rise to the large ΔV_{rad} observed. The ΔV_{nonrad} is highest in HB194 devices (0.45 V), followed by DCV5T/BTIC-H (0.40 V) and DTDCPB devices showing the lowest values (0.29 V). Total voltage losses for these PHJs are summarised in Table 5.1, and fitting details for the EQE extrapolation can be found in Appendix A.7. DCV5T/BTIC-H and DTDCPB/BTIC-H show relatively low total voltage losses (0.81 V and 0.80



(a) (b)

Figure 5.5: Voltage loss breakdown showing the $\Delta V_{J_{SC}}$,ΔV_{rad}, and ΔV_{nonrad} contributions a) split alongside each other and b) stacked below the photovoltaic gap. Individual contributions can be found in Table 5.2. Fitting details can be found in the Appendix A.7.

V). This shows a notable improvement over the voltage losses observed in polymer solar cells ($\approx 0.96V$), where BTIC-H was used with the high performance polymer PCE12 in a solution processed BHJ device [74].

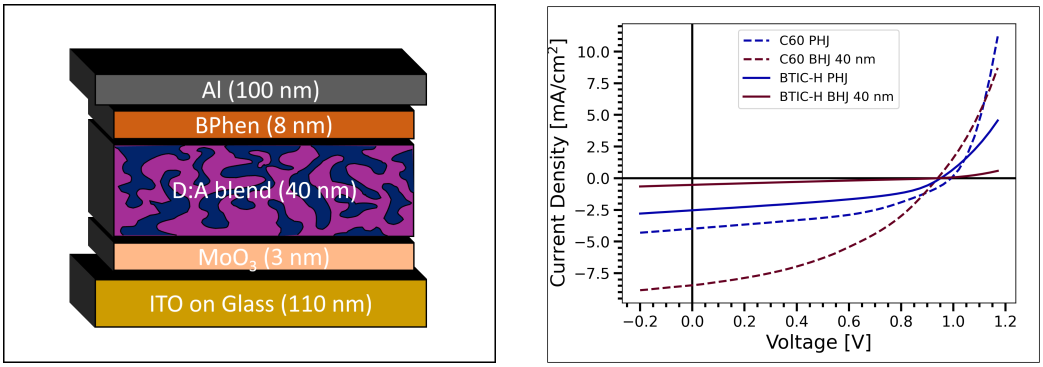
	ΔV_{SC} **(V)**	ΔV_{rad} **(V)**	ΔV_{nonrad} **(V)**
HB194/BTIC-H	0.09	0.11	0.45
DTDCPB/BTIC-H	0.08	0.16	0.29
DCV5T/BTIC-H	0.05	0.08	0.4

Table 5.2: Individual contributions to the voltage loss breakdown shown in Figure 5.5 of BTIC-H PHJ devices (excluding SubNC) showing the $\Delta V_{J_{SC}}$,ΔV_{rad}, and ΔV_{nonrad} contributions.

5.3 BHJ Devices

Given the combination of good J_{SC} (relative to the samples investigated in this thesis) and low voltage losses, the BTIC-H DCV5T system was further explored. BHJ devices were made, and active layers used in these devices used the same nominal thickness of the PHJs, i.e. 40 nm in a 1:1 volumetric ratio. An illustration

of the stack is shown in Figure 5.6a. JV and EQE results are shown in Figure 5.6b and 5.7 respectively, with key metrics summarised in Table 5.3. Also included in these plots are similar results with equivalent C_{60} devices, where the BTIC-H was replaced with C60 in the active layer.



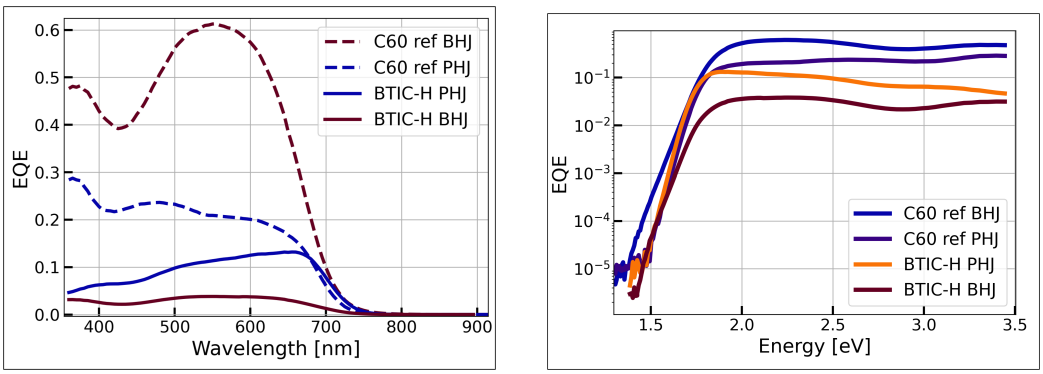
(a) (b)

Figure 5.6: a) Device stack for BHJ devices. BPhen was used as hole blocking layer, and MoO_3 was used as the hole transport layer, nominal thicknesses were ITO (110 nm)/MoO_3 (3 nm)/ DCV5T:BTIC-H (1:1 vol, 40 nm)/ BPhen (8 nm)/ Al (100 nm).b) JV results under illumination of DCV5T/BTIC-H PHJ and DCV5T:BTIC-H BHJ devices and their C60 counterparts.

	BTIC-H PHJ	BTIC-H BHJ	C60 PHJ	C60 BHJ
V_{OC} (V)	0.96 ± 0.01	0.93 ± 0.01	0.99 ± 0.0	0.93 ± 0.0
$J_{SC\ measured}$ (mA/cm^2)	2.43 ± 0.10	0.53 ± 0.01	3.93 ± 0.19	8.20 ± 0.35
Equiv. Sun Intensity (AM1.5G)	0.95	0.95	0.94	0.94
$J_{SC\ corrected}$ (mA/cm^2)	2.55 ± 0.11	0.57 ± 0.01	4.20 ± 0.20	8.77 ± 0.37
FF (%)	41.9 ± 0.3	24.6 ± 0.1	45.2 ± 0.5	41.2 ± 0.6
PCE (%)	1.02 ± 0.04	0.13 ± 0.01	1.75 ± 0.1	3.09 ± 0.12
Voltage Loss (V)	0.81 ± 0.2	0.87 ± 0.2	0.79 ± 0.2	0.93 ± 0.2

Table 5.3: Key device metrics for the DCV5T:BTIC BHJ and DCV5T:C60 BHJ devices, calculated from the $J-V$ and EQE results shown in Figure 5.6b and Figure 5.7 respectively.

DCV5T:BTIC-H BHJs showed V_{OC} of 0.93 V, J_{SC} of 0.53 mA/cm^2, and FF of 25%. The increased interface in a BHJ should ideally result in an increase in short-circuit current because more excitons reach the exciton-splitting interface.



(a) (b)

Figure 5.7: a) EQE results of the same devices shown in Figure 5.6, b) EQE of the same devices, plotted on a logarithmic scale.

However, this is not observed for the DCV5T:BTIC-H BHJs. Two possible reasons for this are that

1. the generation of free charges is impeded compared to the PHJ, e.g. by an energetic barrier that is introduced through orientation [122, 83] or aggregation changes in the molecules upon mixing, or

2. there is an issue with charge collection in the BHJ devices, which may occur due to higher recombination rates in the blend.

Both reasons could also explain the lower FF of $\approx 26\%$ shown in the BHJ JV curves as opposed to the $\approx 42\%$ exhibited in the PHJ JV. It is important to note that the V_{OC} has only slightly dropped, from 0.96 V in the PHJ to 0.93 V in the BHJ. This makes an energetic barrier less likely as the primary loss mechanism to explain the low photocurrent in the BHJ devices, as the impact on the V_{OC} would likely be more severe if energetic barriers were present in the blend. If on the other hand, charge collection is causing a lower FF, this would be mediated by a lower mobility and/or an increase in recombination in the BHJs. OTRACE measurements shown in Figure 5.8 and following the analysis in ref [123] , probe

the faster mobility species and confirm a very low value in the DCV5T:BTIC-H BHJs of 1.3×10^{-6} cm^2/Vs. The likely reason for low mobility is an unfavourable microstructure, which we examine later on.

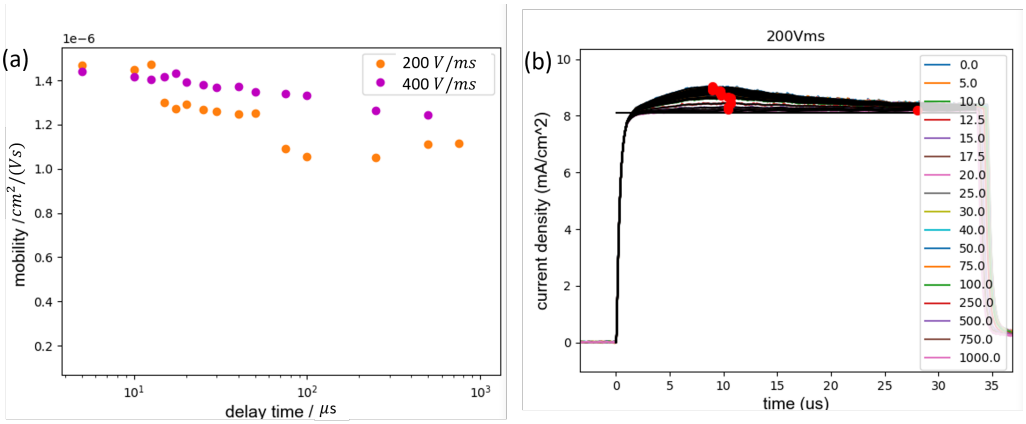
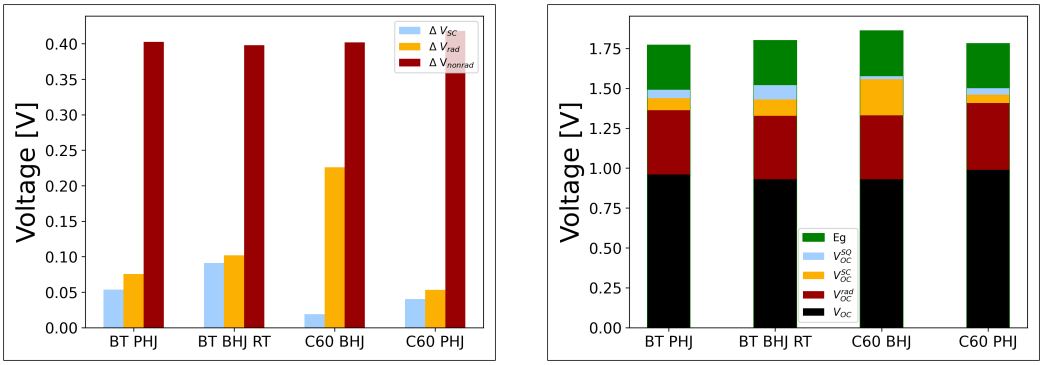


Figure 5.8: OTRACE measurement of the 60nm DCV5T:BTIC-H BHJ. (a) extracted mobilities at two different ramp rates and for several delay times. Results are in good agreement and yield a low mobility of 1.3×10^{-6} cm^2/Vs. (b) Transient current traces for different delay times and a ramp rate of 200V/ms. The black lines smooth the raw data and red dots indicate the automatically extracted maxima used to calculate the mobility. For long delay times the height of the current peak decreases and a maximum cannot be determined. Measurements were taken and processed by Pascal Kaienburg from the University of Oxford.

DCV5T/C_{60} PHJs showcased V_{OC} values of 0.99 V, J_{SC} of 3.93 mA/cm^2, and FF of 45%. DCV5T/C60 PHJs showed better performance across all key metrics than equivalent BTIC-H PHJs, most noticeably in the J_{SC} despite absorbing fewer photons given that the absorption of C_{60} is weaker than that of BTIC-H (refer to Figure 5.1b). In the C_{60} BHJs, the increase in interface area results in a substantially higher J_{SC} of 8.2 mA/cm^2, more than double that observed for a PHJ of the same thickness, a slightly smaller V_{OC} of 0.93 V, and lower FF of 41%. The J_{SC} is further increased in the thicker 60 nm device (Figure 5.8), which is not at all observed in the BTIC-H BHJs. The FF does reduce upon increasing the thickness of the active layer in the C_{60} reference BHJs, which may be caused by higher

charge collection losses at greater thicknesses, but the higher J_{SC} observed still contributes to a higher PCE in the thicker films. It should be noted that in optimised devices DCV5T:C60 BHJs are reported to show similar V_{OC} values (≈ 0.96 V), albeit with much higher J_{SC} ($\approx$ 13 mA/cm^2) and better FF ($\approx 60\%$) [111]. This highlights the impact optimisation can have on the photocurrents of OSCs, but also shows that the value of V_{OC} is mostly impacted by the choice of materials rather than the processing conditions.

Figure 5.9 shows the voltage loss breakdown between C60 and BTIC-H devices in combination with DCV5T, with individual loss contributions shown in Table 5.4. $\Delta V_{J_{SC}}$ for C_{60} devices are lower compared to the BTIC-H devices, reflecting the reduction in J_{SC} seen in the JV. For the C_{60} PHJ devices, ΔV_{rad}, is lower than the BTIC-H PHJ. Interestingly, despite showing far better overall performance than BTIC-H devices, the C60 BHJs show much higher ΔV_{rad}. This is likely due to the fact that the BTIC-H BHJ devices show much lower photocurrents, close to an order of magnitude difference. This makes a fair comparison between the BTIC-H BHJ and the C60 BHJ devices difficult and should be avoided. Both BTIC-H and C60 devices show similar ΔV_{nonrad}. Total voltage losses are displayed in Table 5.3, showing similar voltage losses across both BTIC-H and C60 PHJs, 0.81 and 0.79 respectively, with values within error margins of each other. Despite performing poorly compared to C_{60} BHJs, BTIC-H BHJs show lower voltage losses, 0.87 vs 0.93 V.



(a) (b)

Figure 5.9: Voltage loss breakdown according to detailed balance principle showing $\Delta V_{J_{SC}}$, ΔV_{rad}, and ΔV_{nonrad} contributions, shown a) split up alongside each other and b) stacked with the photovoltaic band gap for ease of reference.

	ΔV_{SC} **(V)**	ΔV_{rad} **(V)**	ΔV_{nonrad} **(V)**
DCV5T/BTIC-H	0.05	0.08	0.4
DCV5T:BTIC-H	0.09	0.1	0.4
DCV5T/C60	0.04	0.05	0.42
DCV5T:C60	0.02	0.23	0.4

Table 5.4: Voltage loss breakdown contributions shown in Figure 5.9 according to detailed balance principle showing $\Delta V_{J_{SC}}$, ΔV_{rad}, and ΔV_{nonrad} contributions.

5.4 Microstructure of DCV5T:BTIC-H blend

Further investigation into the microstructure of the BHJ active layer was prompted by the above results. GIWAXS and AFM measurements were taken on neat (20 nm nominal) and blended (40 nm nominal) films deposited on glass substrates with a 1:1 volumetric ratio to match the active layer in the PHJ and BHJ devices (as shown in Figures 5.2a and 5.6a). Processed images from these measurements are shown in Figure 5.10.

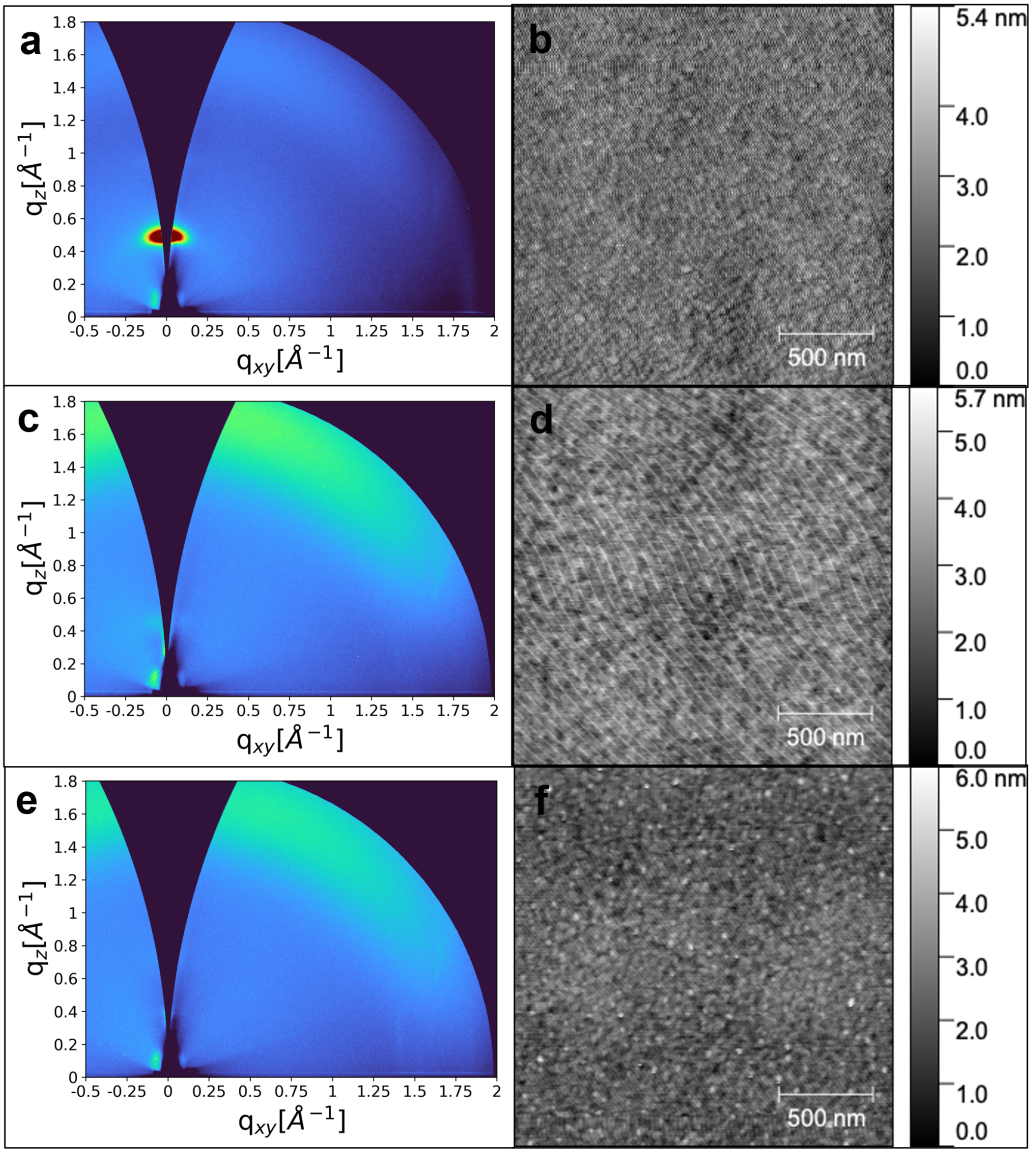


Figure 5.10: GIWAXS images of films deposited on glass substrates held at room temperature of a) neat BTIC-H (20 nm), c) DCV5T:BTIC-H blend (1:1 vol, 40 nm), and e) neat DCV5T (20 nm). AFM images on identical samples shown alongside (b,d,f) with calculated surface roughness of b) 574 ± 108 nm, d) 675 ± 36 nm, f) 594 ± 57 nm .

No clear X-ray scattering is observable for DCV5T at room temperature, however, there is a strong Bragg peak present at $\approx 0.5^{-1}$ for the BTIC-H neat film in the out

of plane direction, indicative of lamellar stacking of the BTIC-H molecules and has been attributed to the dihedral angle in the bithiophene core of the molecule caused by the hexyl side chains [74]. The root-mean-squared (RMS) surface roughness calculated from the AFM images is 574 ± 108 nm for BTIC-H and 594 ± 57 nm for DCV5T. These peaks disappear upon blending, indicating a significant disruption of the stacking order present in the neat film. This could be caused by a strong degree of intermixing between the molecules which create larger amorphous mixed phase regions within the layer. Alternatively, the new blend morphology may still retain large acceptor rich domains like those in the neat film, but these domains might now be amorphous due to interactions with the DCV5T molecules. Since a good FF and efficient collection of charges in a BHJ requires the right degree of phase separation, we believe the former case to be present here. This hypothesis is reinforced by SE results of the blend film which show that the extinction coefficient of the blend is weaker than that of either BTIC-H or DCV5T, implying that there is some molecular interaction between the species which effects the optical transition dipoles of the molecules, for e.g. causing orientation changes which reduce the overall absorption of the blend. The surface roughness of the blend film is 675 ± 36 nm, which is quite similar to both of the neat films, which would be expected of a strongly intermixed blend film with little phase segregation.

Similar thin film samples were deposited on heated substrates held at 80°C and the results of GIWAXS and AFM measurements of these samples are shown in Figure 5.11. According to the GIWAXS image of the BTIC-H sample deposited at 80°C, a Bragg peak ≈ 1.8 Å^{-1} appears in-plane, indicating $\pi - \pi$ stacking in a plane parallel to the substrate, and upon blending the HT sample shows more pronounced ordering than the RT blend, yet still weak compared to the neat BTIC-H images. Nonetheless, in the blend films it is still instructive to note the improvement in

crystallinity with heating, shown from the intensifying of the out-of-plane peak at ≈ 0.5 Å^{-1} indicative of stronger lamellar stacking of the BTIC-H molecules, and the increase in $\pi - \pi$ stacking with an intensifying of the in-plane feature at ≈ 1.8 Å^{-1}. The DCV5T sample also shows stronger scattering with a visible Bragg peak occurring in the out-of-plane direction at ≈ 0.8 Å^{-1}. AFM images both show increased RMS surface roughness values as well, namely 709 ± 94 nm, 822 ± 44 nm, and 672 ± 37 nm for the BTIC-H, blend, and DCV5T film respectively. This supports the idea from the GIWAXS images that heating leads to more crystalline structure, with the RT blend in particular having high levels of intermixing. If a film is highly amorphous, it is likely to be smoother, and vice versa as the film becomes more crystalline the surface can become less smooth. Following our earlier reasoning that this crystallinity is tracking, to some extent, the mixing in the blends, it stands to reason that the HT blend samples show less mixing, i.e., phase segregation increases upon depositing the film on a heated substrate. This is a phenomenon which has been observed for similar systems in the literature [124].

A second set of BHJ devices were made to assess the impact of substrate heating on device performance, with the stacks used being identical to those shown in Figure 5.6a. Substrates of these high temperature (HT) devices were held at 80°C during the deposition of the active layer only. The JV results of these devices is shown in Figure 5.12a. The active layer in two of the substrates were varied to 50 nm (substrates B and D), with the other two matching the room temperature active layer thickness of 40 nm (substrates A and C), with only the J_{SC} being noticeably affected. Also shown in Figure 5.12b are the results from different pixels on the device substrates, which indicate a spread in the overall JV curves most likely due to inhomogeneity across the substrate introduced through the deposition. While minor gains were observed overall in the J_{SC} of all HT devices compared to the

room temperature devices, there is still a stark gap in photocurrents between C_{60} and BTIC-H BHJs. Key metrics from Figure 5.12 are shown alongside the room temperature BHJ JV results in Table 5.5.

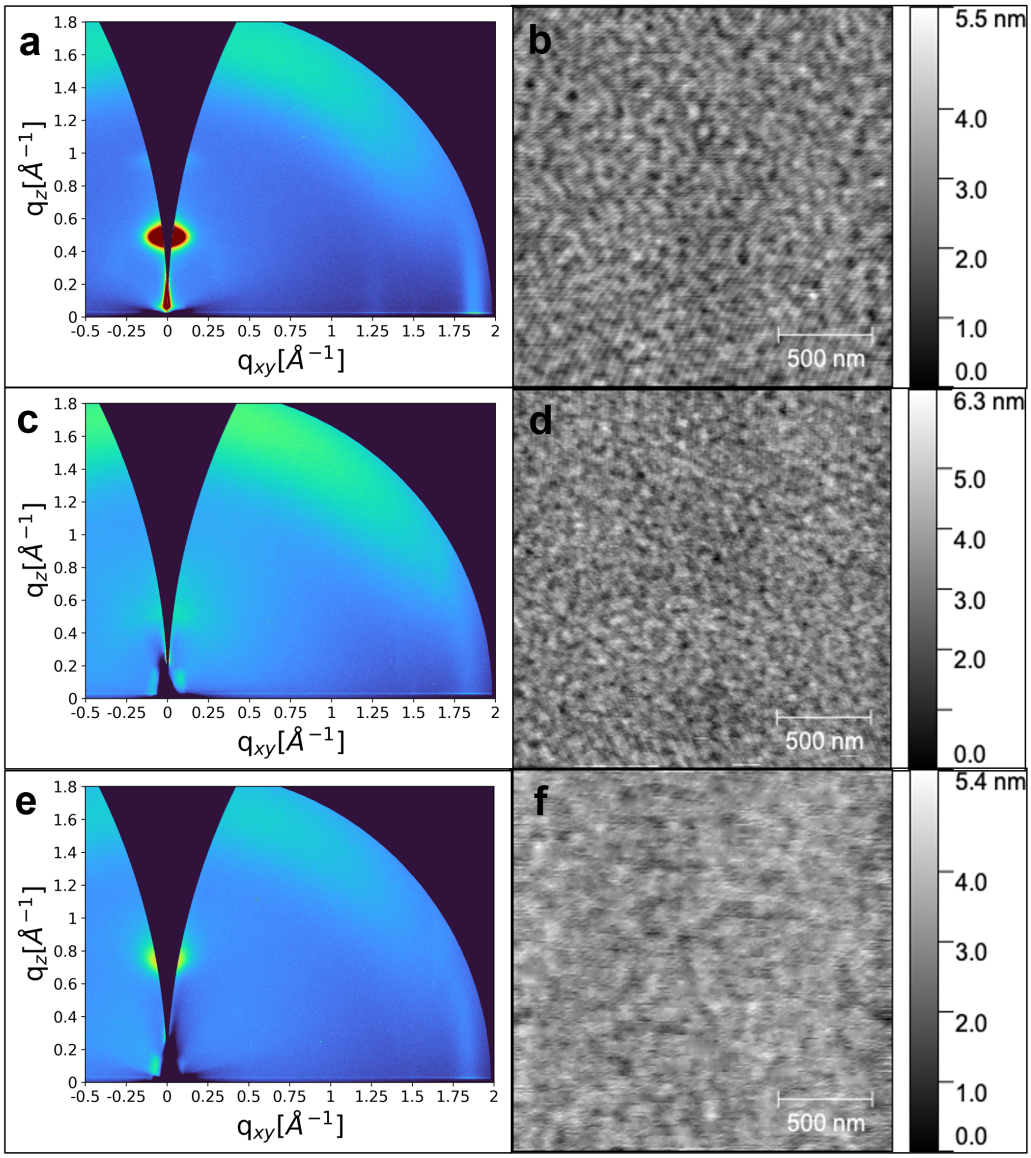
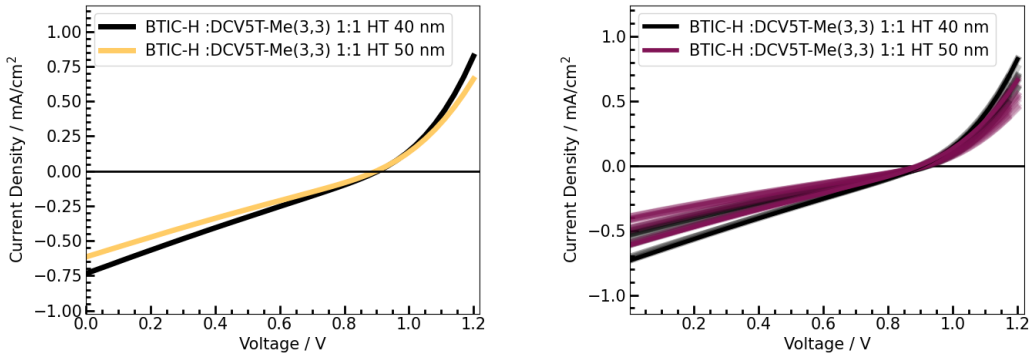


Figure 5.11: GIWAXS images of films deposited on glass substrates held at 80°C of a) neat BTIC-H (20 nm), c) DCV5T:BTIC-H blend (1:1 vol, 40 nm), and e) neat DCV5T (20 nm). AFM images on identical samples shown alongside (b,d,f).



(a) (b)

Figure 5.12: $J-V$ measurements of DCV5T:BTIC-H (1:1 vol ratio nominally) BHJ devices evaporated onto substrates held at $80°$C. Data shown for a) champion devices with 40 nm (black) and 50 nm (yellow) active layers and b) a summary of all device data of the 40 nm (black) and 50 nm (purple) samples, clearly showing a noticeable spread that is likely due to slight inhomogeneities in the deposited thicknesses across the substrate.

	BHJ HT 40 nm	BHJ HT 50 nm	BHJ RT 40 nm
V_{OC} (V)	0.92 ± 0.02	0.90 ± 0.01	0.93 ± 0.01
$J_{SC\ measured}$ (mA/cm^2)	0.58 ± 0.08	0.47 ± 0.08	0.53 ± 0.01
FF (%)	24.2 ± 0.01	24.8 ± 0.1	24.6 ± 0.1
PCE (%)	0.13 ± 0.02	0.10 ± 0.02	0.13 ± 0.01

Table 5.5: Key mean device metrics for the DCV5T:BTIC BHJ HT and DCV5T:C60 BHJ devices, calculated from the $J-V$ results shown in Figure 5.12

5.5 Summary and Conclusions

Despite the low PCE ($\approx 1\%$ for DCV5T/BTIC-H and SubNC/BTIC-H PHJs), the results have nevertheless shown encouraging performance of evaporated organic solar cells using the non-fullerene acceptor BTIC-H, originally developed for solution processing. The low molecular weight and relatively simple molecular structure of BTIC-H, giving it an advantage over many NFAs in terms of

synthetic complexity, makes it feasible for evaporation. Despite the molecule not being optimised for evaporation, we achieve high open-circuit voltage of 0.96 V and modest short circuit currents of 2.43 mA/cm^2 when used with DCV5T as donor in a planar heterojunction device. Furthermore, voltage losses of 0.81 V, comparable to equivalent fullerene devices (0.79 V) were achieved for the DCV5T planar heterojunctions. Bulk heterojunctions of DCV5T:BTIC-H showed similar open circuit voltages (0.93 V) but poor short circuit currents (0.53 mA/cm^2) which was likely due to a poor morphology of the blend layer inhibiting efficient charge collection.

By using a combination of PHJ and BHJ structures to investigate BTIC-H as VTE compatible NFA we were able to begin studying the D/A interface energetics and their effect on photocurrent generation and voltage loss separately from morphological effects in mixed blends. This screening procedure helps to identify suitable donors and was enabled by the ease of sequential deposition in VTE. While these results are certainly encouraging, attaining higher PCE and doing better on the trade-offs encountered in this work is key for the success of evaporable NFAs which, once identified, hold great promise for commercial OPV applications in the near future.

By using this study as a test-bed for investigating evaporable NFAs the following workflow is proposed for efficient screening of new candidates, which is also illustrated in Figure 5.13:

1. Evaporation test in a suitable chamber where films are deposited on Si, SiO2, ITO and glass substrates
2. Basic material characterisation of the optical constants and energy levels using SE and APS.
3. Based on the optical and energetic measurements, a suitable range of donor

molecules should be chosen with different energetic offsets and absorption bands. If absorption is poor (extinction coefficients < 0.4) or if HOMO values are not suitable then a new iteration of the molecule should be considered

4. Using these donors, PHJ devices should be made with sufficiently thin layers (< 20 nm) to ensure adequate film coverage but also to mitigate charge generation losses to due to potential poor mobility. JV and EQE measurements should be made on these devices.

5. Donors which yield promising results (suggested starting values are$J_{SC} > 1$ mA/cm^2, $V_{OC} > 0.8$) should be explored further in BHJ layouts, with JV and EQE measurements performed again.

6. Promising devices (similar metrics as above) can then be shortlisted for further optimisation studies.

The values of the metrics listed above (extinction coefficient, J_{SC} , V_{OC}) are suggestions based on the small sample size on molecules studied in this chapter and will very likely be adjusted as more molecules enter the workflow. It is probably better in the early stages of screening, where material availability is likely to be a hindrance, to be less strict with the elimination criteria.

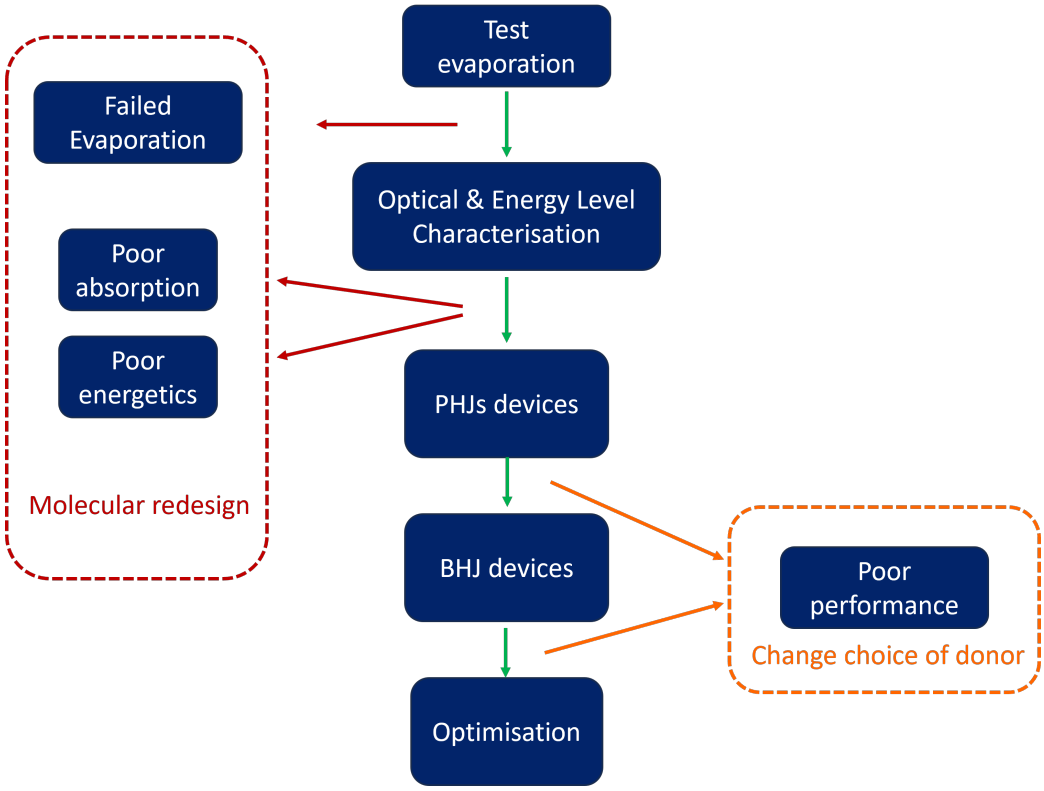


Figure 5.13: Proposed screening workflow for investigations on evaporable NFA candidate molecules.

6 | Using NEXAFS and SE to characterise orientation in evaporated small molecule thin films

6.1 Introduction

The orientation of molecules plays a crucial role in a number of processes in organic semiconductor thin films, including a charge transport properties, morphological packing motifs, absorption, energetic landscapes at the surface, to name a few. There are a number of techniques that can yield a value of the molecular orientation however it is not trivial to understand how these values compare with each other or indeed what specific orientation is being detailed. This is largely because the term molecular orientation is ambiguous, and can refer to many different geometries relevant to an organic molecule. In this work we assume the geometry of molecule is similar to a rectangular disk, i.e. we consider the plane spanned by the backbone of the molecule. We discuss the orientation of the long molecular axis, i.e. the angle between conjugated backbone of the molecule and the substrate normal as illustrated in Figure 6.1a, and the orientation of the short molecular axis, i.e. the angle between the molecular face and the substrate normal, illustrated in Figure 6.1b. Often the optical transition dipole moment (μ_{TDM}), which is usually determined by time-dependent density functional theory calculations, of a linearly conjugated molecule can be used as a proxy for the direction of the molecular backbone [19, 76]. There will be some constant (for each different molecule), minor offset between the μ_{TDM} vector and the backbone of the molecule but this is assumed to be negligible. Similarly, the orbital vectors of the aromatic rings, and in some cases other functional groups, in such a molecule can

be used as a proxy for the orientation of the molecular face.

We use two techniques to analyse these orientations, Near Edge X-ray Absorption Fine Structure (NEXAFS) spectroscopy for the orbital structures and Spectroscopic Ellipsometry (SE) for the optical transition dipole moments, and in so doing develop a more comprehensive image of molecular orientation as illustrated in Figure 6.1c. To avoid confusion we will denote the orientation of the molecular backbone calculated from SE using Equation 3.4 with the order parameter S_μ:

- $S_\mu = -0.5$ indicates that μ_{TDM} is perpendicular to the substrate normal.
- $S_\mu = 0$ indicates either a random orientation distribution (i.e. no preferential orientation) or that μ_{TDM} is $54.7°$ away from the substrate normal.
- $S_\mu = 1$ indicates that μ_{TDM} is parallel to the substrate normal.

Molecular facial orientations calculated from the NEXAFS data will be given in angles between the orbital vector and the substrate normal. These orbital tilt angles are denoted as α:

- $\alpha = 90°$ indicates that the mean molecular arrangement is lying perfectly edge on, i.e. the molecular face is perpendicular to the substrate plane.
- $\alpha = 54.7°$ indicates that there is no conclusive preferential orientation of the molecular face, i.e. there are many possible orientation distributions which may average out to a mean orientation of $54.7°$, including a random distribution with no preferential orientation.
- $\alpha = 0°$ indicates that the mean molecular arrangement is lying perfectly face-on, i.e. the molecular face is parallel to the substrate plane.

Grazing Incidence Wide Angle X-ray Scattering (GIWAXS) images will also be used to supplement the findings qualitatively by looking at changes in scattering

intensity as as function of material and deposition temperature.

In this chapter we will look at the orientation analysis for several popular evaporable small molecules, including a6T, DTDCPB, HB194. a6T has been characterised extensively in the literature and will serve as an excellent benchmark for the analysis. While DTDCPB and HB194 have seen much use in small molecule evaporated devices, their microstructure has not been as extensively characterised in evaporated thin films. We will also look at the impact of substrate annealing during deposition on the orientation of these materials. These samples were deposited in the National Thin Film Cluster Facility and were deposited on various substrates, including Si wafers with a native oxide ($\approx$ 3 nm of SiO_2), Si wafers with a thermal oxide of 150 nm SiO_2, and glass substrates. All samples were nominally 80 nm thick and included a deposited 3 nm MoO_3 underlayer. The reason for the underlayer was to make samples more representative of device working conditions, and the active layers are often deposited on this MoO_3 layer, as well as to remove templating effects from the different substrates. Dr Jin Yao and Zhenlong Li from the University of Oxford assisted with the sample fabrication.

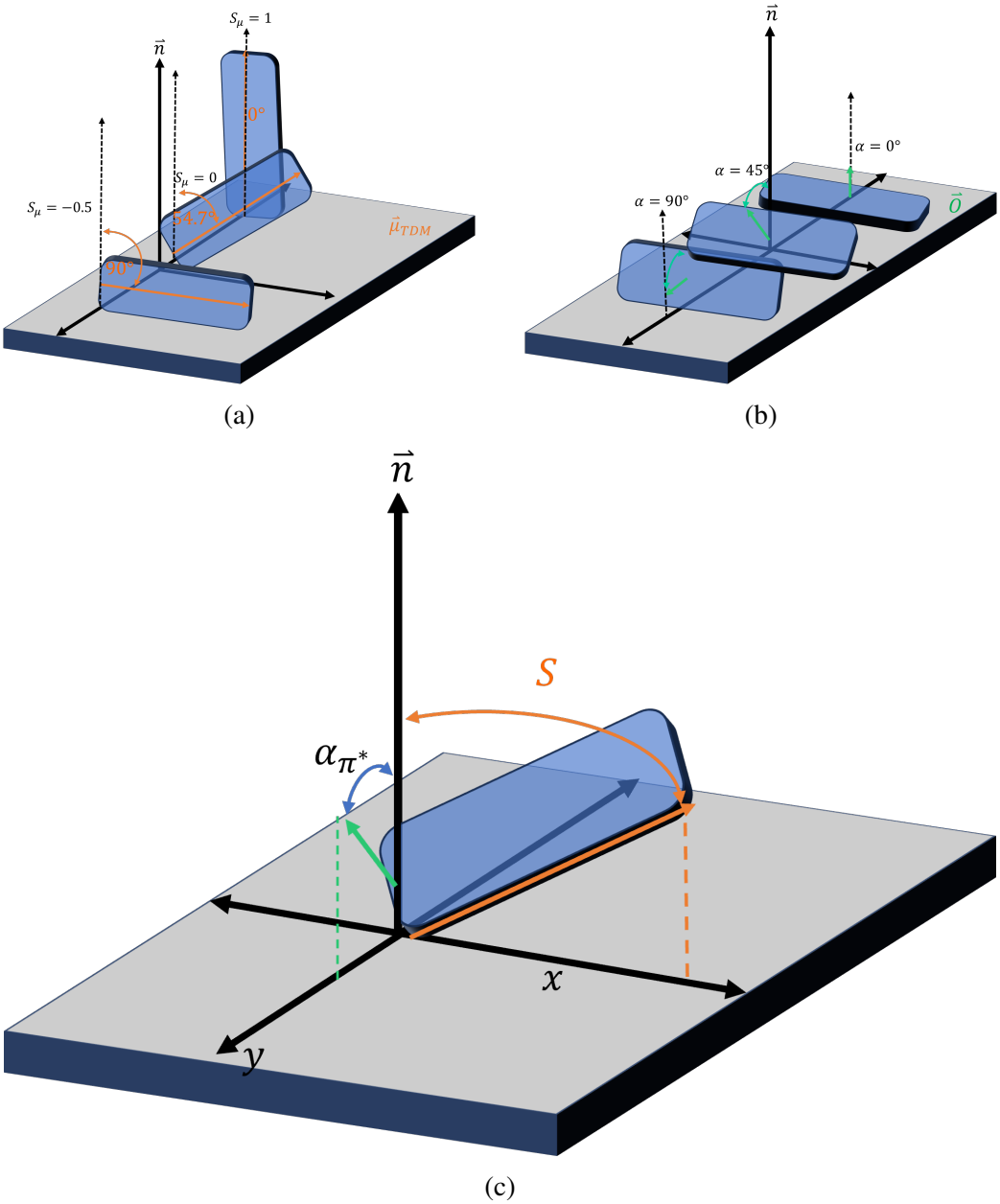


Figure 6.1: Co-ordinate system describing the geometry of different orientation angles (0°, 45°, 90°) with respect to the surface normal $\vec{n}$ of a molecule (shown as a blue rectangle), showing the orientation of a) the optical transition dipole moment $\vec{\mu}_{TDM}$ along the molecular backbone at three different angles , b) the orbital vector $\vec{O}$ (which can also be the normal of an orbital plane for planar orbitals) which describes the transition from the 1s orbital to an excited state (usually the π^* or σ^* orbitals), and c) how both a) and b) can both play a role in the orientation of a molecule.

6.2 NEXAFS Results

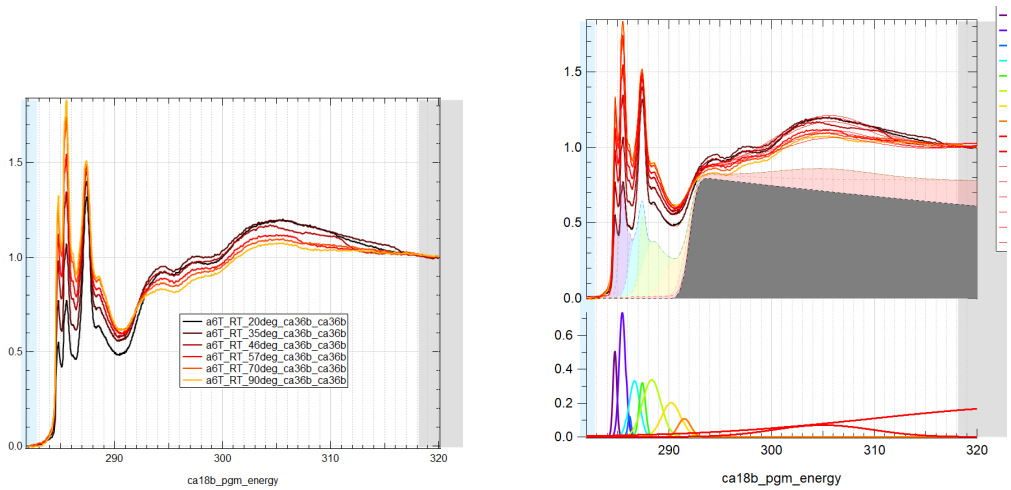
NEXAFS measurements were taken at the B07 beamline at Diamond Light Source, experiment no. SI30197-1. Zhenlong Li from the University of Oxford assisted with data acquisition at the beamtime. Data was taken on thin films deposited on Si substrates with 3 nm MoO_3 underlayer. Conductive clips were used to attach to the sample surface to ensure sufficient conductivity during the NEXAFS measurements. For each material investigated measurements were taken on thin films deposited on substrates held at room temperature and on samples held at an elevated temperature, 80°C for DTDCPB and HB194 and 110°C for α-6T. Further details of the fitting of the NEXAFS data in this chapter can be found in Appendix A.8.

6.2.1 a6T

NEXAFS data for the a6T samples deposited at room temperature (RT) taken at various angles of incidence are shown in Figure 6.2a. Distinct narrow peaks are observed in the < 290 eV range arising from both π^* and σ^* resonances, and broader peaks are observed in the > 290 eV range, arising from σ^* resonances. The peaks in this first energy range, i.e. < 290 eV, are what we will focus on fitting given that these resonances exhibit strong signal-to-noise ratios. The C 1s $\rightarrow \sigma^*$ resonances above 290 eV arise from a combination of the $C = C$ and $C - H$ bonds, but have much lower signal-to-noise ratios when compared to the resonances below 290 eV, and are positioned directly on top of the NEXAFS edge, making fits less certain. Fits over the entire region are shown in Figure 6.2b.

Figure 6.3 show fits over the < 290 eV region. The peaks at 284.78 and 285.5 eV are typical of $C = C$ π^* resonances in polythiophene systems [125]. The peak

at 287.42 eV likely corresponds to the C 1s $\rightarrow \sigma^* \; C-S$ transition [126, 125]. The peak at 288.34 eV likely corresponds to the C 1s $\rightarrow \sigma^* \; C-H$ transition [126, 125]. The peaks in between could be additional resonances from any of the previously mentioned transitions, as well as the C 1s $\rightarrow \sigma^* \; C=C$ transition which is typically also found above the NEXAFS edge.



(a) (b)

Figure 6.2: a) Processed NEXAFS scans at multiple angles (shown in different colours) of a6T deposited at room temperature. b) Fits of a) with several Gaussian oscillators and the NEXAFS edge, with the fitted data shown in thin red lines, and individual Gaussian peaks shown below for the median angle in the scan. The shaded region in the scan indicated the cumulative area from the fitted peaks, and is scaled down so as to increase readability of the data.

Assuming a vector orbital for the π^* transitions and a planar orbital for the σ^* transitions we can fit the areas of the identified peaks using Equation 3.5 to determine the orbital tilts, shown in Figure 6.4. Given that the two subsequent peaks at 286.16 and 286.65 eV show almost identical angular dependence it is likely that these resonances are also due to the C 1s $\rightarrow \pi^* \; C=C$ transition, however these were not included in the calculation shown in Figure 6.4. Fits of the $C=C \; \pi^*$ resonance yield an orbital tilt angle of $\alpha_\pi = 67.73 \pm 0.11°$ from the substrate

normal. Fits of the σ^* resonances show an orbital tilt of $\alpha_\sigma = 58.52 \pm 0.33°$ and $\alpha_\sigma = 44.10 \pm 0.18°$ for the $C - S$ and $C - H$ σ^* orbital planes, respectively. It is interesting that there is a stark discrepancy in the σ^* orbital tilts as they should be in more agreement given that both $C - S$ and $C - H$ orbitals are expected to span the plane of the molecule. These results suggest that this is not the case and that they in face span different planes with an angular offset $\approx 10°$. It may also be possible that the fits using the σ^* transitions are not reliable due to their closer proximity to the NEXAFS edge, as discussed in Chapter 3.

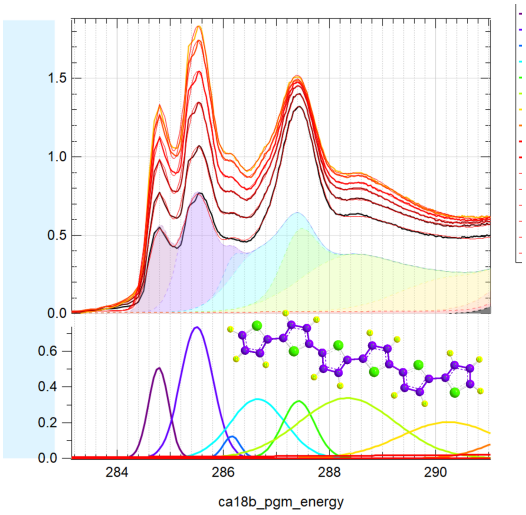


Figure 6.3: Zoomed in image of the fits of the NEXAFS results shown in Figure 6.2 with several Gaussian oscillators and the NEXAFS edge, with the fitted data shown in thin red lines, and individual Gaussian peaks shown below for the median angle in the scan. The shaded region in the scan indicated the cumulative area from the fitted peaks, and is scaled down so as to increase readability of the data. Also shown in the α-6T molecule with moieties shaded to represent contributions from the NEXAFS data: C atoms shaded in purple to reflect the $C = C$ resonances, S atoms in green to reflect the $C - S$ resonance, and H atoms in yellow to reflect the $C - H$ resonances.

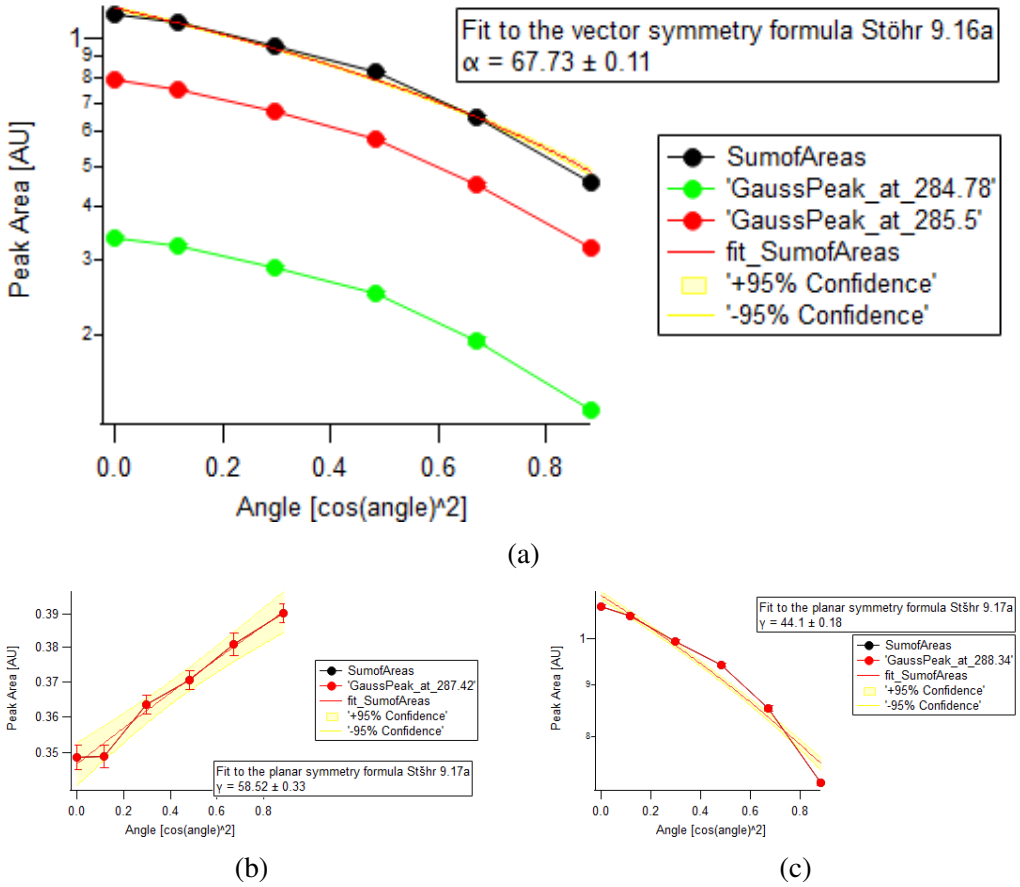
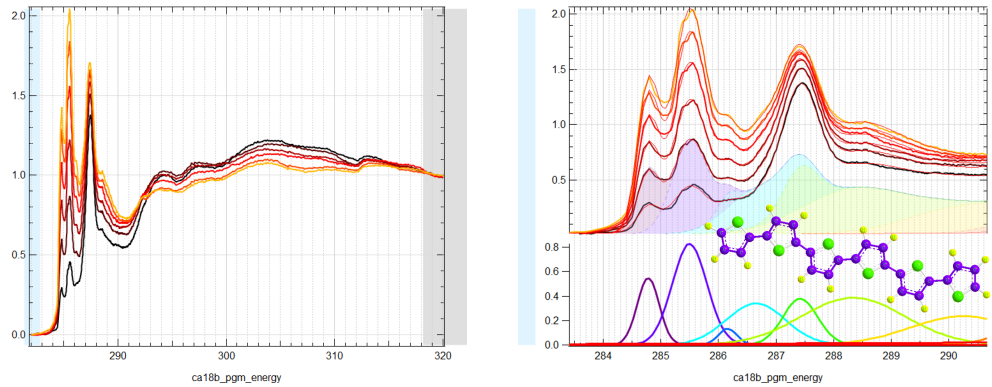


Figure 6.4: Plots of the areas under the peaks from data for a6T deposited on substrate held at room temperature, shown in Figure 6.3, at various angles associated with the a) $C = C\ \pi^*$ transitions, b) $C - S\ \sigma^*$ transitions, and c) $C - H\ \sigma^*$ transitions. Also shown is the cumulative area and the associated fit to that using Equation 3.5 for a) and the planar orbital equation from ref [80] for b) and c).

Similar analysis was carried out on similar samples where a6T was deposited on substrates held at 110 °C. The NEXAFS data measured from the higher temperature (HT) sample as well as fits of the pre-edge of the data is shown in Figure 6.5. Included in the inset of Figure 6.5b is an image of the structure, with the chemical moieties colour coded to match their representative fitted peaks.

Fits of the orbital tilt angle for the same resonances as those fitted in for the a6T



(a) (b)

Figure 6.5: a) Processed NEXAFS scans at multiple angles (shown in different colours) of a6T deposited on a substrate held at 110 °C. b) Fits of a), zoomed in to the pre-edge region, with several Gaussian oscillators and the NEXAFS edge, with the fitted data shown in thin red lines, and individual Gaussian peaks shown below for the median angle in the scan. The shaded region in the scan indicated the cumulative area from the fitted peaks, and is scaled down so as to increase readability of the data. Also shown in the α-6T molecule with moieties shaded to represent contributions from the NEXAFS data: C atoms shaded in purple to reflect the $C = C$ resonances, S atoms in green to reflect the $C - S$ resonance, and H atoms in yellow to reflect the $C - H$ resonances.

RT sample in Figure 6.4 are shown for the a6T HT sample in Figure 6.6. $C = C$ π^* orbitals show a tilt of $77.25 \pm 0.28°$ with respect to the substrate normal, which is even closer to an edge-on orientation than in the RT samples. This suggests that the MoO_3 underlayer is weakly interacting with the a6T molecules and that the Van der Waals bonds between a6T neighbours is strongly preferred, and upon supplying additional thermal energy to the system through substrate heating during the deposition this interaction is favoured even further. Fits of the σ^* $C - S$ and $C - H$ resonances yield orbital tilt angles of $56.51 \pm 0.36°$ and $41.68 \pm 0.23°$ respectively, showing little difference from the RT samples, suggesting that this interaction is independent of the substrate heating. One possibility is that perhaps this orbital tilt is related to the packing between a6T neighbouring molecules rather than the facial orientation on the MoO_3 underlayer.

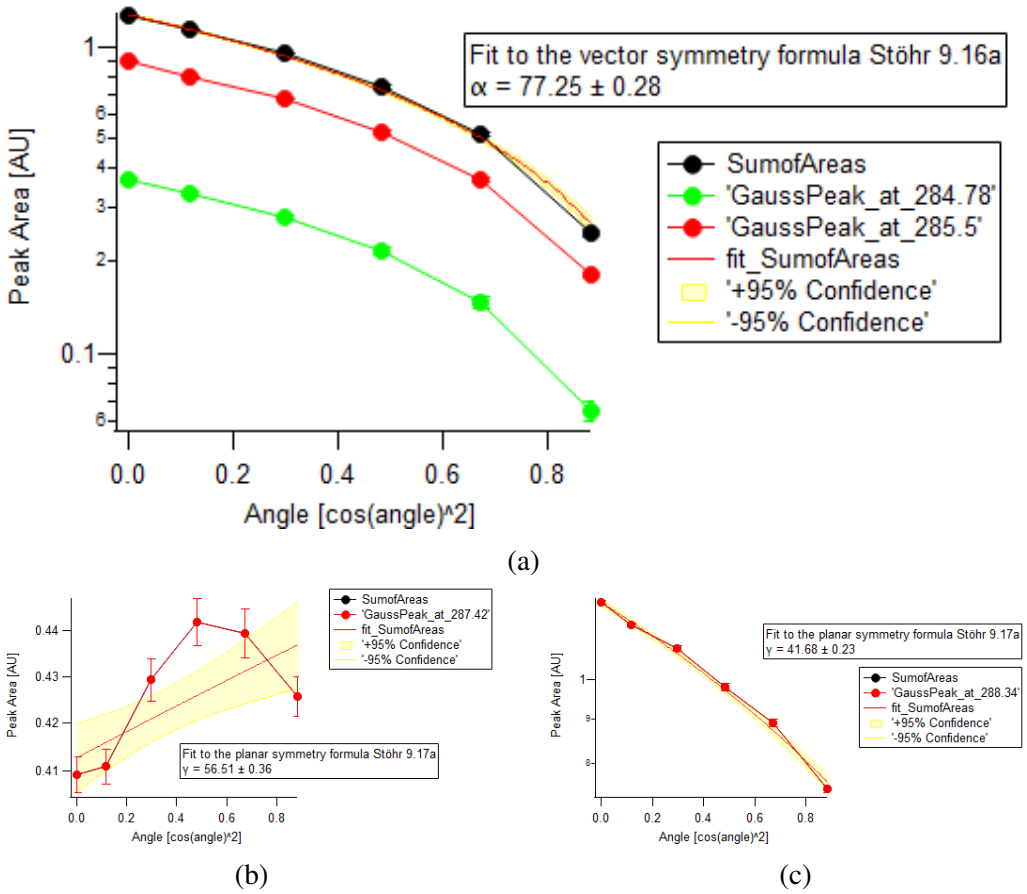
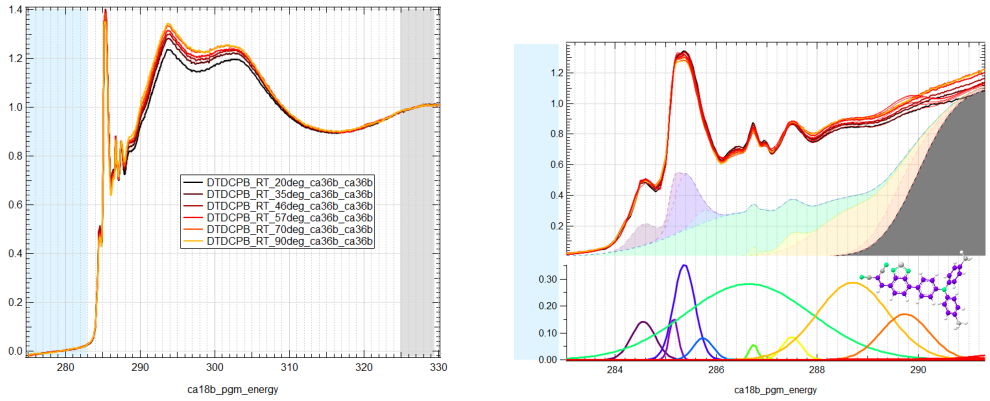


Figure 6.6: Plots of the areas under selected peaks from data of a6T deposited on substrates held at 110 °C, as shown in Figure 6.5 at various angles associated with the a) $C = C\ \pi^*$ transitions, b) $C - S\ \sigma^*$ transitions, and c) $C - H\ \sigma^*$ transitions. Also shown is the cumulative area and the associated fit to that using Equation 3.5 for a) and the planar orbital equation from ref [80] for b) and c).

6.2.2 DTDCPB

NEXAFS data for DTDCPB samples deposited at RT are shown in Figure 6.7a. Little to no angular dependence is observed in the data. This data was fitted with Gaussian oscillators as shown in Figure 6.7b. The first two peaks in the data at 284.6 eV and 285.2 eV are similar to what has been observed in other molecules, and have been attributed to the $C = C$ π^* resonance. The three peaks between 286.2 eV and 287.2 eV are likely due to the $C - N$, $C = N$ [127], and $C \equiv N$ π^* resonances and in particular the second two peaks have been observed in molecules with the dicyanovinylene moiety, i.e. containing $C \equiv N$ bonds, for example these peaks are also observed at almost identical energies in the NEXAFS data for BTIC-H shown in Figure 4.17b. Further peaks beyond this are most likely due to σ^* resonances arising from $C - H$ bonds.



(a) (b)

Figure 6.7: a) Processed NEXAFS scans at multiple angles (shown in different colours) of DTDCPB deposited at room temperature. b) Fits of a), zoomed in to the pre-edge region, with several Gaussian oscillators and the NEXAFS edge, with the fitted data shown in thin red lines, and individual Gaussian peaks shown below for the median angle in the scan. The shaded region in the scan indicated the cumulative area from the fitted peaks, and is scaled down so as to increase readability of the data. Also shown in the DTDCPB molecule with moieties shaded to represent contributions from the NEXAFS data: C atoms shaded in purple to reflect the $C = C$ resonances, N atoms in green to reflect the $C - N, C = N, C \equiv N$ resonances, and the remaining atoms without a specific colour as these resonances were not assigned with confidence.

Using Equation 3.5, the areas under the π^* peaks was fitted to determine orbital tilts and the results of these fits are shown in Figure 6.8. Results are consistent with a random distribution, showing an orbital tilt angle of $54.53 \pm 0.08°$ which is very close to the magic angle of $54.7°$.

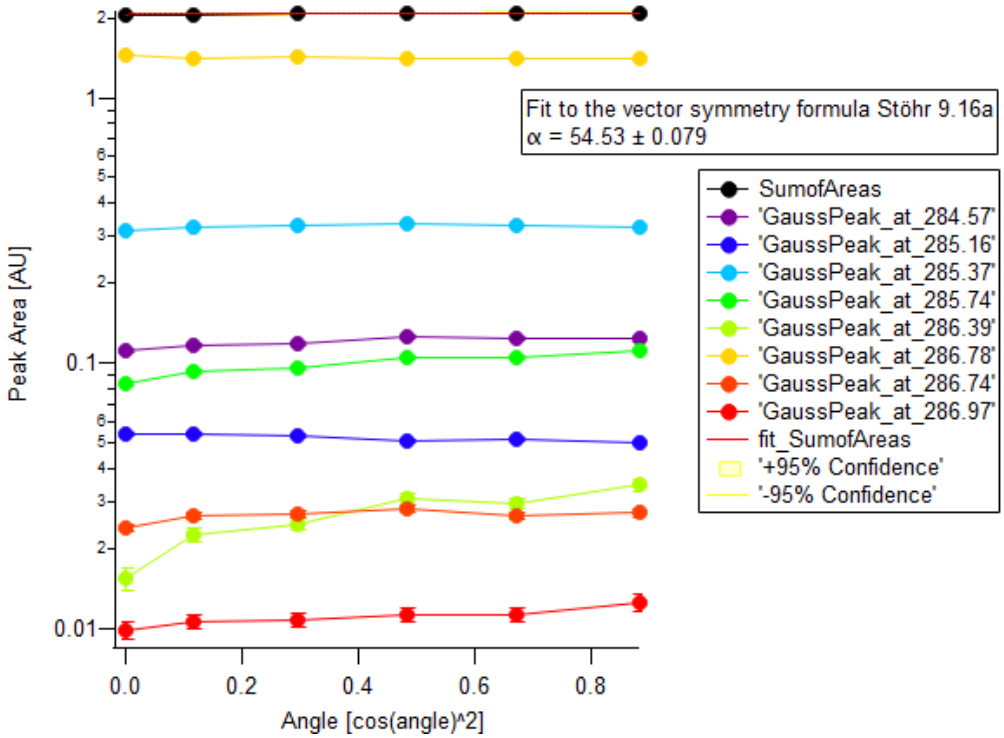
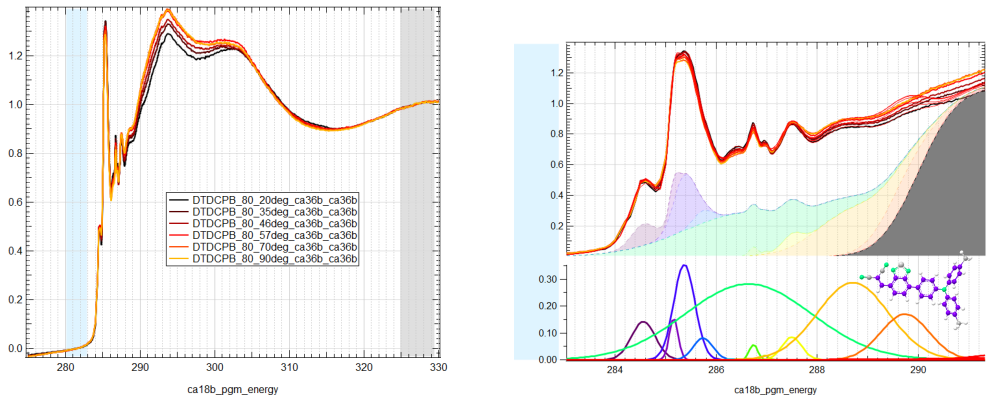


Figure 6.8: Plots of the areas under selected peaks from data for DTDCPB deposited on substrates held at room temperature, shown in Figure 6.7 at various angles associated with the π^* transitions. Also shown is the cumulative area and the associated fit to that using Equation 3.5.

NEXAFS data for DTDCPB samples deposited at 80°C are shown in Figure 6.9a. Similarly to the RT data in Figure 6.9, little to no angular dependence is observed in the data. This data was fitted with Gaussian oscillators as shown in Figure 6.9b.



(a) (b)

Figure 6.9: a) Processed NEXAFS scans at multiple angles (shown in different colours) of DTDCPB deposited at 80 °C. b) Fits of a), zoomed in to the pre-edge region, with several Gaussian oscillators and the NEXAFS edge, with the fitted data shown in thin red lines, and individual Gaussian peaks shown below for the median angle in the scan. The shaded region in the scan indicated the cumulative area from the fitted peaks, and is scaled down so as to increase readability of the data. Also shown in the DTDCPB molecule with moieties shaded to represent contributions from the NEXAFS data: C atoms shaded in purple to reflect the $C = C$ resonances, N atoms in green to reflect the $C = N, C \equiv N$ resonances, and the remaining atoms without a specific colour as these resonances were not assigned with confidence.

Using Equation 3.5, the areas under the π^* peaks was fitted to determine orbital tilts and the results of these fits are shown in Figure 6.10. Results are consistent with a random distribution, showing an orbital tilt angle of $54.56 \pm 0.17°$, similar to what was observed in the RT samples. These findings suggest that the facial orientation of DTDCPB is likely already at an energetic minimum at room temperature, and to tune the facial orientation, with substrate heating at least, temperatures higher that $80°$C will need to be investigated.

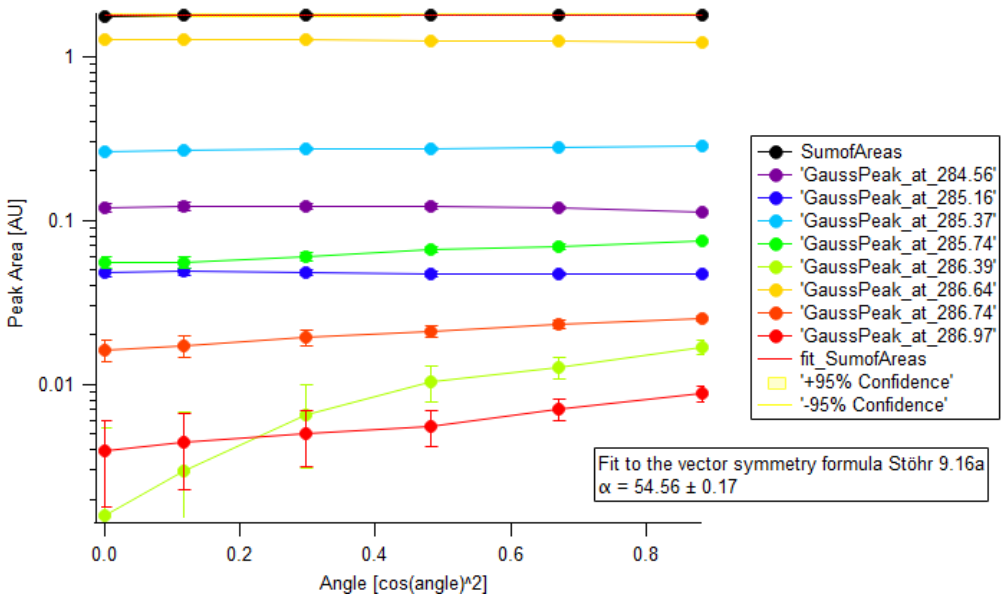
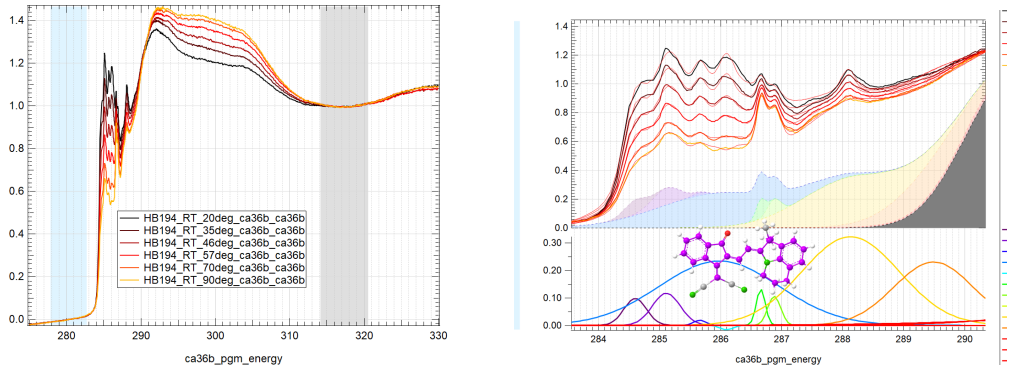


Figure 6.10: Plots of the areas under selected peaks from data in Figure 6.9 for DTDCPB deposited on substrates held at 80°C at various angles associated with the π^* transitions. Also shown is the cumulative area and the associated fit to that using Equation 3.5.

6.2.3 HB194

NEXAFS data for HB194 samples deposited at RT are shown in Figure 6.11a. These data was fitted with Gaussian oscillators as shown in Figure 6.11b. Using Equation 3.5, the areas under these peaks was fitted to determine orbital tilts and the results of these fits are shown in Figure 6.12. The first series of resonances < 286 eV are likely C 1s $\rightarrow \pi^*$ $C = C$ resonances from the acceptor and donor units [128, 129] and show an orbital tilt with respect to the substrate normal of $44.71 \pm 0.39°$. The doublet peak at 286.66 and 286.88 are most likely due to $C \equiv N$ π^* resonances, given that other molecules in this study with $C \equiv N$ bonds also show this distinct doublet, and show an orbital tilt angle of $73 \pm 3°$, implying that these end groups lie more edge-on than the backbone of the molecule. The uncertainty in this fit is much larger than previous calculations, and is due to the

relative weakness of the oscillators in the fit. Finally, there are two broad peaks at 288.13 eV and 289.49 eV, and one low intensity peak at 288.1 eV which is buried by these two broad peaks which is likely due to the $C = O$ π^* resonance [128, 129]. The low intensity peak is probably from the $C = O$ π^* (especially given the relative proportion of O atoms in the HB194 molecule) and is likely superimposed with the much broader σ^* resonance from the previously mentioned two peaks, making fitting less reliable. If three oscillators in this region are used for the fit, the calculation yields an orbital tilt of $53.01 \pm 0.22°$, which could also imply a random distribution given the magic angle value of $54.7°$. If, however, the narrower, less intense resonance that could be due to the $C = O$ is used solely for the orbital tilt calculation, a tilt of $23.1 \pm 10°$ is calculated, with the relatively large uncertainty due to the fact that the resonance is even weaker than those observed for the $C \equiv N$ resonances. Fitting the remaining two peak areas with the equation for σ^* resonances instead [80] we calculate a orbital tilt of $57.87 \pm 0.46°$, which could also be a close to random distribution of orientations of the molecule in this axis and may be arising from the $C - C$ or $C - H$ bonds.



(a) (b)

Figure 6.11: a) Processed NEXAFS scans at multiple angles (shown in different colours) of HB194 deposited at room temperature. b) Fits of a), zoomed in to the pre-edge region, with several Gaussian oscillators and the NEXAFS edge, with the fitted data shown in thin red lines, and individual Gaussian peaks shown below for the median angle in the scan. The shaded region in the scan indicated the cumulative area from the fitted peaks, and is scaled down so as to increase readability of the data. Also shown in the HB194 molecule with moieties shaded to represent contributions from the NEXAFS data: C atoms shaded in purple to reflect the $C = C$ resonances, N atoms in green to reflect the $C \equiv N$ resonances, O atom shaded in red, and the remaining atoms without a specific colour as these resonances were not assigned with confidence.

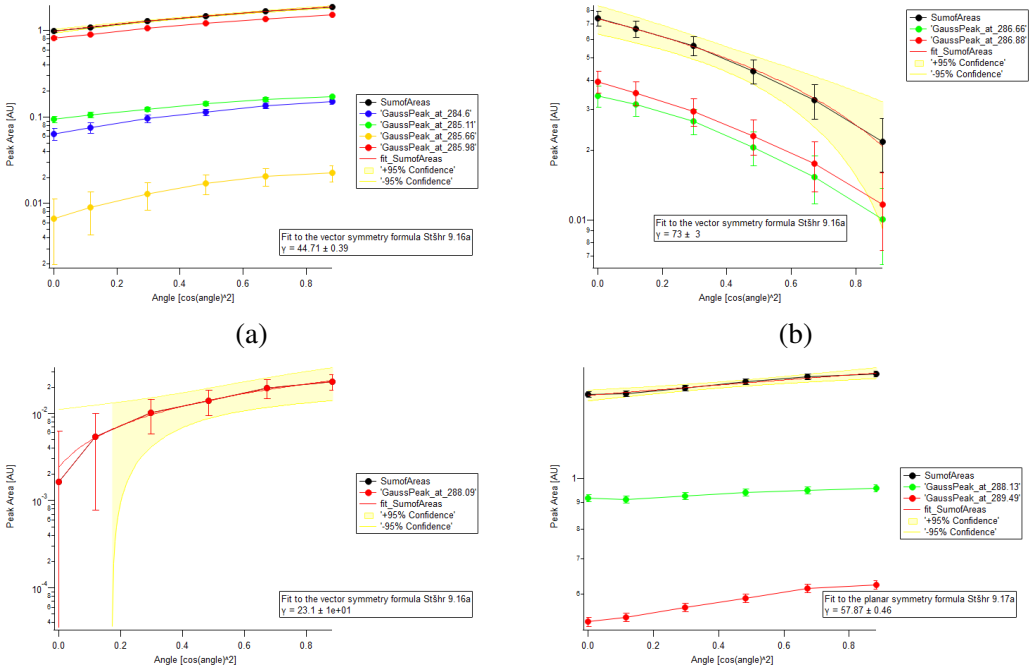
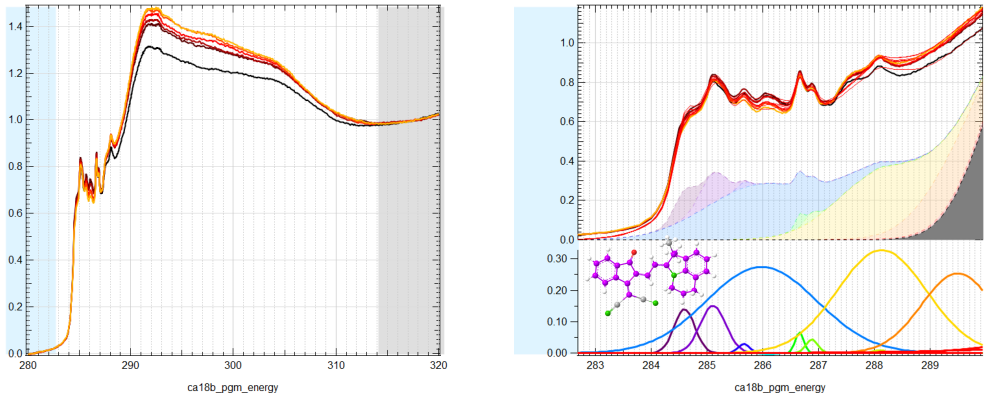


Figure 6.12: Plots of the areas under selected peaks from data for HB194 samples deposited on room temperature substrates, also shown in Figure 6.11, at various angles associated with the a) $C = C\ \pi^*$ transitions, b) $C \equiv N\ \pi^*$ transitions, and c) $C = O\ \pi^*$ transitions, and d) $C - H$, $C - C\ \sigma^*$ transitions. Also shown is the cumulative area and the associated fit to that using Equation 3.5 for a) and b) and the planar orbital equation [80] for c) and d).

NEXAFS data for HB194 samples deposited at $80°$C are shown in Figure 6.13a. A similar analysis was carried out as for the RT samples, and similar resonances were observed, however little to no angle dependency is observed in the data. The fitted data is shown in Figure 6.13b.

Using Equation 3.5, the areas under these peaks was fitted to determine orbital tilts and the results of these fits are shown in Figure 6.14. Unsurprisingly, all orbital tilts show values of $53.99 \pm 0.52°$, which is very close the magic angle $54.7°$, strongly suggesting that the substrate heating disrupts any preferential orientation present in the RT samples. The orbital tilt values for the suspected σ^* resonances

around the $C = O$ resonance at 288.1 eV do not deviate from the magic angle significantly even when fitted with the planar orbital equation [80]. As such Figure 6.14 shows the cumulative fit of all the resonances in the pre-edge region.



(a) (b)

Figure 6.13: a) Processed NEXAFS scans at multiple angles (shown in different colours) of HB194 deposited at 80°C. b) Fits of a), zoomed in to the pre-edge region, with several Gaussian oscillators and the NEXAFS edge, with the fitted data shown in thin red lines, and individual Gaussian peaks shown below for the median angle in the scan. The shaded region in the scan indicated the cumulative area from the fitted peaks, and is scaled down so as to increase readability of the data. Also shown in the HB194 molecule with moieties shaded to represent contributions from the NEXAFS data: C atoms shaded in purple to reflect the $C = C$ resonances, N atoms in green to reflect the $C \equiv N$ resonances, O atom shaded in red, and the remaining atoms without a specific colour as these resonances were not assigned with confidence.

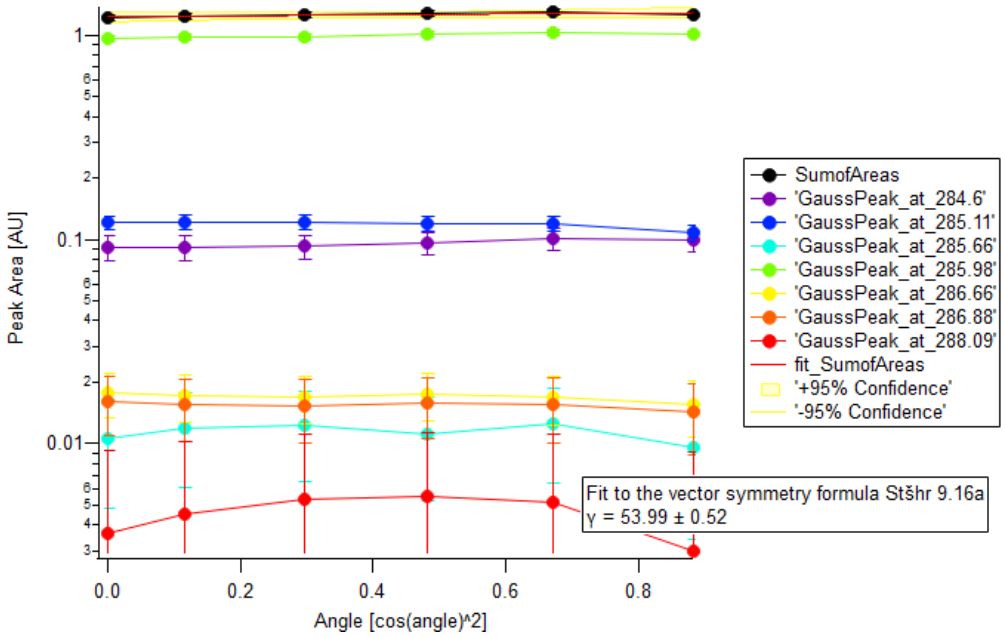


Figure 6.14: Plots of the areas under selected peaks from data of HB194 deposited on 80°C substrates, also shown in Figure 6.13, at various angles associated with the π^* transitions. Also shown is the cumulative area and the associated fit to that using Equation 3.5.

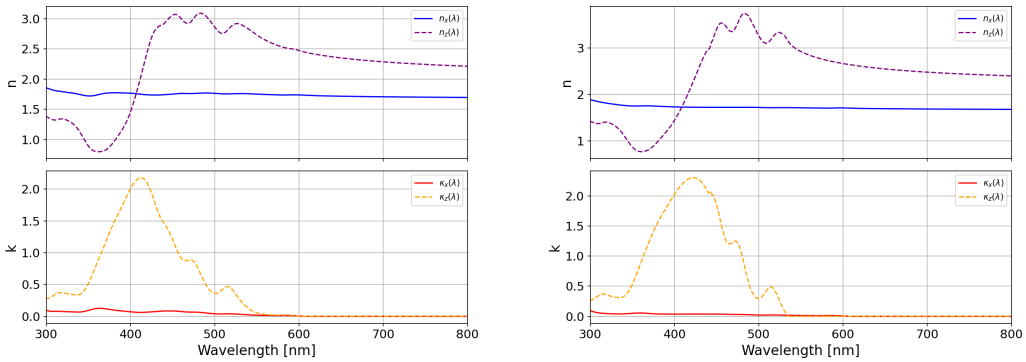
6.3 Spectroscopic Ellipsometry Results

The SE analysis used in this section utilised a multi-sample analysis approach with various samples deposited on different substrates with a common underlayer of MoO_3 to reduce the effect of templating effects. The substrates used were glass, Si with a native oxide ($\approx$ 3 nm), Si with a thermal oxide of 150 nm, and measurements included transmission measurements of the sample deposited on the glass substrate. This approach increases the sensitivity of the model to the out of plane components of the optical constants of the respective samples [130, 131].

6.3.1 a6T

SE data of the a6T samples was used to model the optical constants of the material and is shown in Figure 6.15a. Fitting details are provided in the Appendix A.2.4. Fits yielded an MSE of less than 13, and significant anisotropy was observed with the out-of-plane components dominating the spectrum. Further details of the fitting can be found in the Appendix. Using Equation 3.4 we calculate the mean orientation of the optical transition dipole moment with respect to the substrate normal, which yields a value of $S_\mu = 0.84$. This result is consistent with literature which has shown that a6T molecules pack in an upright manner in thin film at room temperature [20, 102].

Optical constants calculated from the SE results of the a6T HT samples are shown in Figure 6.15b. An identical fitting process as used in the RT samples was used for the HT samples. Fits yielded an MSE of less than 18, and similarly significant anisotropy was observed with the out-of-plane components again dominating the spectrum. Further details of the fitting can be found in the AppendixA.2.4. Using Equation 3.4 we calculate the mean orientation of the optical transition dipole (TD) with respect to the substrate normal, which yields a value of $S_\mu = 0.91$. This is consistent with previous studies on the effects of heating the substrate during a6T deposition [102].



(a) (b)

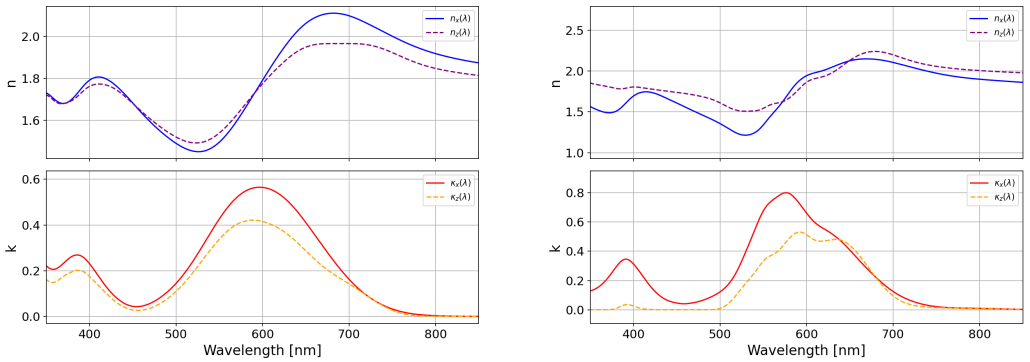
Figure 6.15: Optical constants modelled by spectroscopic ellipsometry of a6T films deposited on substrates held at a) RT and b) 110°C. Data from samples deposited on various substrates was used in a multi-sample analysis approach. All samples had a common underlayer of 3 nm (nominal) MoO_3 to negate any differing templating effects across different substrates.

6.3.2 DTDCPB

SE data of the DTDCPB RT samples was used to model the optical constants of the material and is shown in Figure 6.16a. Fits yielded an MSE of less than 6, and minor anisotropy was observed and tested for sensitivity by replacing the out-of-plane components with a transparent Cauchy layer, which led to a significant increase in the error of the fit. A similar approach was followed for samples deposited on substrates held at 80°C (HT), and fits of this data yielded an MSE less 4. The low MSEs indicate an excellent fit for both data sets. Fitting details for both RT and HT data sets can be found in the Appendix A.2.5. Using Equation 3.4 we calculate the mean orientation order parameter of the optical transition dipole (TD) with respect to the substrate normal for both RT and HT samples, which yields a value of $S_\mu = -0.10$ and $S_\mu = -0.12$ respectively. These results suggests weak anisotropy with a preferential orientation $\approx 60°$ for both RT and HT samples. Given the fact that a random distribution was observed for the facial

orientation from the NEXAFS results above it is likely that the SE results suggest a mostly random distribution of the TD as well in both RT and HT samples. It should be noted, however, that the orientation distribution of the TD in the HT data set is likely more constrained than that of the RT samples given the larger magnitude of the order parameter S_μ.

The optical constants in the heated substrate data also show more distinct peaks and for both in-plane and out-of-plane data, and may be a result of the heating causing some aggregation in the films. A noticeably blue-shifted peak appears at around 580 nm which could be indicative of some H-type aggregation [6].



(a) (b)

Figure 6.16: Optical constants modelled by spectroscopic ellipsometry of DTD-CPB films deposited on substrates held at a) RT and b) 80°C. Data from samples deposited on various substrates was used in a multi-sample analysis approach. All samples had a common underlayer of 3 nm (nominal) MoO_3 to negate any differing templating effects across different substrates.

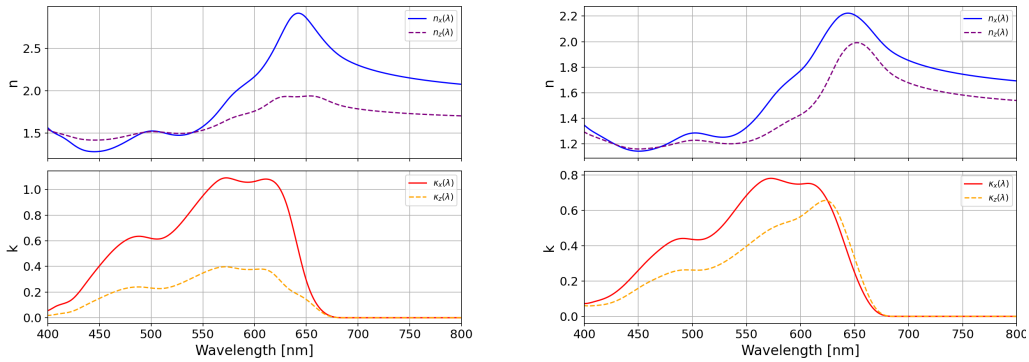
6.3.3 HB194

SE data of the HB194 RT was used to model the optical constants of the material and is shown in Figure 6.17a. Fits yielded an MSE of less than 14, and anisotropy was observed and tested for sensitivity by replacing the out-of-plane components with a transparent Cauchy layer, which led to a significant increase in the error of

the fit. Further details of the fitting can be found in the Appendix A.2.6. Using Equation 3.4 we can calculate the mean orientation of the optical TD with respect to the substrate normal, which yields a value of $S_\mu = -0.27$. This indicates a shallow inclination, and equates to an orientation of $23.19°$ of the TD with respect to the substrate plane. This result is close to the separation angle between diimers of the molecule in solution predicted by [104], which was $25°$. In solution there is a primary absorption peak at ≈ 580 nm, suggesting that the secondary peak at ≈ 620 nm is a result of peak splitting from some orientation offset between the optical TD from neighbouring molecules[6], which further reinforces the diimer-formation hypothesis stated above.

SE data of the HB194 samples deposited at $80°$C was used to model the optical constants of the material and is shown in Figure 6.17b. Fits yielded an MSE of less than 12, and anisotropy was observed and tested for sensitivity by replacing the out-of-plane components with a transparent Cauchy layer, which led to a significant increase in the error of the fit. Further details of the fitting can be found in the Appendix A.2.6. Using Equation 3.4 we calculate the mean orientation of the optical TD with respect to the substrate normal, which yields a value of $S_\mu = -0.05$, implying a random distribution of orientations, as was observed for the facial orientation in the NEXAFS analysis. Since the facial orientation was disrupted by the substrate heating, it is expected that the mean tilt angle of the long axis of the molecule would be similarly affected. Interestingly, the highest wavelength peak at 620 nm in the extinction coefficient data has a small ratio between in-plane and out-of-plane intensities than subsequent peaks. This could indicate that there is the appearance of two phases; a randomly oriented, isotropic, phase indicated by the peak 620 nm and a diimer phase indicated by the subsequent peaks. If we calculate the mean orientation using the ratio of extinction coefficients for the peak at 575 nm instead, we find that $S_\mu = -0.14$, which corresponds to an orientation of

$\approx 30°$ with respect to the substrate plane, which is also close the diimer separation angle predicted by [104].



(a) (b)

Figure 6.17: Optical constants modelled by spectroscopic ellipsometry of HB194 films deposited on substrates held at a) RT and b) $80°$C. Data from samples deposited on various substrates was used in a multi-sample analysis approach. All samples had a common underlayer of 3 nm (nominal) MoO_3 to negate any differing templating effects across different substrates.

6.4 GIWAXS results

Figure 6.18 shows the GIWAXS images of HB194 and DTDCPB thin films deposited on glass substrates at room temperature and at $80°$C. Details on the beamtime can be found in Chapter 3.

HB194 thin films deposited on substrates held at RT exhibit weak but broad scattering at approximately $q = 0.8$ Å^{-1}. This could indicate some weak ordering in packing of the molecules. When deposited on a substrate at held at $80°$C this scattering becomes weaker. This possibly signifies that the substrate heating causes a disruption in the packing of the molecules during deposition, similar to what was seen in both the NEXAFS and SE data sets, however the scattering is too weak to make meaningful comparisons between the images. What is clear, however, is

that there is no significant crystallinity suggested by the data at both RT and HT conditions.

DTDCPB thin films deposited at RT exhibit no discernible features other than weak scattering at $q_{xy} = 1.4$ Å^{-1}. This scattering is indicative $\pi - \pi$ stacking and is quite common in organic thin films. Samples deposited at 80°C show much weaker scattering in this region, however, and may imply that the substrate heating has also disrupted order in the DTDCPB thin films during deposition. However, similarly to the HB194 data, the scattering is not strong enough to make a meaningful comparison. It is also clear for the DTDCPB data that there is no significant crystallinity suggested by the data at both RT and HT conditions.

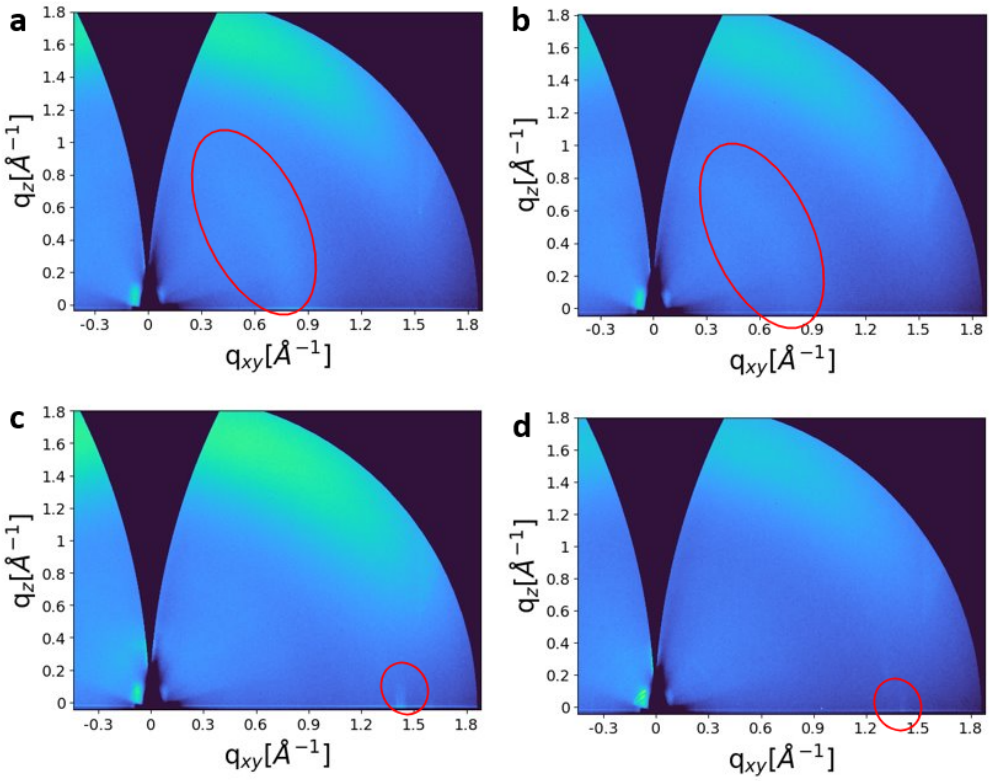


Figure 6.18: GIWAXS images of HB194 (a,b) and DTDCPB (c,d) thin films deposited at room temperature (a,c) and at 80°C (b,d). HB194 thin films show broad, but weak, scattering in a ring at $q = 0.8^{-1}$ (circled in red) that is less intense in higher temperature samples. DTDCPB thin films show weak scattering at $q_{xy} = 1.4^{-1}$, which becomes very weak in higher temperature samples.

6.5 Discussion

Table 6.1 summarise the key results from the chapter, in particular the orbital tilts (α) calculated from the NEXAFS analysis and the TDM orientation order parameters (S_μ) calculated from the SE analysis.

Material	α **(RT)**	α **(HT)**	S_μ **(RT)**	S_μ **(HT)**
a6T	$67.73 \pm 0.11°$	$77.25 \pm 0.28°$	0.84	0.94
DTDCPB	$54.53 \pm 0.08°$	$54.56 \pm 0.17°$	-0.10	-0.12
HB194	$44.71 \pm 0.39°$	$53.99 \pm 0.52°$	-0.27	-0.05 and -0.14

Table 6.1: Key results of the orientation analysis from the NEXAFS (α) and SE data (S_μ) of a6T, DTDCPB, and HB194 samples deposited on substrates held at RT and at HT ($110°$C for a6T, $80°$C for DTDCPB and HB194).

a6T thin films showed prominent edge-on orientation at an orbital tilt of $\alpha = 67.73 \pm 0.11°$ with respect to the substrate normal and a very high order parameter of $S_\mu = 0.84$. This is indicative of a molecule packing in fairly upright manner, with the molecules towards the surface of the thin film being tilted on their edge away from the substrate plane. Samples which were deposited at $110°$C showed even stronger edge-on orbital tilts of $\alpha = 77.25 \pm 0.28°$ with respect to the substrate normal with an even higher order parameter of $S_\mu = 0.94$. This indicates that upon substrate heating during the deposition of the thin film, a6T molecules pack in a far more upright manner. This is illustrated in Figure 6.19. The stronger edge-on orientation may allow for for more ordered $\pi - \pi$ stacking in the out-of-plane direction. Indeed this would be in agreement with GIWAXS data of this material found in the literature, where far stronger out-of-plane scattering is observed for this material at elevated substrate temperatures [102] compared to RT [20]. Indeed in the literature two phases of a6T are identified, a low temperature (LT) phase and a β phase, to coexist at RT, and at elevated substrate temperatures during deposition the β phase is dominant. In essence these phases are described as 'fairly upright' and 'very upright' orientations, and are nicely reproduced by the SE results in Figure 6.15 alone. The analysis from the NEXAFS results however expanded the understanding of these phases by also revealing a measurable change in the facial orientation in addition to the orientation of the backbone of the molecule.

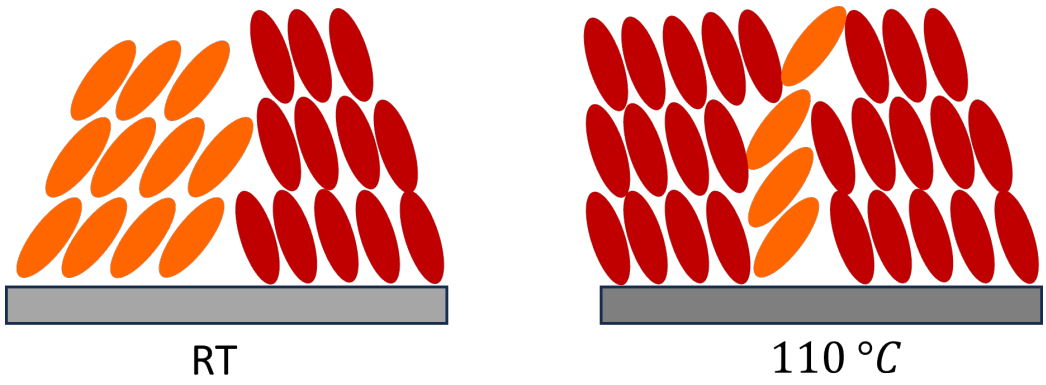


Figure 6.19: An illustration of the likely packing scenario for α-6T thin films deposited at room temperature (RT) and at 110°C (HT) based on the SE and NEXAFS results shown in this chapter as well as the literature [102]. At RT molecules orient in an upright manner with two phases present (indicated in orange and red). At HT the more upright phase (red) dominates the packing motif.

Overall, a6T served as an excellent benchmark for this analysis, clearly showing that the use of NEXAFS and SE can indeed reveal rich information about small molecules evaporated samples which is consistent with other data in the literature.

Extending this analysis to DTDCPB thin film samples revealed that DTDCPB shows orbital tilts close to $\alpha = 54.7°$ with respect to the substrate normal, and the lack of strong scattering in the GIWAXS images in Figure 6.18 suggest that this corresponds to random distribution with no preferential facial orientation. This was apparent in both RT and 80°C samples. Similarly, SE data showed weak anisotropy, yielding an order parameter of $S_\mu = -0.10$ at RT, which slightly increased in magnitude at 80°C to $S = -0.12$. This is illustrated in Figure 6.20. This indicates that, at least from a molecular orientation perspective, DTDCPB is quite resistant to morphological tuning using substrate heating during deposition, and consequently thermal annealing in general, up to 80°C.

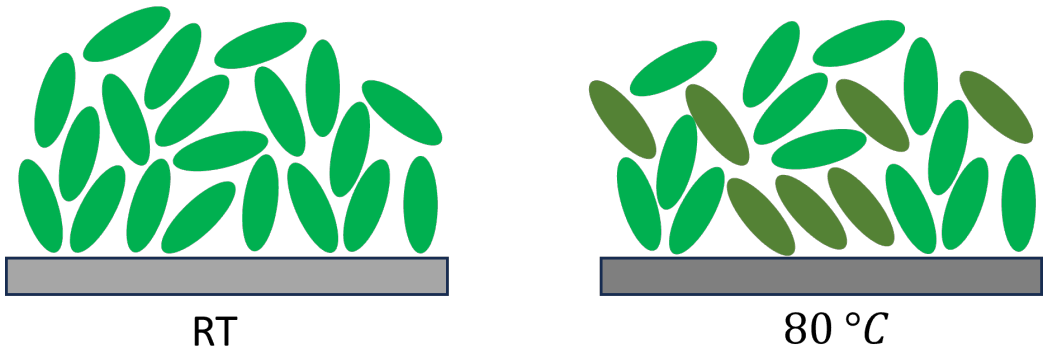


Figure 6.20: An illustration of the likely packing scenario for DTDCPB thin films deposited at room temperature (RT) and at 80°C (HT) based on the SE and NEXAFS results shown in this chapter. At RT the orientation of molecules is randomly distributed, and at HT this mostly remains the case with some minor element of preferential orientation beginning to appear (indicated by darker shades of green).

HB194 samples deposited at RT showed a facial orientation of $44.71 \pm 0.39°$ with respect to the substrate normal at room temperature. Samples deposited at 80°C showed a facial orientation close to $54.7°$ which likely corresponds to a random orbital tilt distribution with no preferential orientation, based on the lack of strong scattering from the GIWAXS images for these samples shown in Figure 6.18. Furthermore, there is a slight reduction in the already weak scattering intensity at $q = 0.8$ Å^{-1}. A shift to a disordered random distribution would correlate with this observation and, combined with the NEXAFS results discussed above, would reinforce the idea that the facial orientation switches from a weak preferential orientation in the RT samples to a random orientation distribution in the 80°C samples. This hypothesis is also reinforced by the SE results, which show that the order parameter S_μ changed from $S_\mu = -0.27$ to $S_\mu = -0.05$, which suggests a change to a random distribution. It is highly likely that a switch to a random distribution in molecular packing would be seen in both the facial orientation and the backbone (i.e. the optical TD) orientation. However, SE data from Figure 6.17 also suggests that there is some preferential TD orientation still present in the film

at 80°C. Subsequent peaks at lower wavelengths (575 nm and 480 nm) suggest that there is still some diimer structure present, and using the 575 nm peak ratio instead yields a order parameter of $S = -0.14$. This is illustrated in Figure 6.21. In conclusion, HB194 thin films deposited at RT have been observed to contain a weakly ordered phase with both a preferential facial and backbone orientation, likely containing some diimer structure, to a two phase system consisting of 1. some similar diimer phase and 2. a disordered, randomly oriented phase, when deposited at a substrate temperature of 80°C. This could be seen as an inversion of the thermal phase behaviour observed for a6T, which has been shown to shift from a two-phase system at RT to a mostly one-phase system at HT.

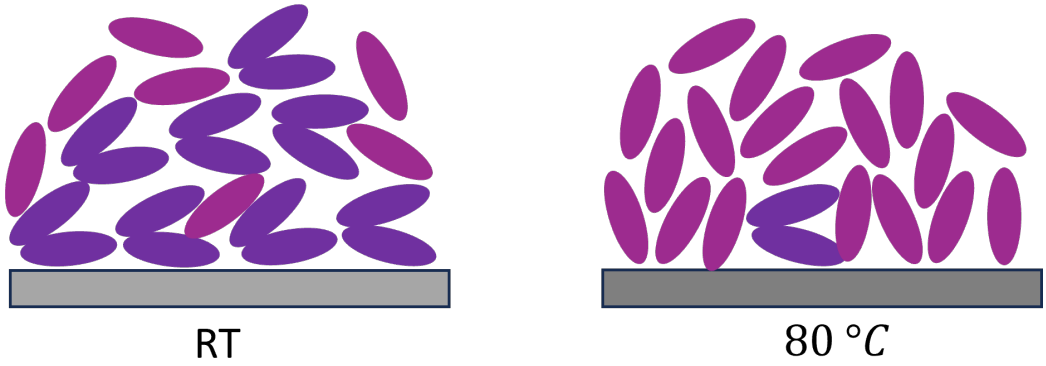


Figure 6.21: An illustration of the likely packing scenario for HB194 thin films deposited at room temperature (RT) and at 80°C (HT) based on the SE and NEXAFS results shown in this chapter. At RT there is a noticeable preferential orientation between molecules which likely manifests as a diimer structure with a constant angle of separation (indicated in dark purple). At HT this is somewhat disrupted by the appearance of a randomly distributed phase with no preferential orientation (indicated by lighter shades of purple).

6.6 Conclusion

The results in this chapter demonstrated that the combination of NEXAFS and SE can provide a far more holistic picture of the orientation distribution of evaporated

organic thin films than when used alone, as they both probe different aspects of the molecular thin films. NEXAFS is sensitive to the surface of a thin film and can be used to better understand the facial orientation, i.e. whether a molecule is tilted face-on or edge-on (or somewhere in between), by tracking the effects of a changing angle of incidence on the intensity of peaks belonging to the $1s \rightarrow \pi^*$ resonance in the NEXAFS spectrum. SE is sensitive to the bulk of the film and to the orientation of the backbone of the molecule, i.e. whether the molecule is aligned to the substrate plane or to the substrate normal, and was used to model the anisotropic components of the optical constants. This allowed for the ratio between the maximum of the in-plane and out-of-plane extinction coefficient to be used to estimate the mean orientation of the optical transition dipole moment with respect to the substrate normal. Finally, GIWAXS imaging was used to identify any crystallinity in the samples probed and to supplement the existing findings from the two previous result sets.

On the material side, a6T thin films were used to confirm that the analysis above would show that a6T films do indeed exhibit more upright-standing molecules upon substrate heating during deposition, as is observed in the literature. It was also further revealed that substrate heating also increased the facial orientation to a more edge-on orientation, which may play a role in the increase in crystallinity observed in this material upon heating in the literature. This observation also suggests that an increased backbone orientation, i.e. $S_\mu \rightarrow 1$, goes hand in hand with $\alpha \rightarrow 90°$, suggesting that these two parameters are not entirely independent, even though you cannot calculate one from the other. This makes sense considering the geometry, whereby as both parameters reach their extremes they limit the degrees of freedom available to each other, but when one is least constrained the other is as well.

DTDCPB and HB194 thin films deposited at room temperature and $80°$C were

also investigated using the same analysis. Findings suggested that DTDCPB exhibits a random distribution in both backbone and facial orientation which does not significantly change upon substrate heating to 80°C during deposition. However, the data suggests that HB194 thin films may exhibit a switch from both a preferential facial and TD orientation to a two-phase system exhibiting a similar TD orientation as well as a random orientation distribution, suggesting that at 80°C the molecular packing is significantly disrupted.

These findings lay the necessary groundwork for future studies using a more comprehensive analysis of more complex systems than pristine films, namely planar and bulk heterojunction films. By probing these types of orientation changes researchers can identify key changes in the facial orientation, which may have significant effects on molecular packing and related parameters such as charge transport, and the backbone orientation, which has significant effects on the absorption of the films. Both photophysical processes are key to OPV operation. Additionally, the interdependence between these two orientations can be better understood to form a more comprehensive understanding of the microstructure in this materials.

In particular, the results from this chapter will likely feed into a study which will extend the analysis used here to include more elemental edges from NEXAFS measurements, for example the Nitrogen edge at ≈ 410 eV, to better isolate the effects of functional groups in complex molecules. This will provide a much more robust framework for analysing blended films, with the ultimate goal of being able to comprehensively analyse device-relevant films in order to better identify key structure-property relationships in OPV.

7 | Summary, Evaluation and Recommendations

7.1 Concluding Remarks

They experimental work done in this thesis can be divided into two categories: 1. the identification of a candidate for evaporable NFA OSCs (Chapters 4 and 5) and 2. developing a more comprehensive view of the molecular orientation in evaporated organic thin films (Chapter 6).

7.1.1 Identification of candidate NFA for evaporable OSCs

In Chapter 4 a material investigation study was performed on three candidate NFAs, namely the perylene diimide PDIFCN2, and the oligothiophenes TTR, TTIC4F, and BTIC-H. This investigation mainly comprised energetic (via ambient photoelectron spectroscopy) and optical (via spectroscopic ellipsometry) characterisation of thin films of each material fabricated via vacuum deposition. Due to its favourable optical (peak extinction coefficient > 0.6) and energetic properties (HOMO ≈ -5.9 eV, LUMO ≈ -3.6 eV) further microstructural characterisation was also performed on BTIC-H, including further analysis of the SE data, NEXAFS, and GIWAXS measurements. This revealed that when deposited in a pristine film on transparent substrates (standard glass, ITO-coated glass, quartz) there is a noticeable preferential orientation in both the transition dipole moment (i.e. the long molecular axis or backbone of the molecule) and the orbital vector (i.e. the short molecular axis or the molecular face). These results indicate that BTIC-H packs at a shallow angle of inclination from the substrate in a mostly face-on configuration ($S = -0.26$, $\alpha \approx 60°$).

Chapter 5 explored the use of BTIC-H in OSC devices. First, PHJ devices were explored with a few different donor molecules. Results were promising, a good V_{OC} was observed for most devices (≈ 1 V) but only modest photocurrents were achieved with poor EQE ($< 15\%$ for most devices), and consequently poor PCEs ($\approx 1\%$ for the best devices). Due combination of a good V_{OC} and relatively good J_{SC} (within the sample of devices investigated) DCv5T was selected as a donor to further investigate with BTIC-H but BHJ OSCs with this combination yielded extremely poor J_{SC} (< 1 mA/cm^2). Further investigation suggested that when blended together BTIC-H and DCV5T likely intermix strongly, disrupting any percolation pathways that are necessary for good charge extraction. Mobility measurements of the blend also revealed very low values which suggest that a high recombination in the blend is also a likely reason charge extraction.

This study demonstrated that there is very real promise for evaporable NFAs. BTIC-H was a molecule originally synthesised for use in solution processed OSCs, and yet device results showed better or similar performance when compared with optimised solution processed devices (devices studied in this thesis showed better V_{OC} and voltage losses and comparable J_{SC} and PCE).

There are several limitations in the study that should be acknowledged, and may inform future studies:

- Energy level characterisation of the LUMO values had a high uncertainty. More reliable measurement of this could be performed on the systems, for example through the use of inverse photoelectron spectroscopy.
- CT state analysis using electroluminesence measurements was not done and would yield valuable insight into the role of the CT state in the loss pathways present in devices made.
- Further BHJ optimisation could have been performed on the DCV5T: BTIC-

H devices, in particular by probing different thicknesses, substrate temperatures, and donor:acceptor concentrations, though adequate deposition rate control would be challenging for these two materials in particular given their evaporation behaviour.

- BHJ devices could be made for the other donors used in the PHJ systems, as the mixed heterojunction might overcome barriers introduced by the planar heterojunction (for example the energetic landscape could change due to interactions between different molecular species which could overcome previously existing energetic barriers in the PHJs).
- Further analysis could be done on TTR and PDIFCN2, in particular by pairing them with a wider variety of donor molecules.

Recommendations for future studies include some of items above as well as a more systematic study of different molecular structures, for example making iterative changes in the molecular design of BTIC-H to inform a more comprehensive design study of evaporable NFAs. This could build on the current results from this study, as well as the preliminary results of TTR and TTIC4F. Additional measurements were performed on a new molecule not included in this thesis which further tuned the bithiophene structure used by these molecules, but results were too preliminary to include in this thesis.

7.1.2 Developing a more comprehensive view of the molecular orientation in evaporated organic thin films

Chapter 6 explored the use of a combination of techniques to more comprehensively study molecular orientation present in evaporated thin films, specifically thin films of alpha-sexithiophene (a6T), the merocyanine dye HB194, and the donor-acceptor-acceptor type molecule DTDCPB. In particular, angle resolved

near edge x-ray absorption fine structure (NEXAFS) spectroscopy was used to measure the tilt of the orbital vector of primarily the C 1s$\rightarrow \pi^*$ transitions, which revealed the mean facial orientation of molecules towards the surface of the thin film. Spectroscopic ellipsometry measurements were performed on similar systems and optical models were generated to describe the optical constants of the materials. Using the extinction coefficient the mean order parameter describing the orientation of the optical transition dipole was calculated, which yields an approximation of the orientation of molecular backbone. Finally GIWAXS measurements were used to further contextualise the findings.

Key findings showed that the techniques correctly reproduce the backbone orientation of a6T as shown in the literature, and further advances the understanding of the molecular packing by showing that the molecules also have a distinct edge-on facial orientation. When deposited on heated substrates both these orientations increased in magnitude, becoming more upright and more tilted towards being edge-on.

DTDCPB and HB194 thin films deposited at room temperature and elevated substrate temperatures were also investigated using the same analysis. Findings suggested that DTDCPB exhibits a random distribution in both backbone and facial orientation which does not significantly change upon substrate heating during deposition. However, HB194 thin films likely exhibit a switch from both a preferential facial and optical transition dipole (TD) orientation to a two-phase system exhibiting a similar TD orientation as well as a random orientation distribution, suggesting that at the investigated temperature (80°C) the molecular packing is significantly disrupted.

These findings lay the necessary groundwork for future studies using a more comprehensive analysis of more complex systems than pristine films, namely planar

and bulk heterojunction films. By probing these types of orientation changes researchers can identify key changes in the facial orientation, which may have significant effects on molecular packing and related parameters such as charge transport, and the backbone orientation, which has significant effects on the absorption of the films. Both these photophysical processes are key to OPV operation.

Some of the limitations of the work done in this chapter are as follows:

- No computational modelling was used in this work to justify the assignment of peaks in the NEXAFS spectra to functional groups. Instead, cross-referencing with data used in this study and referencing similar molecular structures in the literature was done to justify the peak assignment. While certainly valid, computational modelling would definitely provide an additional layer of reliability to the findings.
- Gaussian oscillators were used for all NEXAFS peak fitting, and while this is the convention in the literature there is also evidence to suggest that that alternative functional forms should be attempted, namely Lorentzian or Voigt oscillators, which may better fit the data, in particular the peaks around the NEXAFS edge which were mostly omitted during the analysis in this thesis.
- There was a time delay between SE and NEXAFS measurements which may have caused sample degradation that might decouple the SE results from the NEXAFS results.
- The orientation order parameter is dependant on the maximum of in-plane and out-of-plane extinction coefficients, however, it might be better to calculate the order parameter from the extinction coefficient ratio of distinct peaks rather than the maximum of the whole spectrum, as was demonstrated for the case of HB194. This would require further work to justify this ap-

proach.

In terms of future studies, the results from Chapter 6 will likely feed into a follow up study which will extend the analysis used here to include more elemental edges from NEXAFS measurements, for example the Nitrogen edge at ≈ 410 eV, to better isolate the effects of functional groups in complex molecules. This will provide a much more robust framework for analysing blended films, with the ultimate goal of being able to comprehensively analyse device-relevant films in order to better identify key structure-property relationships in OPV.

7.1.3 Final Remarks

At the start of this thesis it was discussed that there is little research on vacuum deposited NFAs compared to their solution processed counterparts. The results of Chapter 4 and 5, specifically those of samples using the molecule BTIC-H, demonstrate that vacuum deposited non-fullerene acceptors that have been developed using contemporary design practices are possible. The results, while modest, make the case that these materials deserve the attention of the research community in order to both improve on the design and develop new materials that can exploit both the advantages of modern non-fullerene acceptor molecules as well as the many advantages of vacuum deposition as a fabrication route.

In addition to the viability of vacuum deposited NFAs discussed above, the results in Chapter 6 also demonstrate that the orientation of organic thin films can be far more comprehensively determined by using complementary techniques such as Spectroscopic Ellipsometry and NEXAFS. This removes ambiguity in findings by differentiating between molecular facial and backbone orientations, and allows for a far richer analysis of the microstructure of organic thin films. These techniques are also easily adaptable to the analysis of the orientation of both donor

and acceptor films fabricated via vacuum deposition. This allows for findings to be related to device operation far more easily than for measurements made on solution processed samples, which often require additional considerations of polymer chains and solvent molecules, for example.

It is my strong belief that organic photovoltaics, specifically vacuum deposited organic photovoltaics, will play an integral role in the energy security of our future society. To this end, it is my hope that the findings in this thesis will contribute to the advancement of organic photovoltaic research.

Bibliography

[1] Research and Markets. *Global OLED Market with COVID-19 Impact Analysis by Product Type (Smartphones, Television Sets, Smart Wearables, Large Format Displays), Panel Type, Panel Size, Technology, Vertical, and Geography - Forecast to 2026*. Report. 2021. URL: https://www.researchandmarkets.com/reports/5309109/global-oled-market-with-covid-19-impact-analysis.

[2] Expert Market Research. *Global OLED Market Report and Forecast 2024-2032*. Report. 2023. URL: https://www.expertmarketresearch.com/reports/oled-market.

[3] Precedence Research. *Global OLED Market Size, Share, Trends, Growth, Forecast Analysis Report By Segment, By Product, By Application, By Region - Global Forecast 2022-2030*. Report. 2023. URL: https://www.precedenceresearch.com/press-release/oled-market.

[4] Heliatek GmbH. *Organic Photovoltaics - Truly Green Energy: "Ultra-Low Carbon Footprint"*. Report. 2020. URL: https://www.heliatek.com/fileadmin/user_upload/pdf_documents/2020-10_Heliatek_Truly_Green_Energy_Ultra_Low_Carbon_Footprint_REV2.pdf.

[5] IRENA. *Renewable Power Generation Costs in 2022*. Report. 2023. URL: https://mc-cd8320d4-36a1-40ac-83cc-3389-cdn-endpoint.azureedge.net/-/media/Files/IRENA/Agency/Publication/2023/Aug/IRENA_Renewable_power_generation_costs_in_2022.pdf?rev=cccb713bf8294cc5bec3f870e1fa15c2.

[6] Anna Köhler and Heinz Bässler. *Electronic Processes in Organic Semiconductors : An Introduction*. Wiley-VCH Verlag GmbH & Co. KGaA, 2015.

[7] C. W. Tang. "Two-layer organic photovoltaic cell". In: *Applied Physics Letters* 48.2 (1986), pp. 183–185. ISSN: 0003-6951. DOI: 10.1063/1.96937. URL: https://dx.doi.org/10.1063/1.96937.

[8] Ardalan Armin et al. "A History and Perspective of Non-Fullerene Electron Acceptors for Organic Solar Cells". In: *Advanced Energy Materials* 11.15 (2021), p. 2003570. ISSN: 1614-6832. DOI: 10.1002/aenm.202003570.

[9] Yang Li et al. "Recent Progress in Organic Solar Cells: A Review on Materials from Acceptor to Donor". In: *Molecules* 27.6 (2022), p. 1800. ISSN: 1420-3049. DOI: 10.3390/molecules27061800. URL: https://dx.doi.org/10.3390/molecules27061800.

[10] Yuhang Liu et al. "Aggregation and morphology control enables multiple cases of high-efficiency polymer solar cells". In: *Nature Communications* 5.1 (2014), p. 5293. ISSN: 2041-1723. DOI: 10.1038/ncomms6293. URL: https://www.ncbi.nlm.nih.gov/pmc/articles/PMC4242436.

[11] Yuze Lin et al. "An Electron Acceptor Challenging Fullerenes for Efficient Polymer Solar Cells". In: *Advanced Materials* 27.7 (2015), pp. 1170–1174. ISSN: 0935-9648. DOI: 10.1002/adma.201404317.

[12] Lei Zhu et al. "Single-junction organic solar cells with over 19% efficiency enabled by a refined double-fibril network morphology". In: *Nature Materials* 21.6 (2022), pp. 656–663. ISSN: 1476-1122. DOI: 10.1038/s41563-022-01244-y. URL: https://dx.doi.org/10.1038/s41563-022-01244-y.

[13] Viviane Nogueira Hamanaka et al. "Investigating the influence of the solution-processing method on the morphological properties of organic semiconductor films and their impact on OLED performance and lifetime". In: 78 (2020). 1566-1199, p. 105509. URL: https://www.sciencedirect.com/science/article/pii/S1566119919305361.

[14] Irfan Habib et al. "Vacuum deposited organic solar cells with BTIC-H as A-D-A non-fullerene acceptor". In: *APL Materials* 11.6 (2023). ISSN: 2166-532X. DOI: 10.1063/5.0148208. URL: https://doi.org/10.1063/5.0148208.

[15] Yao Liu et al. "Photophysics of Monodisperse Platinum-Acetylide Oligomers: Delocalization in the Singlet and Triplet Excited States". In: *Journal of the American Chemical Society* 124.42 (2002). doi: 10.1021/ja027639i 0002-7863, pp. 12412–12413. URL: https://doi.org/10.1021/ja027639i.

[16] Wolfgang Tress. *Organic Solar Cells*. Springer Cham, 2016.

[17] George Murray Burnett, John N. Sherwood, and Alastair M North. *Transfer and storage of energy by molecules: Rotational Energy*. Wiley-Interscience, 1969.

[18] Jean-Luc Bredas. "Mind the gap!" In: *Mater. Horiz.* 1.1 (2014), pp. 17–19. ISSN: 2051-6347. DOI: 10.1039/c3mh00098b.

[19] Christoph Schünemann et al. "Evaluation and Control of the Orientation of Small Molecules for Strongly Absorbing Organic Thin Films". In: *The Journal of Physical Chemistry C* 117.22 (2013), pp. 11600–11609. ISSN: 1932-7447. DOI: 10.1021/jp400604j.

[20] T. L. Derrien et al. "In Situ Observations of the Growth Mode of Vacuum-Deposited α-Sexithiophene". In: *The Journal of Physical Chemistry C*

124.22 (2020), pp. 11863–11869. ISSN: 1932-7447. DOI: 10.1021/acs.jpcc.0c00447.

[21] Jan Meiss et al. "Tetrapropyl-tetraphenyl-diindenoperylene derivative as a green absorber for high-voltage stable organic solar cells". In: *Physical Review B* 83.16 (2011). PRB, p. 165305. URL: https://link.aps.org/doi/10.1103/PhysRevB.83.165305.

[22] Richard R. Lunt et al. "Exciton diffusion lengths of organic semiconductor thin films measured by spectrally resolved photoluminescence quenching". In: *Journal of Applied Physics* 105.5 (2009). ISSN: 0021-8979. DOI: 10.1063/1.3079797. URL: https://doi.org/10.1063/1.3079797.

[23] Yuhki Terao, Hiroyuki Sasabe, and Chihaya Adachi. "Correlation of hole mobility, exciton diffusion length, and solar cell characteristics in phthalocyanine/fullerene organic solar cells". In: *Applied Physics Letters* 90.10 (2007). ISSN: 0003-6951. DOI: 10.1063/1.2711525. URL: https://doi.org/10.1063/1.2711525.

[24] Richard R. Lunt, Jay B. Benziger, and Stephen R. Forrest. "Relationship between Crystalline Order and Exciton Diffusion Length in Molecular Organic Semiconductors". In: *Advanced Materials* 22.11 (2010), pp. 1233–1236. ISSN: 0935-9648. DOI: 10.1002/adma.200902827. URL: https://deepblue.lib.umich.edu/bitstream/2027.42/69160/1/1233_ftp.pdf.

[25] Martina Causa' et al. "Femtosecond Dynamics of Photoexcited C60 Films". In: *The Journal of Physical Chemistry Letters* 9.8 (2018). doi: 10.1021/acs.jpclett.8b00520, pp. 1885–1892. URL: https://doi.org/10.1021/acs.jpclett.8b00520.

[26] Koen Vandewal et al. “On the origin of the open-circuit voltage of polymer-fullerene solar cells”. In: *Nature Materials* 8.11 (2009), pp. 904–909. ISSN: 1476-1122. DOI: 10.1038/nmat2548.

[27] Koen Vandewal et al. “Relating the open-circuit voltage to interface molecular properties of donor:acceptor bulk heterojunction solar cells”. In: *Physical Review B* 81.12 (2010). ISSN: 1098-0121. DOI: 10.1103/physrevb.81.125204.

[28] Christoph J Brabec et al. “Tracing photoinduced electron transfer process in conjugated polymer/fullerene bulk heterojunctions in real time”. In: *Chemical Physics Letters* 340.3-4 (2001), pp. 232–236. ISSN: 0009-2614. DOI: 10.1016/s0009-2614(01)00431-6.

[29] Safakath Karuthedath et al. “Intrinsic efficiency limits in low-bandgap non-fullerene acceptor organic solar cells”. In: *Nature Materials* 20.3 (2021), pp. 378–384. ISSN: 1476-1122. DOI: 10.1038/s41563-020-00835-x. URL: https://dx.doi.org/10.1038/s41563-020-00835-x.

[30] Jonathan A. Bartelt et al. “Charge-Carrier Mobility Requirements for Bulk Heterojunction Solar Cells with High Fill Factor and External Quantum Efficiency $> 90\%$”. In: *Advanced Energy Materials* 5.15 (2015). 1614-6832, p. 1500577. URL: https://doi.org/10.1002/aenm.201500577.

[31] Valentina Belova et al. “Structure-Dependent Charge Transfer in Molecular Perylene-Based Donor/Acceptor Systems and Role of Side Chains”. In: *The Journal of Physical Chemistry C* 124.21 (2020), pp. 11639–11651. ISSN: 1932-7447. DOI: 10.1021/acs.jpcc.0c00230.

[32] Andreas Opitz et al. “Charge Separation at Molecular DonorâAcceptor Interfaces: Correlation Between Morphology and Solar Cell Performance”.

In: *IEEE Journal of Selected Topics in Quantum Electronics* 16.6 (2010), pp. 1707–1717. ISSN: 1077-260X. DOI: 10.1109/jstqe.2010.2048096.

[33] Kenneth R. Graham et al. "The Roles of Structural Order and Intermolecular Interactions in Determining Ionization Energies and Charge-Transfer State Energies in Organic Semiconductors". In: *Advanced Energy Materials* 6.22 (2016). 1614-6832, p. 1601211. URL: https://doi.org/10.1002/aenm.201601211.

[34] Long Ye et al. "Quantitative relations between interaction parameter, miscibility and function in organic solar cells". In: *Nature Materials* 17.3 (2018), pp. 253–260. ISSN: 1476-1122. DOI: 10.1038/s41563-017-0005-1.

[35] Minlu Zhang et al. "Bulk Heterojunction Photovoltaic Cells with Low Donor Concentration". In: *Advanced Materials* 23.42 (2011). 0935-9648, pp. 4960–4964. URL: https://doi.org/10.1002/adma.201102173.

[36] Gareth John Moore et al. "Ultrafast Charge Dynamics in Dilute-Donor versus Highly Intermixed TAPC:C60 Organic Solar Cell Blends". In: *The Journal of Physical Chemistry Letters* 11.14 (2020), pp. 5610–5617. ISSN: 1948-7185. DOI: 10.1021/acs.jpclett.0c01495.

[37] Alexander I. Kitaigorodsky. "Mixed Crystals". In: *Springer Series in Solid-State Sciences* (1984). ISSN: 0171-1873. DOI: 10.1007/978-3-642-81672-7.

[38] Long Ye et al. "Quenching to the Percolation Threshold in Organic Solar Cells". In: *Joule* 3.2 (2019), pp. 443–458. ISSN: 2542-4351. DOI: 10.1016/j.joule.2018.11.006.

[39] Andreas Opitz et al. “Ordered Donor-Acceptor Complex Formation and Electron Transfer in Co-deposited Films of Structurally Dissimilar Molecules”. In: *The Journal of Physical Chemistry C* 124.20 (2020), pp. 11023–11031. ISSN: 1932-7447. DOI: 10.1021/acs.jpcc.0c02465.

[40] Wei Li et al. “Organic solar cells with near-unity charge generation yield”. In: *Energy Environmental Science* 14.12 (2021), pp. 6484–6493. ISSN: 1754-5692. DOI: 10.1039/d1ee01367j.

[41] Koen Vandewal et al. “Efficient charge generation by relaxed charge-transfer states at organic interfaces”. In: *Nature Materials* 13.1 (2014), pp. 63–68. ISSN: 1476-1122. DOI: 10.1038/nmat3807.

[42] Kazuaki Kawashima et al. “High-efficiency polymer solar cells with small photon energy loss”. In: *Nature Communications* 6.1 (2015), p. 10085. ISSN: 2041-1723. DOI: 10.1038/ncomms10085. URL: https://www.nature.com/articles/ncomms10085.pdf.

[43] Weiwei Li et al. “High Quantum Efficiencies in Polymer Solar Cells at Energy Losses below 0.6 eV”. In: *Journal of the American Chemical Society* 137.6 (2015). doi: 10.1021/ja5131897 0002-7863, pp. 2231–2234. URL: https://doi.org/10.1021/ja5131897.

[44] Xiaoling Ma et al. “Achieving 17.4% Efficiency of Ternary Organic Photovoltaics with Two Well-Compatible Nonfullerene Acceptors for Minimizing Energy Loss”. In: *Advanced Energy Materials* 10.31 (2020). 1614-6832, p. 2001404. URL: https://doi.org/10.1002/aenm.202001404.

[45] Qishi Liu et al. “18% Efficiency organic solar cells”. In: 65.4 (2020). 2095-9273, pp. 272–275. URL: https://www.sciencedirect.com/science/article/pii/S2095927320300013.

[46] Yong Cui et al. “Single-Junction Organic Photovoltaic Cells with Approaching 18% Efficiency”. In: *Advanced Materials* 32.19 (2020). 0935-9648, p. 1908205. URL: https://doi.org/10.1002/adma.201908205.

[47] Heinz Bässler and Anna Köhler. “"Hot or cold": how do charge transfer states at the donor-acceptor interface of an organic solar cell dissociate?” In: *Physical Chemistry Chemical Physics* 17.43 (2015), pp. 28451–28462. ISSN: 1463-9076. DOI: 10.1039/c5cp04110d.

[48] Simon Gélinas et al. “Ultrafast Long-Range Charge Separation in Organic Semiconductor Photovoltaic Diodes”. In: *Science* 343.6170 (2014), pp. 512–516. ISSN: 0036-8075. DOI: 10.1126/science.1246249. URL: https://www.repository.cam.ac.uk/bitstream/1810/286327/1/1246249RevisedText3.pdf.

[49] D. Amarasinghe Vithanage et al. “Visualizing charge separation in bulk heterojunction organic solar cells”. In: *Nature Communications* 4.1 (2013). ISSN: 2041-1723. DOI: 10.1038/ncomms3334. URL: https://www.nature.com/articles/ncomms3334.pdf.

[50] Dan Liraz and Nir Tessler. “Charge dissociation in organic solar cells - from Onsager and Frenkel to modern models”. In: *Chemical Physics Reviews* 3.3 (2022), p. 031305. ISSN: 2688-4070. DOI: 10.1063/5.0099986.

[51] V. I. Arkhipov, E. V. Emelianova, and H. Bässler. “Dopant-assisted charge carrier photogeneration in conjugated polymers”. In: 372.5 (2003). 0009-2614, pp. 886–892. URL: https://www.sciencedirect.com/science/article/pii/S0009261403005207.

[52] V. I. Arkhipov, P. Heremans, and H. Bässler. “Why is exciton dissociation so efficient at the interface between a conjugated polymer and an elec-

tron acceptor?" In: *Applied Physics Letters* 82.25 (2003), pp. 4605–4607. ISSN: 0003-6951. DOI: 10.1063/1.1586456.

[53] O. Rubel et al. "Exact Solution for Hopping Dissociation of Geminate Electron-Hole Pairs in a Disordered Chain". In: *Physical Review Letters* 100.19 (2008). ISSN: 0031-9007. DOI: 10.1103/physrevlett.100.196602.

[54] W. Shockley. "The Theory of p-n Junctions in Semiconductors and p-n Junction Transistors". In: *Bell System Technical Journal* 28.3 (1949), pp. 435–489. ISSN: 0005-8580. DOI: 10.1002/j.1538-7305.1949.tb03645.x.

[55] G. Yu et al. "Polymer Photovoltaic Cells: Enhanced Efficiencies via a Network of Internal Donor-Acceptor Heterojunctions". In: *Science* 270.5243 (1995), pp. 1789–1791. ISSN: 0036-8075. DOI: 10.1126/science.270.5243.1789.

[56] Yuze Lin et al. "A Facile Planar Fused-Ring Electron Acceptor for As-Cast Polymer Solar Cells with 8.71% Efficiency". In: *Journal of the American Chemical Society* 138.9 (2016). doi: 10.1021/jacs.6b00853 0002-7863, pp. 2973–2976. URL: https://doi.org/10.1021/jacs.6b00853.

[57] Dong Meng et al. "Three-Bladed Rylene Propellers with Three-Dimensional Network Assembly for Organic Electronics". In: *Journal of the American Chemical Society* 138.32 (2016). doi: 10.1021/jacs.6b04368 0002-7863, pp. 10184–10190. URL: https://doi.org/10.1021/jacs.6b04368.

[58] Sarah Holliday et al. "High-efficiency and air-stable P3HT-based polymer solar cells with a new non-fullerene acceptor". In: *Nature Communications* 7.1 (2016), p. 11585. ISSN: 2041-1723. DOI: 10.1038/ncomms11585.

URL: https://qmro.qmul.ac.uk/xmlui/bitstream/123456789/16208/1/Nielsen%20High-efficiency%20and%20air-stable%202016%20Published.pdf.

[59] Ajay K. Pandey, Sylvie Dabos-Seignon, and Jean-Michel Nunzi. "Pentacene: PTCDI-C13H27 molecular blends efficiently harvest light for solar cell applications". In: *Applied Physics Letters* 89.11 (2006), p. 113506. ISSN: 0003-6951. DOI: 10.1063/1.2352800. URL: https://espace.library.uq.edu.au/view/UQ:234501/UQ234501_OA.pdf.

[60] Paul Sullivan et al. "Halogenated Boron Subphthalocyanines as Light Harvesting Electron Acceptors in Organic Photovoltaics". In: *Advanced Energy Materials* 1.3 (2011), pp. 352–355. ISSN: 1614-6832. DOI: 10.1002/aenm.201100036.

[61] G. D. Sharma et al. "Efficient bulk heterojunction devices based on phenylenevinylene small molecule and perylene-pyrene bisimide". In: *J. Mater. Chem.* 20.3 (2010), pp. 561–567. ISSN: 0959-9428. DOI: 10.1039/b918527e.

[62] Jianquan Zhang et al. "Material insights and challenges for non-fullerene organic solar cells based on small molecular acceptors". In: *Nature Energy* 3.9 (2018), pp. 720–731. ISSN: 2058-7546. DOI: 10.1038/s41560-018-0181-5.

[63] Jun Yan et al. "Identifying structure-absorption relationships and predicting absorption strength of non-fullerene acceptors for organic photovoltaics". In: *Energy Environmental Science* 15.7 (2022), pp. 2958–2973. ISSN: 1754-5692. DOI: 10.1039/d2ee00887d.

[64] Jiehao Fu et al. "19.31% binary organic solar cell and low non-radiative recombination enabled by non-monotonic intermediate state transition". In:

Nature Communications 14.1 (2023). ISSN: 2041-1723. DOI: 10.1038/s41467-023-37526-5.

[65] Wenchao Zhao et al. "Molecular Optimization Enables over 13% Efficiency in Organic Solar Cells". In: *Journal of the American Chemical Society* 139.21 (2017). doi: 10.1021/jacs.7b02677 0002-7863, pp. 7148–7151. URL: https://doi.org/10.1021/jacs.7b02677.

[66] Jun Yuan et al. "Single-Junction Organic Solar Cell with over 15% Efficiency Using Fused-Ring Acceptor with Electron-Deficient Core". In: *Joule* 3.4 (2019), pp. 1140–1151. ISSN: 2542-4351. DOI: 10.1016/j.joule.2019.01.004. URL: http://www.cell.com/article/S2542435119300327/pdf.

[67] Moritz Riede, Donato Spoltore, and Karl Leo. "Organic Solar Cells - The Path to Commercial Success". In: *Advanced Energy Materials* 11.1 (2021), p. 2002653. ISSN: 1614-6832. DOI: 10.1002/aenm.202002653.

[68] Zhenzhen Zhang and Yuze Lin. "Organic Semiconductors for Vacuum-Deposited Planar Heterojunction Solar Cells". In: *ACS Omega* 5.39 (2020), pp. 24994–24999. ISSN: 2470-1343. DOI: 10.1021/acsomega.0c03868.

[69] Kjell Cnops et al. "8.4% efficient fullerene-free organic solar cells exploiting long-range exciton energy transfer". In: *Nature Communications* 5.1 (2014). ISSN: 2041-1723. DOI: 10.1038/ncomms4406. URL: https://www.nature.com/articles/ncomms4406.pdf.

[70] Qihui Yue et al. "Vacuum-deposited organic solar cells utilizing a low-bandgap non-fullerene acceptor". In: *Journal of Materials Chemistry C* 10.7 (2022), pp. 2569–2574. ISSN: 2050-7526. DOI: 10.1039/d1tc03954g.

[71] Xiaojun Li et al. "Simplified synthetic routes for low cost and high photovoltaic performance n-type organic semiconductor acceptors". In: *Nature Communications* 10.1 (2019). ISSN: 2041-1723. DOI: 10.1038/

s41467-019-08508-3. URL: https://doi.org/10.1038/s41467-019-08508-3.

[72] Taeho Lee et al. "Simple Bithiophene-Rhodanine-Based Small Molecule Acceptor for Use in Additive-Free Nonfullerene OPVs with Low Energy Loss of 0.51 eV". In: *Advanced Energy Materials* 9.16 (2019), p. 1804021. ISSN: 1614-6832. DOI: 10.1002/aenm.201804021.

[73] Zhi-Peng Yu et al. "Simple non-fused electron acceptors for efficient and stable organic solar cells". In: *Nature Communications* 10.1 (2019). ISSN: 2041-1723. DOI: 10.1038/s41467-019-10098-z. URL: https://doi.org/10.1038/s41467-019-10098-z.

[74] Yao Li et al. "Simple non-fullerene electron acceptors with unfused core for organic solar cells". In: *Chinese Chemical Letters* 30.1 (2019), pp. 222–224. ISSN: 1001-8417. DOI: 10.1016/j.cclet.2018.09.014. URL: https://dx.doi.org/10.1016/j.cclet.2018.09.014.

[75] J.A. Woollam. *Ellipsometry Measurements*. Web Page. URL: https://www.jawoollam.com/resources/ellipsometry-tutorial/ellipsometry-measurements.

[76] Alexander Hofmann, Markus Schmid, and Wolfgang Brütting. "The Many Facets of Molecular Orientation in Organic Optoelectronics". In: *Advanced Optical Materials* 9.21 (2021), p. 2101004. ISSN: 2195-1071. DOI: 10.1002/adom.202101004.

[77] D. Wynands et al. "Spectroscopic ellipsometry characterization of vacuum-deposited organic films for the application in organic solar cells". In: *Organic Electronics* 13.5 (2012), pp. 885–893. ISSN: 1566-1199. DOI: 10.1016/j.orgel.2012.01.036.

[78] Diamond Light Source. *ES-2: Ambient Pressure NEXAFS*. Web Page. URL: https://www.diamond.ac.uk/Instruments/Structures-and-Surfaces/B07/beamline/B07-B/focal-point-2.html.

[79] Eliot Gann et al. "Quick AS NEXAFS Tool (QANT): a program for NEXAFS loading and analysis developed at the Australian Synchrotron". In: *Journal of Synchrotron Radiation* 23.1 (2016), pp. 374–380. ISSN: 1600-5775. DOI: doi:10.1107/S1600577515018688. URL: https://doi.org/10.1107/S1600577515018688.

[80] Joachim Stöhr. "NEXAFS Spectroscopy". In: *Springer Series in Surface Sciences* (1992). ISSN: 0931-5195. DOI: 10.1007/978-3-662-02853-7.

[81] Thomas J. Ferron et al. "Characterization of the Interfacial Orientation and Molecular Conformation in a Glass-Forming Organic Semiconductor". In: *ACS Applied Materials Interfaces* 14.2 (2022), pp. 3455–3466. ISSN: 1944-8244. DOI: 10.1021/acsami.1c19948.

[82] R. I. Iglamova and S. V. Izmailov. "The external photoelectric effect of semiconductors". In: *Soviet Physics Journal* 19.3 (1976), pp. 373–377. ISSN: 0038-5697. DOI: 10.1007/bf00945696.

[83] Yifan Dong et al. "Orientation dependent molecular electrostatics drives efficient charge generation in homojunction organic solar cells". In: *Nature Communications* 11.1 (2020). ISSN: 2041-1723. DOI: 10.1038/s41467-020-18439-z.

[84] Peter I. Djurovich et al. "Measurement of the lowest unoccupied molecular orbital energies of molecular organic semiconductors". In: 10.3 (2009). 1566-1199, pp. 515–520. URL: https://www.sciencedirect.com/science/article/pii/S1566119908002632.

[85] David Nečas and Petr Klapetek. "Gwyddion: an open-source software for SPM data analysis". In: *Open Physics* 10.1 (2012). ISSN: 2391-5471. DOI: 10.2478/s11534-011-0096-2. URL: http://www.degruyter.com/downloadpdf/j/phys.2012.10.issue-1/s11534-011-0096-2/s11534-011-0096-2.xml.

[86] Uwe Rau et al. "Efficiency Potential of Photovoltaic Materials and Devices Unveiled by Detailed-Balance Analysis". In: *Physical Review Applied* 7.4 (2017). ISSN: 2331-7019. DOI: 10.1103/physrevapplied.7.044016.

[87] Anna Jungbluth, Pascal Kaienburg, and Moritz Riede. "Charge transfer state characterization and voltage losses of organic solar cells". In: *Journal of Physics: Materials* 5.2 (2022), p. 024002. ISSN: 2515-7639. DOI: 10.1088/2515-7639/ac44d9. URL: https://dx.doi.org/10.1088/2515-7639/ac44d9.

[88] Pascal Kaienburg et al. "Assessing the Photovoltaic Quality of Vacuum-Thermal Evaporated Organic Semiconductor Blends". In: *Advanced Materials* (2021), p. 2107584. ISSN: 0935-9648. DOI: 10.1002/adma.202107584. URL: https://dx.doi.org/10.1002/adma.202107584.

[89] William Shockley and Hans J. Queisser. "Detailed Balance Limit of Efficiency of p-n Junction Solar Cells". In: *Journal of Applied Physics* 32.3 (1961), pp. 510–519. ISSN: 0021-8979. DOI: 10.1063/1.1736034.

[90] Mohammed Azzouzi, Thomas Kirchartz, and Jenny Nelson. "Factors Controlling Open-Circuit Voltage Losses in Organic Solar Cells". In: *Trends in Chemistry* 1.1 (2019), pp. 49–62. ISSN: 2589-5974. DOI: 10.1016/j.trechm.2019.01.010.

[91] Johannes Benduhn et al. “Intrinsic non-radiative voltage losses in fullerene-based organic solar cells”. In: *Nature Energy* 2.6 (2017), p. 17053. ISSN: 2058-7546. DOI: 10.1038/nenergy.2017.53.

[92] Xian-Kai Chen et al. “A unified description of non-radiative voltage losses in organic solar cells”. In: *Nature Energy* 6.8 (2021), pp. 799–806. ISSN: 2058-7546. DOI: 10.1038/s41560-021-00843-4.

[93] Jules Bertrandie et al. “The Energy Level Conundrum of Organic Semiconductors in Solar Cells”. In: *Advanced Materials* 34.35 (2022), p. 2202575. ISSN: 0935-9648. DOI: 10.1002/adma.202202575.

[94] J. Lorrmann et al. “Charge carrier extraction by linearly increasing voltage: Analytic framework and ambipolar transients”. In: *Journal of Applied Physics* 108.11 (2010), p. 113705. ISSN: 0021-8979. DOI: 10.1063/1.3516392. URL: http://arxiv.org/pdf/1006.4394.

[95] Antonio Facchetti et al. “Building Blocks for n-Type Molecular and Polymeric Electronics. Perfluoroalkyl- versus Alkyl-Functionalized Oligothiophenes (nT; $n = 26$). Systematics of Thin Film Microstructure, Semiconductor Performance, and Modeling of Majority Charge Injection”. In: *Journal of the American Chemical Society* 126.42 (2004), pp. 13859–13874. ISSN: 0002-7863. DOI: 10.1021/ja0489846.

[96] Cenqi Yan et al. “Non-fullerene acceptors for organic solar cells”. In: *Nature Reviews Materials* 3.3 (2018), p. 18003. ISSN: 2058-8437. DOI: 10.1038/natrevmats.2018.3.

[97] Safa Shoaee et al. “Acceptor Energy Level Control of Charge Photogeneration in Organic Donor/Acceptor Blends”. In: *Journal of the American Chemical Society* 132.37 (2010), pp. 12919–12926. ISSN: 0002-7863. DOI: 10.1021/ja1042726.

[98] Alexander Schubert et al. “Ultrafast Exciton Self-Trapping upon Geometry Deformation in Perylene-Based Molecular Aggregates”. In: *The Journal of Physical Chemistry Letters* 4.5 (2013), pp. 792–796. ISSN: 1948-7185. DOI: 10.1021/jz4000752.

[99] Brooks A. Jones et al. “High-Mobility Air-Stable n-Type Semiconductors with Processing Versatility: Dicyanoperylene-3,4:9,10-bis(dicarboximides)”. In: *Angewandte Chemie International Edition* 43.46 (2004), pp. 6363–6366. ISSN: 1433-7851. DOI: 10.1002/anie.200461324.

[100] Priya J. Jadhav et al. “Triplet Exciton Dissociation in Singlet Exciton Fission Photovoltaics”. In: *Advanced Materials* 24.46 (2012), pp. 6169–6174. ISSN: 0935-9648. DOI: 10.1002/adma.201202397.

[101] Valentina Belova et al. “Real-Time Structural and Optical Study of Growth and Packing Behavior of Perylene Diimide Derivative Thin Films: Influence of Side-Chain Modification”. In: *The Journal of Physical Chemistry C* 122.15 (2018), pp. 8589–8601. ISSN: 1932-7447. DOI: 10.1021/acs.jpcc.8b00787.

[102] Christopher Lorch et al. “Growth and annealing kinetics of α-sexithiophene and fullerene C60 mixed films”. In: *Journal of Applied Crystallography* 49.4 (2016), pp. 1266–1275. ISSN: 1600-5767. DOI: 10.1107/s1600576716009936.

[103] Hannah BürckstÃ¼mmer et al. “Tailored merocyaninedyes for solution-processed BHJ solar cells”. In: *J. Mater. Chem.* 20.2 (2010), pp. 240–243. ISSN: 0959-9428. DOI: 10.1039/b916181c.

[104] Jianwei Shen et al. “Ultrafast photoinduced dynamics of a donor-π bridge-acceptor based merocyanine dye”. In: *Scientific Reports* 12.1 (2022). ISSN: 2045-2322. DOI: 10.1038/s41598-022-23080-5.

[105] Jun Matsui et al. “Photoconductivity of Micrometer Long Organic Single Crystal Fiber Array Prepared by EvaporationâInduced Self-Assembled

Method". In: *Israel Journal of Chemistry* 62.5-6 (2022). ISSN: 0021-2148. DOI: 10.1002/ijch.202100083.

[106] Vera Steinmann et al. "Simple, Highly Efficient Vacuum-Processed Bulk Heterojunction Solar Cells Based on Merocyanine Dyes". In: *Advanced Energy Materials* 1.5 (2011), pp. 888–893. ISSN: 1614-6832. DOI: 10.1002/aenm.201100283.

[107] Yi-Hong Chen et al. "Vacuum-Deposited Small-Molecule Organic Solar Cells with High Power Conversion Efficiencies by Judicious Molecular Design and Device Optimization". In: *Journal of the American Chemical Society* 134.33 (2012), pp. 13616–13623. ISSN: 0002-7863. DOI: 10.1021/ja301872s.

[108] Bregt Verreet et al. "The characterization of chloroboron (iii) subnaphthalocyanine thin films and their application as a donor material for organic solar cells". In: *Journal of Materials Chemistry* 19.30 (2009), p. 5295. ISSN: 0959-9428. DOI: 10.1039/b902342a.

[109] Tao Zhang et al. "Intrinsic measurements of exciton transport in photovoltaic cells". In: *Nature Communications* 10.1 (2019). ISSN: 2041-1723. DOI: 10.1038/s41467-019-09062-8. URL: https://www.nature.com/articles/s41467-019-09062-8.pdf.

[110] Roland Fitzner et al. "Correlation of π-Conjugated Oligomer Structure with Film Morphology and Organic Solar Cell Performance". In: *Journal of the American Chemical Society* 134.27 (2012), pp. 11064–11067. ISSN: 0002-7863. DOI: 10.1021/ja302320c.

[111] Rico Meerheim, Christian Körner, and Karl Leo. "Highly efficient organic multi-junction solar cells with a thiophene based donor material". In: *Applied Physics Letters* 105.6 (2014), p. 063306. ISSN: 0003-6951. DOI: 10.1063/1.4893012.

[112] Donghui Li et al. "Aggregation of non-fullerene acceptors in organic solar cells". In: *Journal of Materials Chemistry A* 8.31 (2020), pp. 15607–15619. ISSN: 2050-7488. DOI: 10.1039/d0ta03703f.

[113] Brooks A. Jones et al. "Tuning Orbital Energetics in Arylene Diimide Semiconductors. Materials Design for Ambient Stability of n-Type Charge Transport". In: *Journal of the American Chemical Society* 129.49 (2007), pp. 15259–15278. ISSN: 0002-7863. DOI: 10.1021/ja075242e.

[114] Artur Glavic and Matts Björck. "GenX 3: the latest generation of an established tool". In: *Journal of Applied Crystallography* 55.4 (2022), pp. 1063–1071. ISSN: 1600-5767. DOI: 10.1107/s1600576722006653.

[115] Wolfgang Tress, Karl Leo, and Moritz Riede. "Influence of Hole-Transport Layers and Donor Materials on Open-Circuit Voltage and Shape of I-V Curves of Organic Solar Cells". In: *Advanced Functional Materials* 21.11 (2011), pp. 2140–2149. ISSN: 1616-301X. DOI: https://doi.org/10.1002/adfm.201002669. URL: https://onlinelibrary.wiley.com/doi/abs/10.1002/adfm.201002669.

[116] Oskar J. Sandberg, Mathias Nyman, and Ronald Österbacka. "Effect of Contacts in Organic Bulk Heterojunction Solar Cells". In: *Physical Review Applied* 1.2 (2014). ISSN: 2331-7019. DOI: 10.1103/physrevapplied.1.024003.

[117] Jens Wehner and Björn Baumeier. "Multiscale simulations of singlet and triplet exciton dynamics in energetically disordered molecular systems based on many-body Green's functions theory". In: *New Journal of Physics* 22.3 (2020), p. 033033. ISSN: 1367-2630. DOI: 10.1088/1367-2630/ab7a04.

[118] Vasileios C. Nikolis et al. "Field Effect versus Driving Force: Charge Generation in Small-Molecule Organic Solar Cells". In: *Advanced Energy*

Materials 10.47 (2020), p. 2002124. ISSN: 1614-6832. DOI: 10.1002/aenm.202002124.

[119] M.C. Scharber et al. "Design Rules for Donors in Bulk-Heterojunction Solar Cells - Towards 10% Energy-Conversion Efficiency". In: *Advanced Materials* 18.6 (2006), pp. 789–794. ISSN: 0935-9648. DOI: https://doi.org/10.1002/adma.200501717. URL: https://onlinelibrary.wiley.com/doi/abs/10.1002/adma.200501717.

[120] David C. Coffey et al. "An Optimal Driving Force for Converting Excitons into Free Carriers in Excitonic Solar Cells". In: *The Journal of Physical Chemistry C* 116.16 (2012), pp. 8916–8923. ISSN: 1932-7447. DOI: 10.1021/jp302275z.

[121] George F. Burkhard, Eric T. Hoke, and Michael D. Mcgehee. "Accounting for Interference, Scattering, and Electrode Absorption to Make Accurate Internal Quantum Efficiency Measurements in Organic and Other Thin Solar Cells". In: *Advanced Materials* 22.30 (2010), pp. 3293–3297. ISSN: 0935-9648. DOI: 10.1002/adma.201000883.

[122] Katrin Ortstein et al. "Band gap engineering in blended organic semiconductor films based on dielectric interactions". In: *Nature Materials* 20.10 (2021), pp. 1407–1413. ISSN: 1476-1122. DOI: 10.1038/s41563-021-01025-z.

[123] A. Baumann et al. "A New Approach for Probing the Mobility and Lifetime of Photogenerated Charge Carriers in Organic Solar Cells Under Real Operating Conditions". In: *Advanced Materials* 24.32 (2012), pp. 4381–4386. ISSN: 0935-9648. DOI: https://doi.org/10.1002/adma.201200874. URL: https://onlinelibrary.wiley.com/doi/abs/10.1002/adma.201200874.

[124] Christian Koerner et al. “Probing the effect of substrate heating during deposition of DCV4T:C60 blend layers for organic solar cells”. In: 13.4 (2012). 1566-1199, pp. 623–631. URL: https://www.sciencedirect.com/science/article/pii/S1566119912000122.

[125] Gregory M. Su et al. “First-Principles Predictions of Near-Edge X-ray Absorption Fine Structure Spectra of Semiconducting Polymers”. In: *The Journal of Physical Chemistry C* 121.17 (2017), pp. 9142–9152. ISSN: 1932-7447. DOI: 10.1021/acs.jpcc.7b01353. URL: https://doi.org/10.1021/acs.jpcc.7b01353.

[126] M. Oehzelt et al. “α-Sexithiophene on Cu(110) and Cu(110)-(2x1)O: An STM and NEXAFS study”. In: 603.2 (2009). 0039-6028, pp. 412–418. URL: https://www.sciencedirect.com/science/article/pii/S0039602808008509.

[127] Shrayesh N. Patel et al. “NEXAFS Spectroscopy Reveals the Molecular Orientation in Blade-Coated Pyridal[2,1,3]thiadiazole-Containing Conjugated Polymer Thin Films”. In: *Macromolecules* 48.18 (2015), pp. 6606–6616. ISSN: 0024-9297. DOI: 10.1021/acs.macromol.5b01647.

[128] A. Y. Matsuura et al. “Adsorption of merocyanine dye on rutile TiO2(110)”. In: 360.1 (2002). 0009-2614, pp. 133–138. URL: https://www.sciencedirect.com/science/article/pii/S0009261402008254.

[129] Akihito Imanishi et al. “Pretreatment Dependence of Adsorption Properties of Merocyanine Dye at Rutile (110) and (100) TiO2 Surfaces Studied by C K-Edge NEXAFS”. In: *The Journal of Physical Chemistry C* 113.39 (2009), pp. 17254–17261. ISSN: 1932-7447. DOI: 10.1021/jp904993u.

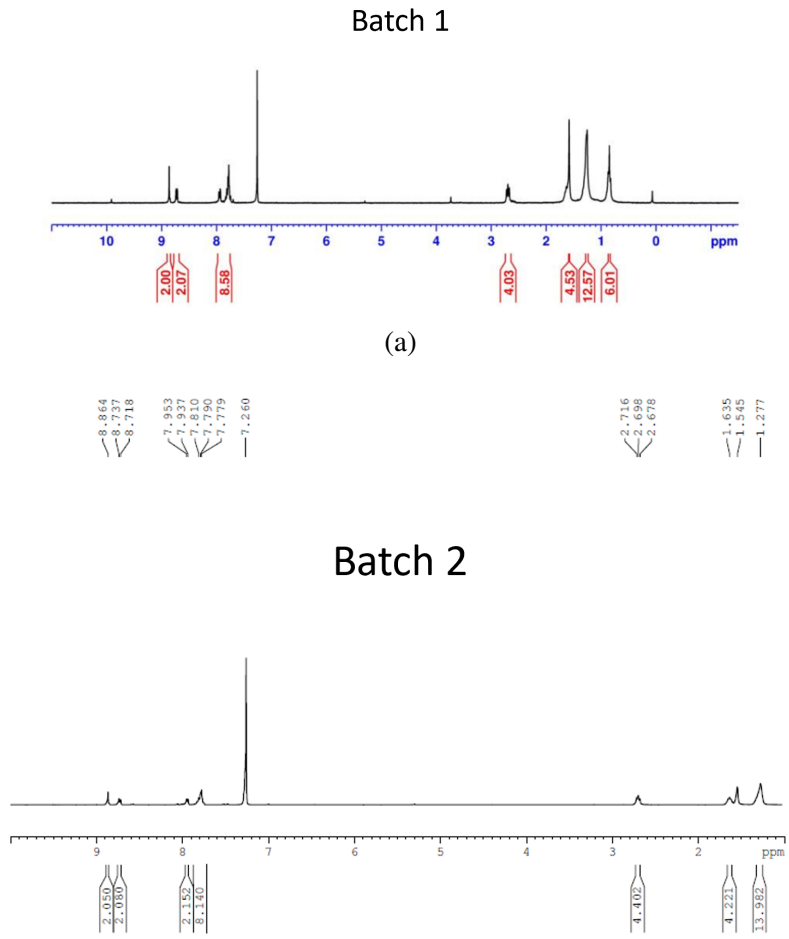
[130] U. Heinemeyer et al. "Uniaxial anisotropy of organic thin films determined by ellipsometry". In: *physica status solidi (a)* 205.4 (2008), pp. 927–930. ISSN: 1862-6300. DOI: 10.1002/pssa.200777765.

[131] James N Hilfiker, RA Synowicki, and HG Tompkins. "Spectroscopic ellipsometry methods for thin absorbing coatings". In: *51st Annual Technical Conference Proceedings of the Society of Vacuum Coaters*, pp. 511–516.

[132] Irfan Habib. *NEXAFS and SE data for PhD Thesis*. http://dx.doi.org/10.5287/ora-y5m80zvzr. DOI: 10.5287/ora-y5m80zvzr.

A | Appendix

A.1 BTIC-H NMR



(a)

(b)

Figure A.1: H-NMR data of a) the first batch and b) second batch of BTIC-H received. The NMR was recorded in $CDCl_3$. Data was provided by Dondong Xia from the Beijing University of Chemical Technology.

A.2 Spectroscopic ellipsometry fitting

A.2.1 BTIC-H

Fitting details and raw data can be found on GitHub via https://github.com/ifoo07/PhD-Thesis-Data/tree/main/SE_data/BTIC-H_SE_Fitting or the Oxford University Research Archive [132].

A.2.2 PDIFCN2

Fitting details and raw data can be found on GitHub viahttps://github.com/ifoo07/PhD-Thesis-Data/tree/main/SE_data/PDIFCN2_SE_Fitting or the Oxford University Research Archive [132].

A.2.3 TTR

Fitting details and raw data can be found on GitHub via https://github.com/ifoo07/PhD-Thesis-Data/tree/main/SE_data/TTR_SE_Fitting or the Oxford University Research Archive [132].

A.2.4 a6T

Fitting details and raw data can be found on GitHub via https://github.com/ifoo07/PhD-Thesis-Data/tree/main/SE_data/a6T_SE_fitting or the Oxford University Research Archive [132].

A.2.5 DTDCPB

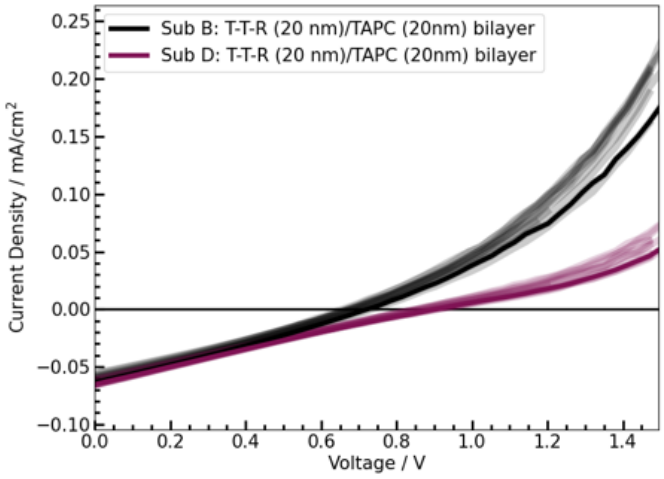
Fitting details and raw data can be found on GitHub via https://github.com/ifoo07/PhD-Thesis-Data/tree/main/SE_data/DTDCPB_SE_

Fitting or the Oxford University Research Archive [132].

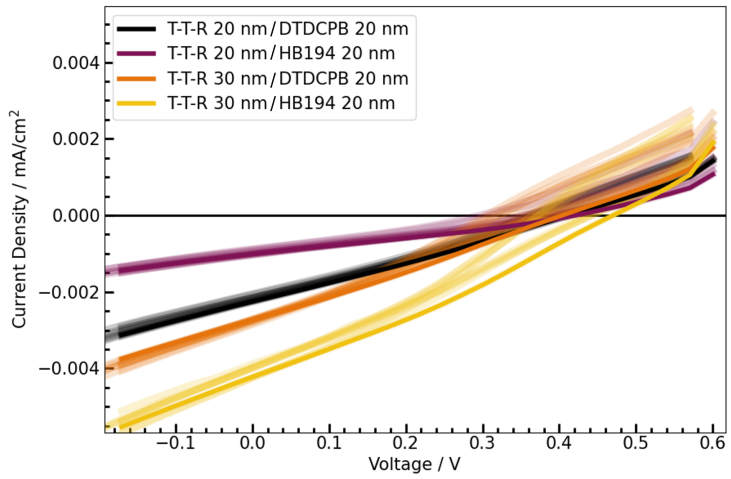
A.2.6 HB194

Fitting details and raw data can be found on GitHub via https://github.com/ifoo07/PhD-Thesis-Data/tree/main/SE_data/HB194_SE_Fitting or the Oxford University Research Archive [132].

A.3 TTR preliminary devices



(a)



(b)

Figure A.2: JV scans of TTR used as an acceptor in a) TAPC (20 nm)/TTR (20 nm), b) donor (20 nm)/TTR (20 or 30 nm), as indicated in the plot.

A.4 PDIFCN2 preliminary devices

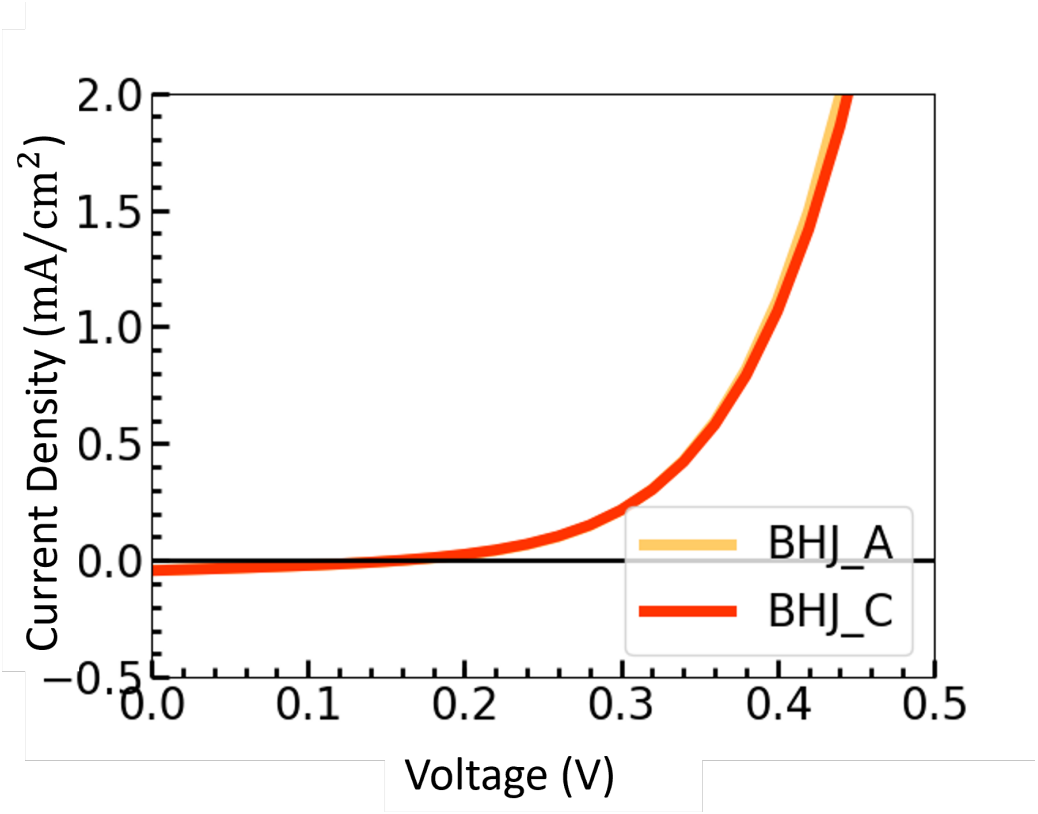


Figure A.3: JV scans of PDIFCN2 in BHJ devices on two different substrates (denoted by A and C) with ZnPc as donor: ZnPc:PDIFCN2 (20 nm 1:1 vol ratio). PHJ devices were also made according to ZnPc (25 nm)/PDIFCN2 (25 nm) but all devices were severely shunted (not shown above).

A.5 APS of PHJ donors

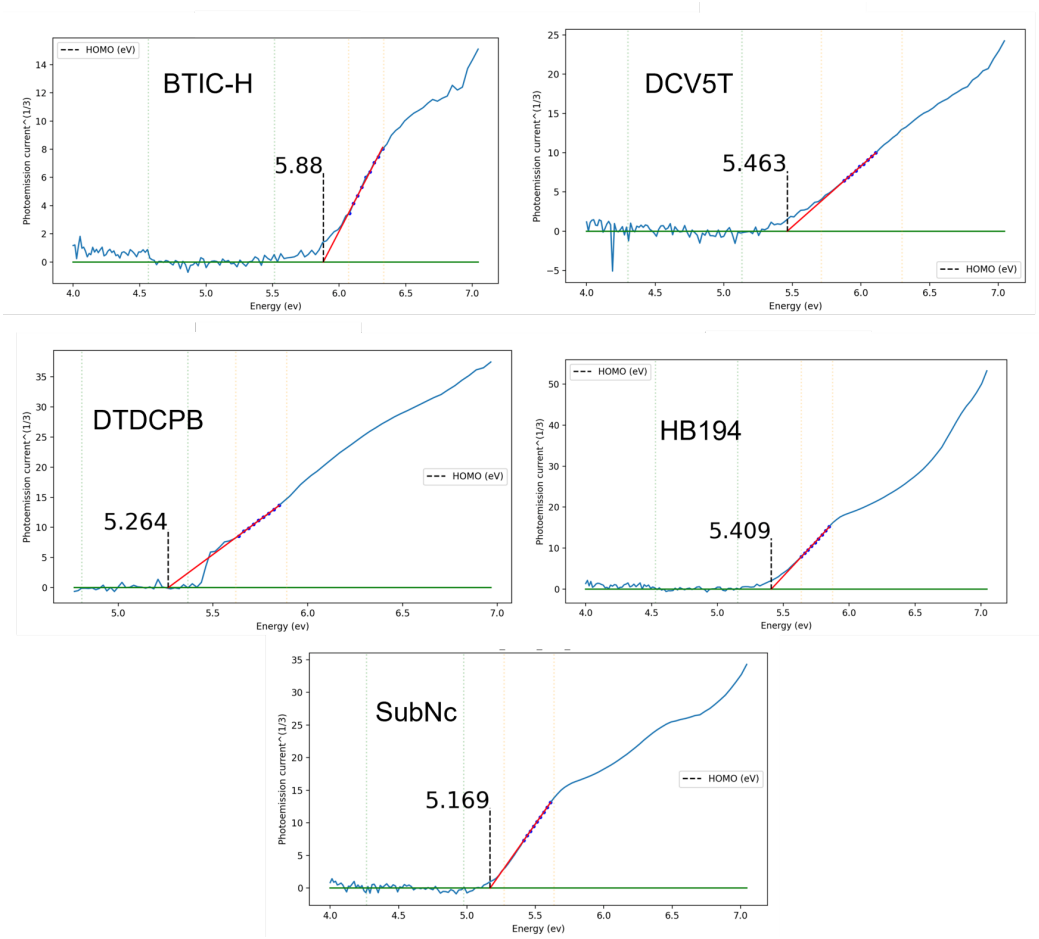


Figure A.4: APS data and fitting of donor materials used in PHJ devices used in Chapter 5.

A.6 EA estimation values

Material	Optical Gap (eV)	HOMO (eV)	HOMO + Optical Gap (eV)	LUMO (eV)
BTIC-H	1.6	-5.9	-4.3	-3.7
DTDCPB	1.7	-5.3	-3.6	-2.9
HB194	1.9	-5.4	-3.5	-2.8
SubNc	1.7	-5.2	-3.5	-2.8
DCV5T	1.7	-5.5	-3.8	-3.1

Table A.1: Table of values used to estimate the LUMO values of materials used in PHJ devices in Chapter 5. LUMO values are calculated using Equation 3.6.

A.7 Voltage Loss Fits for BTIC-H PHJ Devices

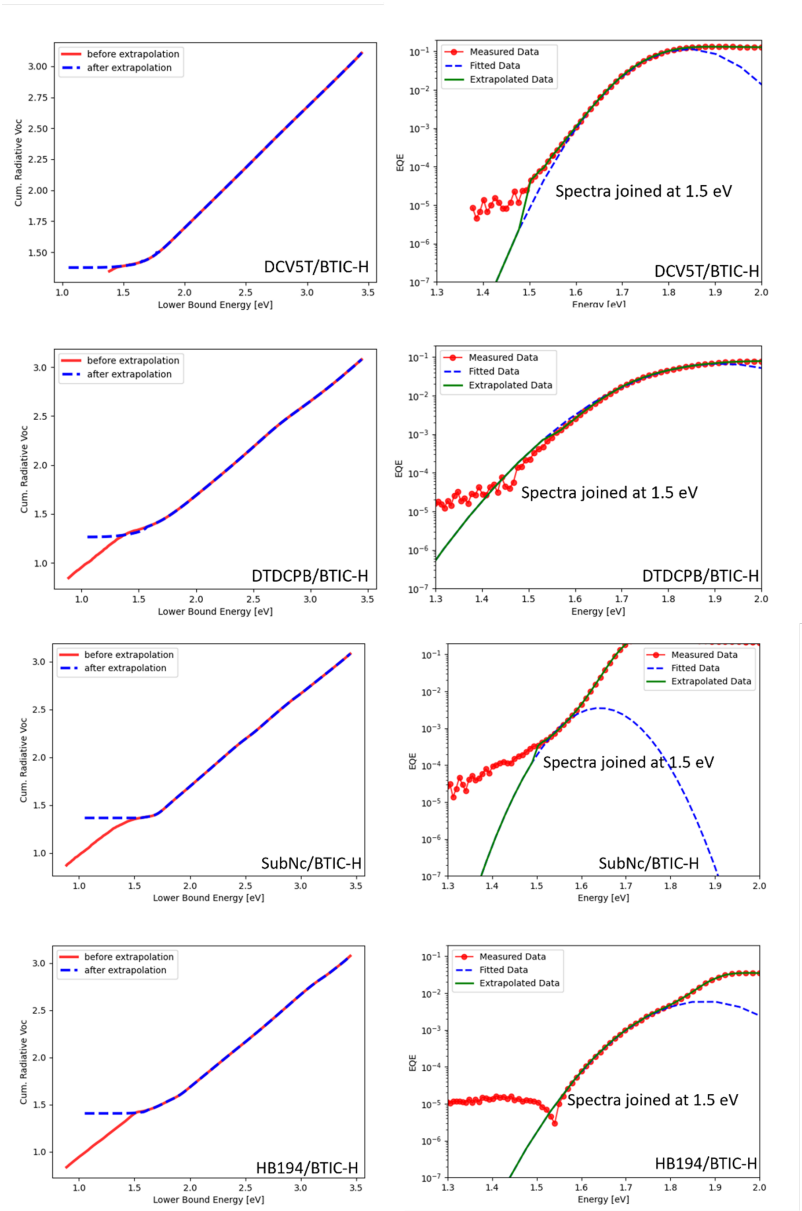


Figure A.5: : Images of the fitting process for the Voltage Loss Analysis as per the detailed balance principle and the guidelines proposed in [86, 87, 88]. For each PHJ the EQE are fitted to extend the data past the noise floor (plots on the right) so as to make sure the cumulative radiative V_{OC} saturates (plots on the left).

A.8 NEXAFS Data

Fitting of NEXAFS data in this thesis was carried out using QANT [79], an Igor package written by Elliot Gann to perform a comprehensive analysis of NEXAFS data. Data processing, plotting, and fitting was all carried out using QANT. Igor files containing the data relevant to each fit can be found on GitHub via https://github.com/ifoo07/PhD-Thesis-Data/tree/main/NEXAFS_data or the Oxford University Research Archive [132].